DETERMINATION OF NEUTRON ENERGY SPECTRA INSIDE A WATER PHANTOM IRRADIATED BY NEUTRONS OF ENERGY UP TO ~ 64 MeV

by

MARK HERBERT

Thesis presented for the degree of

DOCTOR OF PHILOSOPHY

In the Department of Physics

University of Cape Town

October 2009

Abstract

A neutron spectrometer based on an NE230 deuterated organic liquid scintillator (25 mm diameter x 25 mm) has been developed for measuring neutron spectra in water. The spectrometer is capable of measuring neutron energies above 5 MeV, set by the electronic threshold. An important feature of the spectrometer is that it is able to discriminate between recoiling protons that are associated with neutron interactions that take place in the detector from recoiling protons that arise from n-p scattering in the water. The spectrometer was tested by recording pulse height spectra in a water phantom irradiated by neutrons of energy up to ~ 64 MeV. Neutron energy spectra were obtained from the pulse height spectra by Bayesian unfolding with the code MAXED using a response matrix that was determined experimentally. The efficiency of the NE230 detector was determined experimentally relative to an NE213 detector of known efficiency. A series of detailed measurements was taken at positions in the phantom along the axis of the neutron beam while exploratory runs were made off the beam axis. Results from measurements made along the axis of the neutron beam compare well with Monte Carlo calculations using MCNPX.

DEDICATION

I dedicate this work to
my grandparents, David and Amina Herbert,
my parents, Sitaar and Barbie Herbert,
my sister, Amanda Herbert and
my friends Nadia Matthews and Gadija Adams.

ACKNOWLEDGEMENTS

I wish to express my sincere appreciation and gratitude to:

Professor Saalih Allie, my supervisor, for his help, guidance, support and editing of the thesis.

Emeritus Professor Frank Brooks, for conceptualizing the work and for his help and guidance with the experiments and analysis of the data.

Dr. Rudolf Nchodu, for his advice, help and support, especially with the MCNPX simulations.

Professor Andy Buffler, Dr. Dan Jones, Dr. Mark Swanepoel and Julian Symons for their help and support.

Marilyn Lawrence, Gadija Adams, Peter Booysen and Ricardo Collins for proof reading the thesis.

Jerome Pekeur for the drawings.

George Swartz and Lindsay Davids for the many versions of the thesis they printed.

My mother, Barbie, and father, Sitaar, for their encouragement and support.

My sisters, Mandy and Norma, brothers, Tony and David and the rest of my family Amy, Callan, Amber, Tony junior, my grandmother Amina, uncles and aunts for their encouragement.

My friends for their support and with whom I shared many joyful and happy moments during the completion of this work, in particular, Nadia, Enrico, Anzil, Melanie, Marlan, Michael, Ricardo, Liezel, Michelle, Pedro, Colan Gavin, Ricardo, Vincent, Gadija, Sue-Ann, Lieschen, Portia, Samantha, Vinoliah, Sybil, Sus Vicky, Peter, Freda, Bambi, Angelique, Broadwin, Kim Le Roux, Jacqueline Vermaak, Virginia Thompson, Candice Hendricks, Rashida Adams, Patricia Conradie and Charlie (The Barber).

Staff of iThemba LABS as well the staff of the Physics department.

The Claude Leon Harris Foundation, Joseph Stone Bursary, the National Research Foundation and the University of Cape Town for financial assistance.

CONTENTS

LIST OF FIGURES

LIST OF TABLES

CHAPTER 1

INTRODUCTION

The underlying principle of radiation therapy is that energy is deposited in body tissue by ionising radiation and that by delivering a suitably tailored beam of particles to an affected region a cancerous tumour can be destroyed. Radiation therapy includes both conventional radiation therapy using electrons and photons and hadron radiation therapy using neutrons, protons and heavy ions such as carbon and neon. The deposition of energy within tissue depends on both the type of radiation used and the energy of the radiation. Charged particles, like electrons, protons and heavy ions cause direct ionization by interacting with the electrons in the tissue via Coulomb interactions. On the other hand, uncharged particles such as photons and neutrons cause ionization indirectly. Photons interact with the atomic electrons via the photoelectric effect, Compton scattering and pair production while neutrons interact by scattering and nuclear reactions with atomic nuclei.

Data accumulated over the past 50 years have shown that while several types of cancerous lesions are resistant to conventional radiation radiotherapy, they respond to fast neutron and heavy ion radiation therapy [Da00, Hu01, Le01, Wa04, Jo07]. For example, clinical trials have indicated that fast neutron therapy has proven to be more effective than conventional radiation therapy for the treatment of certain types of inoperable cancerous tumours [Le01] of the salivary gland [La93, Do03] and the prostate [Ru93]. As of 2007, it is estimated that about 27 000 patients have been treated using neutron radiation therapy [Jo07].

Fast neutrons that are used in therapy typically have energies up to 70 MeV [Jo01b]. Beams of fast neutrons that are used in therapy can be generated by fusion reactions such as $d + T$ and $d + D$ or by stripping and inelastic reactions of deuterons or protons on thick beryllium targets such as $(d + Be)$ and $(p + Be)$ [Ro97, Jo01b, Jo07]. However, the $(p + Be)$ reaction is preferred to the $(d + Be)$ reaction because protons can be accelerated to twice the energy of deuterons with particle accelerators producing more penetrating beams with higher dose rates [Aw80, Te82, Jo01b].

Neutron beams produced by thick Be-targets are broadly distributed in energy [Wh92]. A treatment facility for carrying out neutron radiation therapy using the $(p + Be)$ reaction was developed at iThemba LABS (South Africa) during the late 1980's and between 1988 and 2007, 1396 patients were treated there [Jo07].

1.1 Interaction of neutrons with body tissue

Neutrons interact with the nuclei of the atoms through scattering (elastic or inelastic) and neutron induced nuclear reactions as shown in fig. 1.1. The particles that are produced in these interactions then cause ionization of the surrounding atoms. During elastic scattering, a neutron collides elastically with a nucleus, and transfers some of its energy to this nucleus, which then recoils leading to ionisation of the surrounding atoms. During inelastic scattering an excited nucleus is formed which emits gamma rays that cause ionisation of the surrounding atoms. Nuclear reactions take place when the neutron is absorbed by a nucleus, which then decays by the emission of particles (gammas, protons, alphas and fission fragments) [Dö95, Sh90, Tu95].

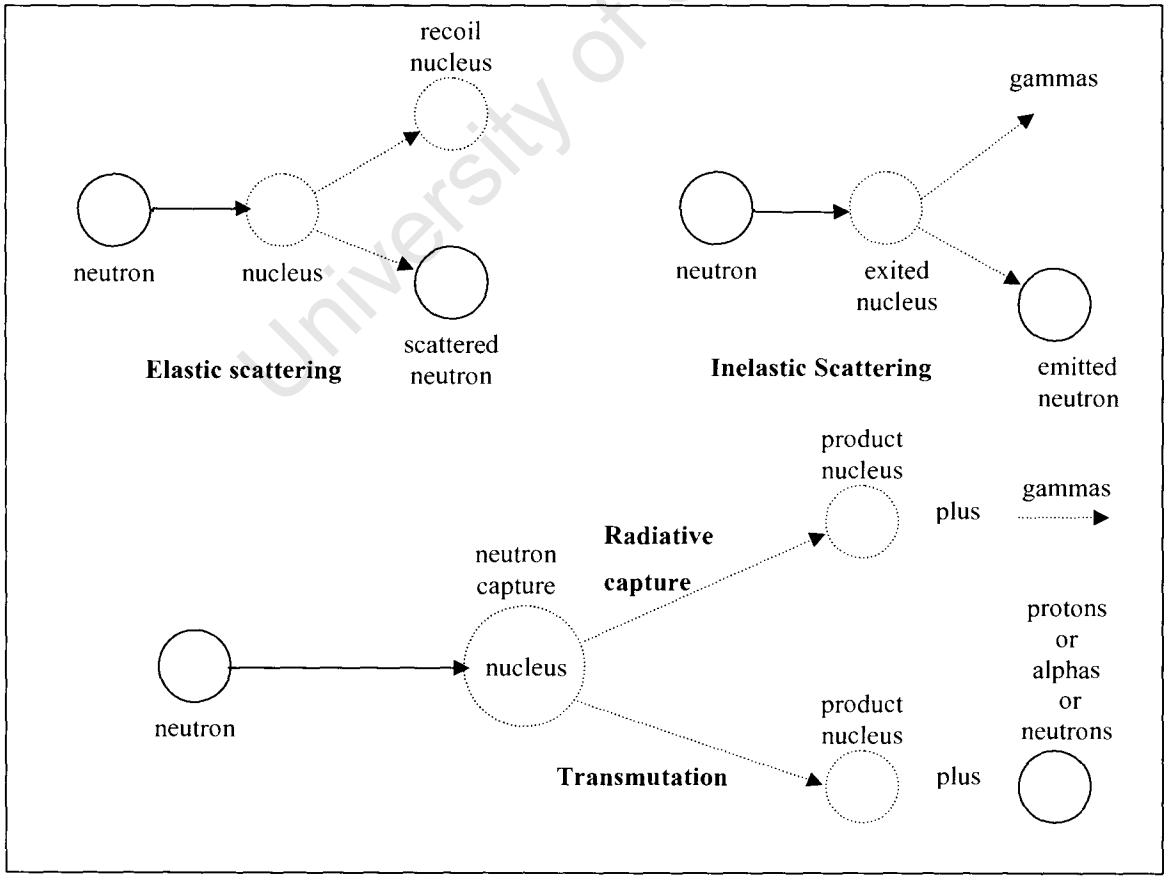

Fig. 1.1 *Schematic diagram showing various interactions of neutrons with atomic nuclei in matter.*

Human body tissue consists of about 10% hydrogen, 18% carbon, 3% nitrogen, 65% oxygen and 4% various trace elements [Wh92]. Fig. 1.2(a)-(d) shows the various reaction cross-sections (elastic, non-elastic and total) for neutrons on these elements as a function of neutron energy between 1 and 70 MeV. In the case of hydrogen (fig.1.2 (a)) the reactions proceed almost exclusively via elastic scattering while in the case of the other elements (fig.1.2(b)-(d)) the non-elastic reactions contribute significantly to the total reaction cross-section. Fig. 1.2(e) shows a comparison of the total reaction cross-sections for the elements in question as a function of neutron energy. Above 10 MeV both the elastic and the total reaction cross-sections for carbon, oxygen and nitrogen, respectively exceed the total reaction cross-section for hydrogen. At these energies, transmutation reactions with the carbon, oxygen and nitrogen nuclei can occur, leading to the emission of either protons or alpha particles or neutrons. Below 10 MeV the total reaction cross-section for hydrogen increases both smoothly and sharply while for the other elements various resonance structures can be seen. At much lower energies of the order of 0.1 MeV or less (not shown) the total cross-section for hydrogen exceeds the total reaction cross-sections for the other elements. The neutrons energy distribution inside a human will therefore depend to a large extent on the differential elastic and inelastic scattering cross-sections. In the present work human tissue was simulated by water which has scattering properties close to those of tissue.

The energy that is deposited in tissue depends not only on the cross-sections but also on the type of ionising particle that is released after the neutron has undergone scattering or a nuclear reaction. A measure of the energy deposited is the "kinetic energy released in matter" (kerma). At energies above 1 MeV energy is deposited in tissue mainly by neutron interactions with hydrogen and oxygen. This can be seen from fig. 1.3 taken from Chadwick et al. [Ch99] which shows the relative percentage kerma for various elements as a function of neutron energy in muscle tissue. Thus, at 60 MeV, for example, neutron interactions with hydrogen and oxygen account for about 90% of the kerma while neutron interactions with carbon and nitrogen account for only a few percent each. This is one of the reasons why it is possible to simulate human tissue by water as is done in the present work (see 1.2.2).

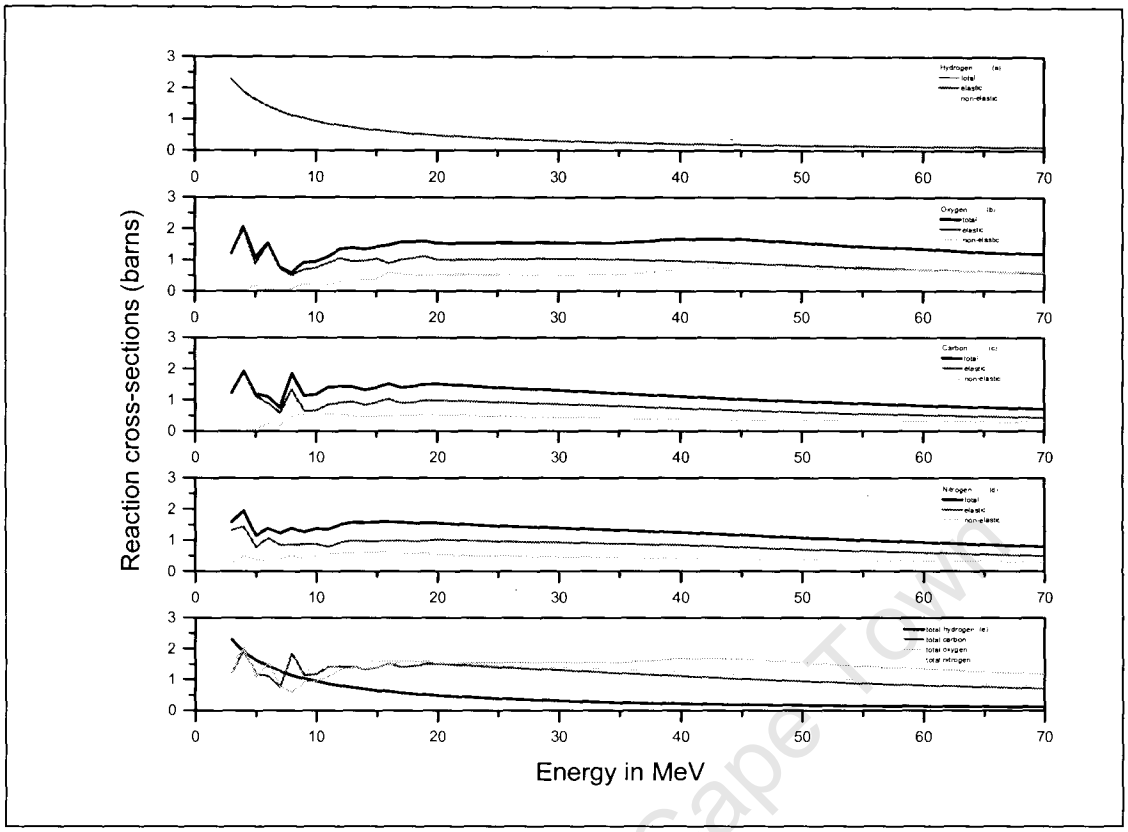

Fig. 1.2 *Reaction cross-sections (elastic, non-elastic and total) for neutrons on the tissue elements hydrogen, carbon, oxygen and nitrogen as a function of neutron energy between 1 and 70 MeV [Ro91].*

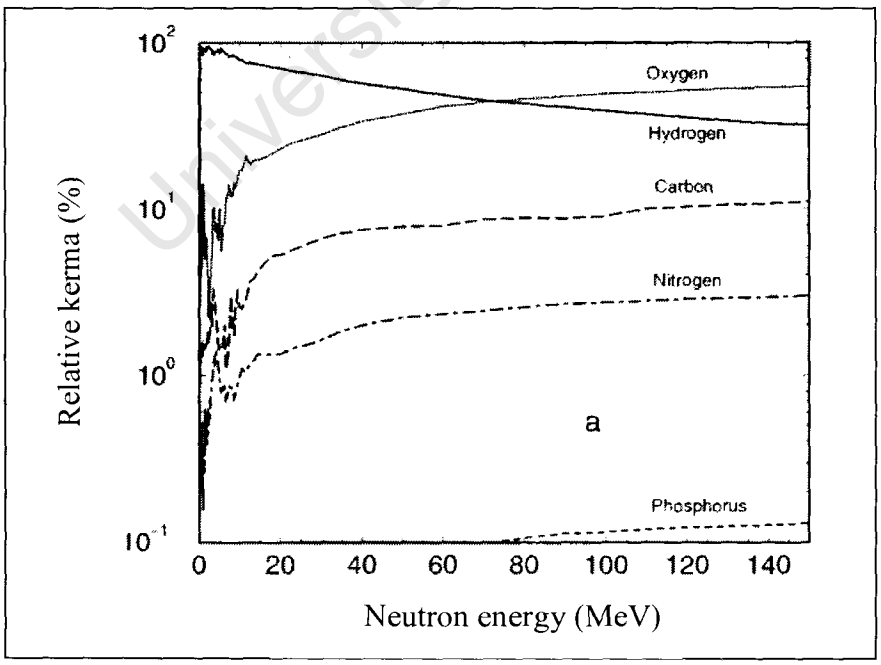

Fig. 1.3 *Relative percentage "kinetic energy released in matter" (kerma) due to neutron interactions with hydrogen, carbon, nitrogen, oxygen and phosphorus in muscle tissue as a function of neutron energy [Ch99].*

1.2 Determination of neutron energy spectra

Calculating the energy deposited in tumour site under treatment involves both detailed knowledge of the neutron beam delivery system as well as of the energy spectrum of the source [Wh92, Ro97, Jo92, Bo99, Jo01a]. In addition, an understanding of the evolution of the neutron energy spectrum as it passes through the body is required because neutron interactions with nuclei of body tissue are energy dependent. In principle, these energy spectra can either be calculated by Monte Carlo Methods or measured experimentally [Dö83, Cr91, Jo92, Ro97, Bi98, Bo99, Jo01b, Be02]. However, there are a number of difficulties that are involved in carrying out either the calculations or experiments as discussed below.

1.2.1 Monte Carlo Calculations

A number of Monte Carlo codes have been developed for use in nuclear physics [Ro97, Bo99, Ro06]. For example, GEANT4 [Ag03], which was designed to simulate the transport of elementary particles through matter, has been used in various applications including for radiation therapy with neutrons [Ca04]. Of particular interest to the present work are MCNP and MCNPX. MCNP was developed at Los Alamos Laboratory for simulating nuclear interactions involving neutron, photon and electron in three-dimensional geometries [Br97]. MCNPX [Hu97, Wa99] combines the general features of MCNP for modeling geometries and sources [Br97] with various theoretical models used in the Monte Carlo code LAHET [Pr89]. MCNPX has been used to characterize the source spectrum of radiotherapy facilities [Ro97, Bo99] as well as to determine dose distributions from these sources [De98, Bo99].

Despite the usefulness of the Monte Carlo calculations one of the main limitations that limits the accuracy of the predictions is the degree to which the necessary reaction cross-sections are known. In particular, this applies to the energy regions above 20 MeV where the non-elastic contribution to the reaction cross-section is significant and have either not been measured or are difficult to calculate using present nuclear models [Br02b].

1.2.2 Measurements

There are a variety of methods that can be used to measure neutron energy spectra. At the energies of interest, the techniques include time-of-flight, recoil spectrometry, threshold (activation or fission) spectrometry and methods based on neutron moderation [Jo92, Br02b]. The time-of-flight technique involves measuring the flight times of neutrons over well defined distances [Kn89, Br02b] and then converting the flight times to energies. Recoil spectrometry is based on measuring the energy of recoil nuclei such as ^{1}H and ^{2}H [Kn89, Br02b] that result from neutron elastic scattering. Threshold spectrometry involves using activation or fission foils to indicate neutron energy by observing the appearance of one of more products from endothermic neutron-induced reactions within the foil [Kn89, Br02b]. The observation of these products indicates that the neutron energy has exceeded the threshold for the reaction. Bonner spheres are an example of a method that is based on moderating neutrons. In this case, neutrons are typically moderated using polyethylene spheres before being detected at the centre. The information that is obtained from a number of spheres of different dimensions can be combined and unfolded to obtain an energy spectrum [Kn89, Br02b].

In order to study the way in which the spectrum changes as it passes though the body it is necessary to perform measurements as a function of depth within the tissue. Since it is not practical to use real body tissue for this purpose, experiments are carried out in tissue-equivalent phantoms. Although various tissue equivalent materials have been suggested [AA80], it has been recommended that water be used as the reference phantom material [Br81, IC45, Mi87] in clinical neutron dosimetry. This is largely due to its similarity to muscle tissue with regard to energy absorption (see 1.1) and it is much easier to carry out measurements with water than with other suggested tissue equivalent materials. Monte Carlo calculations have confirmed that water is a good substitute for soft body tissue for neutron energies up to 80 MeV [So00].

The properties of the neutron detector which is placed inside a water phantom also have to be taken into account, i.e. the detector should be similar in composition to water in order to reduce distortions in the measured energy spectrum. Also the energies of the secondary neutrons must be significantly below those of the primary neutrons but the total flight time from the target to the interaction site in the detector

must still be close to that of the primary neutron. Time of flight, which is the most accurate of the methods described above for measuring neutron energy spectra, cannot be used to measure neutron energies inside a water phantom [Cr91, Jo92]. This is due to the fact that the neutrons may be scattered in the water before entering the detector, resulting in an ill-defined flight path (see fig.1.4).

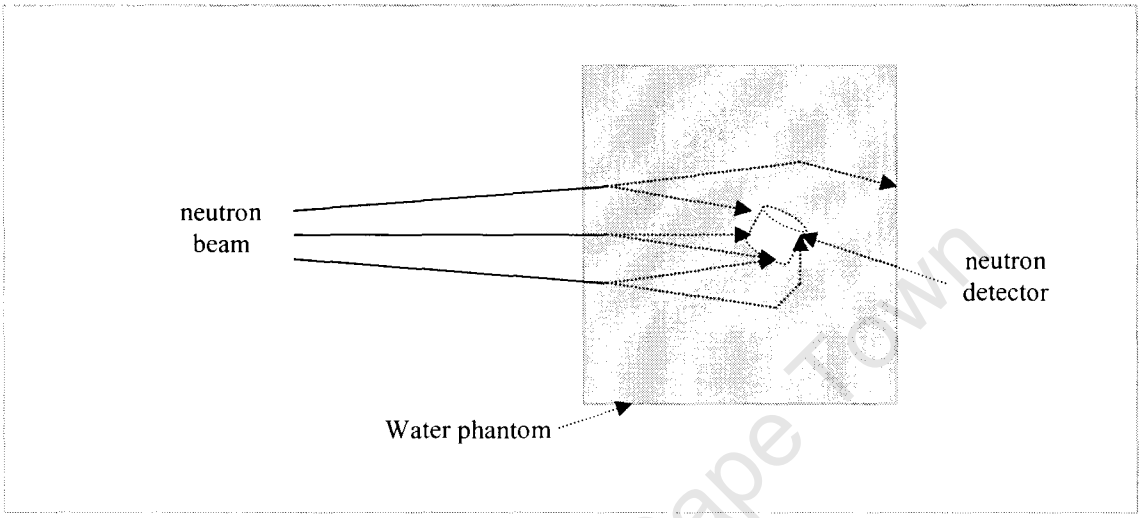

Fig.1.4 *Due to scattering, the neutrons do not have a well-defined flight path before entering the detector.*

Both recoil spectrometry and threshold spectrometry has been used to measure energy spectra in a water phantom. At energies above 20 MeV, threshold spectrometry has been less favoured than recoil spectrometry because of the large uncertainties in the activation cross-sections at the higher energies [Mo82, Cr91]. A number of studies using recoil spectrometers, with NE213 liquid scintillator as the neutron detector, have been reported [Ul81, Cr91, Jo92]. NE213 is well suited for such in-phantom measurements because the scintillator has similar scattering properties to water. The scintillator also has good pulse shape properties to discriminate against gamma rays [Cr91, Br02b]. In addition NE213 also has an isotropic response and is capable of covering the whole energy range of interest. However, the detector is not able to discriminate between recoil protons that arise from interactions in the water from those produced within the detector itself [Cr91].

1.3 Previous work

Below 20 MeV a number of measurements of neutron energy spectra have been carried out [Pa72, Pe79, Sc81, Bo82, Mo82, Be87]. These include in-air measurements i.e. source spectra, as well as in-phantom measurements using water. A comparison with a Monte Carlo calculation has indicated reasonably good agreement over this energy range [Dö83] for both types of measurements. However, at energies above 20 MeV, relatively few experiments have been carried out. In addition the majority of studies have involved measurements in air [Aw80, Bi87, Cr91, Jo92, Jo01b, Ro97, Bo99] while only 2 in-phantom experiments using water as the tissue equivalent material have been reported [Cr89, Cr91]. Monte Carlo calculations have been carried out by Ross et al. [Ro97] and Bohm et al. [Bo99] in which the source has been modelled (in air) using MCNP+LAHET and MCNP, respectively.

Fig. 1.5 shows measurements (in air) of the energy spectrum for the neutron radiation therapy source at iThemba LABS based on the time of flight method [Jo01b]. The figure also shows Monte Carlo simulations for this source using MCNP+LAHET [Ro97]. The results are presented in the figure in the form of relative fluences. The measured spectrum agrees well with the Monte Carlo calculations over the whole energy range. However, there are systematic differences at the higher energies. These have been attributed to the finite energy resolution of the measurements that were not properly taken into account [Jo01b].

In-phantom Monte Carlo calculations were carried out by Benck et al [Be02] using MCNPX to predict the evolution of the measured iThemba neutron therapy beam in a water phantom. Fig. 1.6 shows the predicted changes in the energy spectrum as a function of position. The calculated energy spectra predict that the proportion of high-energy neutron to low energy neutrons increases in the neutron beam with increasing depth along the beam axis into the water phantom. In contrast the proportion of low energy neutrons to high energy neutrons increases with increasing lateral distance from the beam's axis. Although the overall trends are in broad agreement with the way in which neutrons are expected to scatter as the neutron beam passes through the water, the predictions have not been confirmed by experiment.

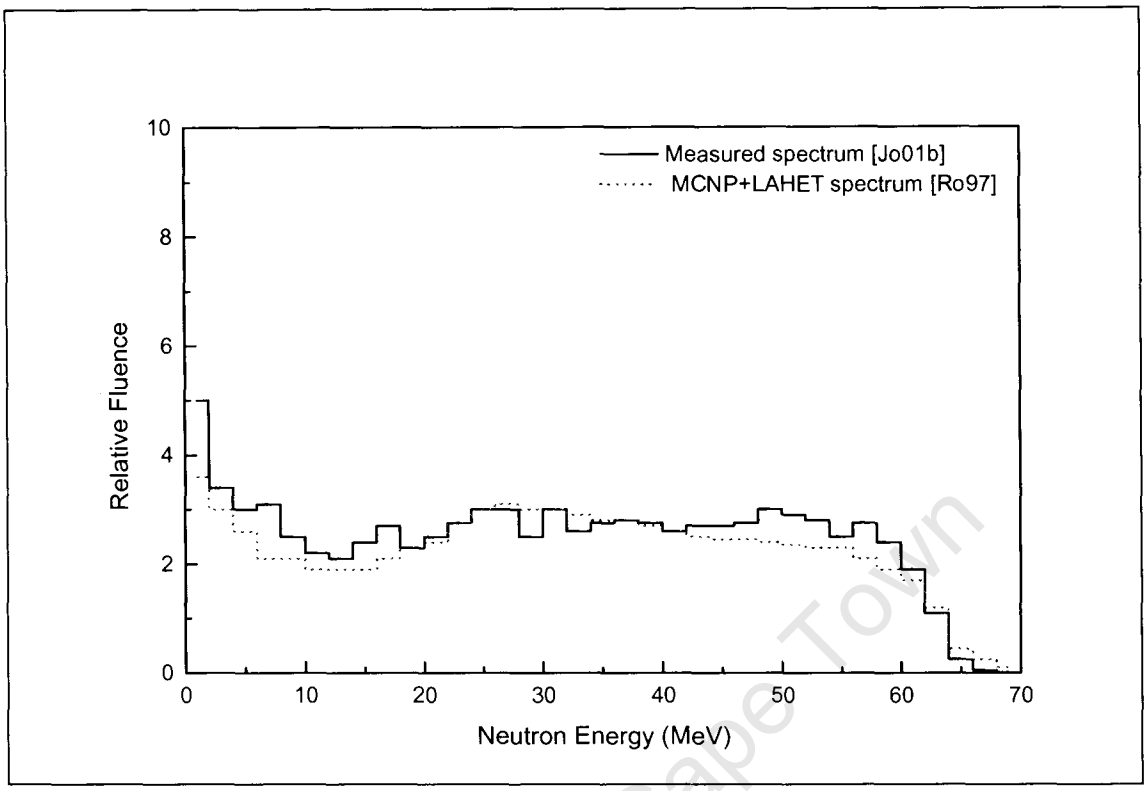

Fig.1.5 *Measured neutron energy spectra of the iThemba LABS neutron radiation therapy source compared with Monte Carlo calculations. The figure is redrawn from [Jo01b].*

Crout et al. [Cr89, Cr91] carried out in-phantom (water) measurements in the energy range 10 to 60 MeV at the Clatterbridge neutron therapy facility. For these experiments they used an NE213 scintillator as a proton recoil spectrometer and measured pulse height spectra using pulse shape discrimination (PSD) to select the proton events resulting from the interaction of neutrons in the scintillator medium. The pulse height spectra were unfolded into neutron energy spectra using a computer unfolding code RADAK [Mc75]. Their work showed that as the neutron beam passed through the water the spectrum hardened, i.e. the proportion of high energy to low energy neutrons increased, as a function of depth. This behaviour is clearly indicated in fig. 1.7 which shows the in-phantom measurements compared with the source spectrum that was determined in-air using time-of-flight. One of the problems with a spectrometer based on recoiling protons is that it cannot discriminate between protons from n-p elastic scattering events taking place in the water from protons produced by n-p elastic scattering events in the scintillator. Thus, the measured neutron energy spectrum will have a background component associated with the n-p elastic scattering

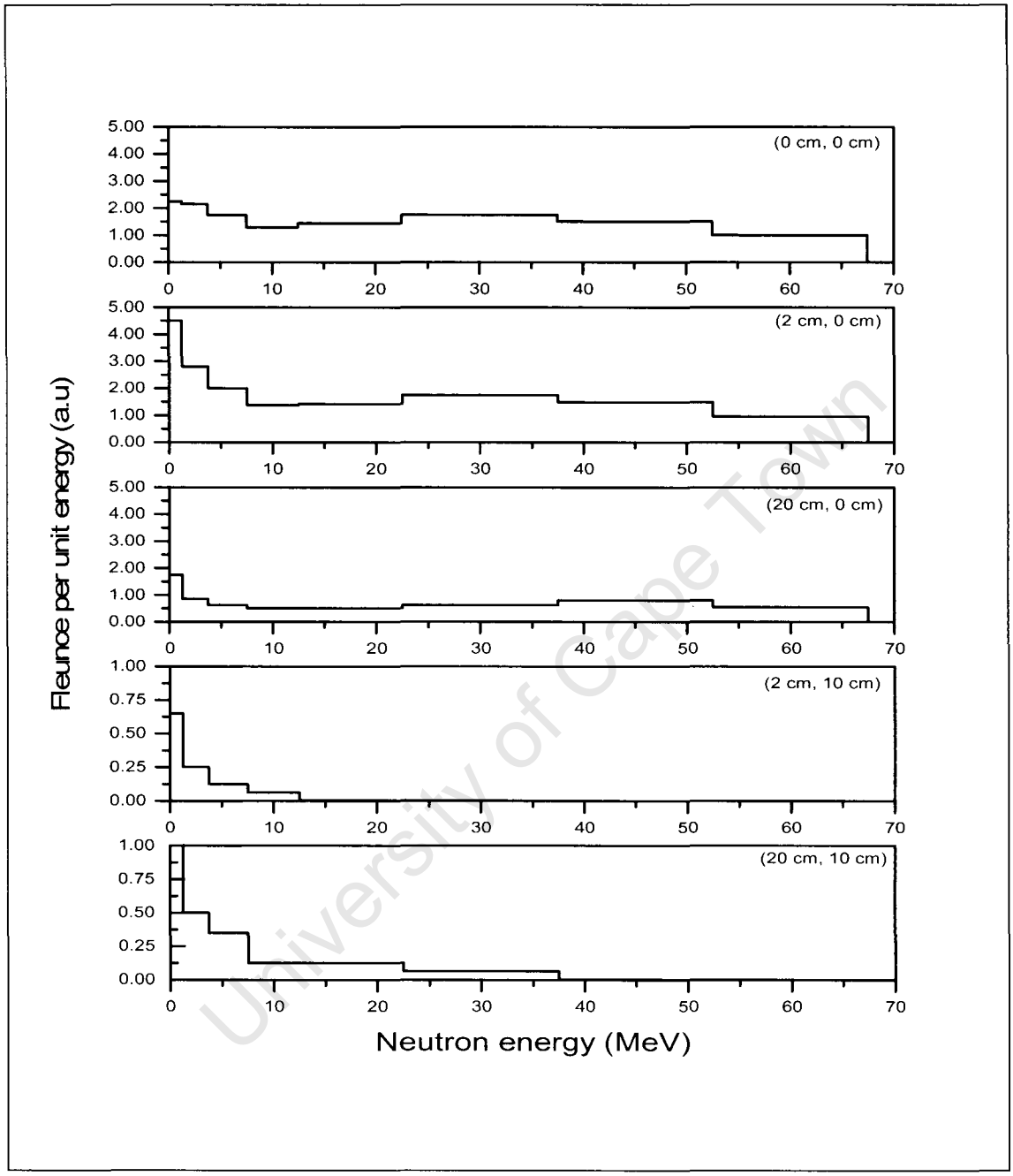

Fig.1.6 *Monte Carlo calculations of the fluence spectra at various positions in the water phantom. The figure is redrawn from [Be02]. The positions (x, y) show depth along the beam axis measured from the point at which the beam enters the phantom (x) and lateral distance from the beam axis (y).*

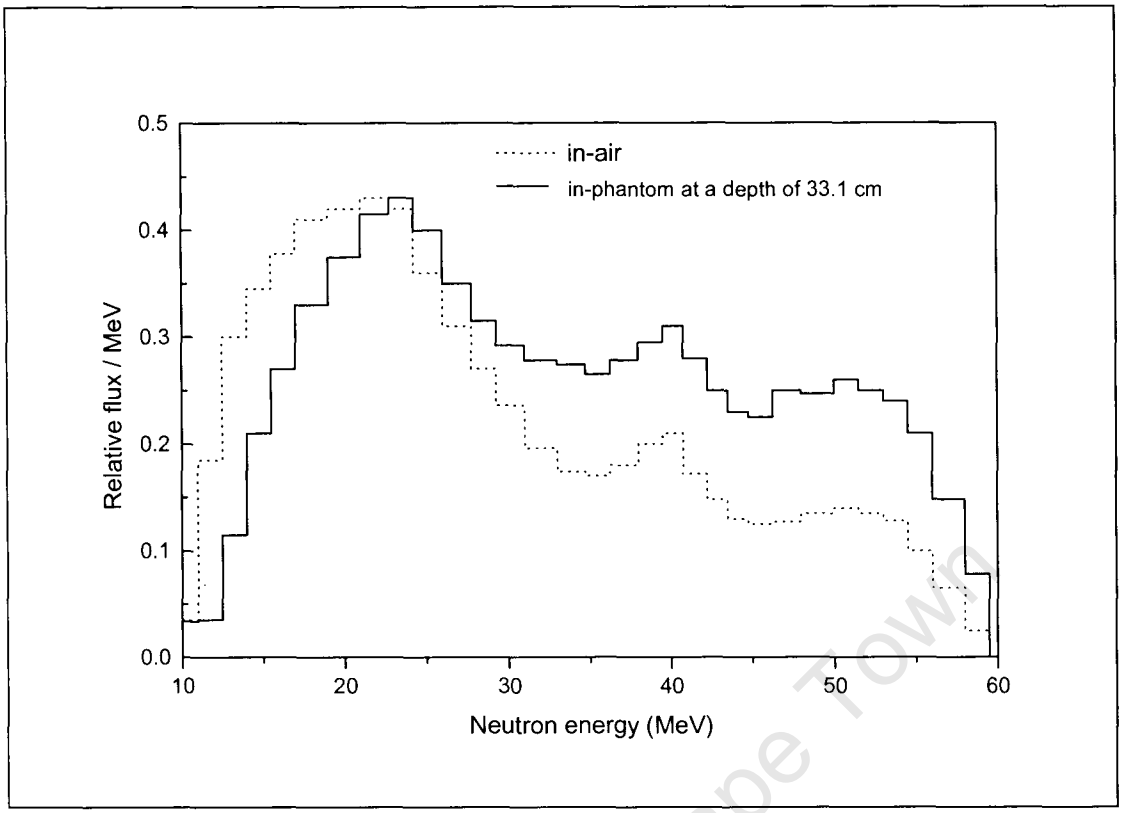

Fig.1.7 *Neutron spectra measured in-air and in a water phantom at the Clatterbridge Hospital cyclotron. The figure is redrawn from [Cr91].*

events in the water. In their work a lead cap was used to screen out the protons from the water. The effect of the lead cap on the spectrum was investigated by Monte Carlo calculation.

1.4 The present work

One of the ways to overcome the problem of background protons due to events in the water is to use a detector that does not rely on recoiling protons but on recoiling deuterons, for example. An added advantage of using a heavier charged particle is that the range of the recoiling particle will be smaller than that of a proton of the same energy. For example, the range of a 50 MeV deuteron in a deuterated liquid scintillator such as NE230 is 1.16 cm compared with 2.49 cm for a 50 MeV proton in NE213. This means that, at a particular energy, the fraction of recoiling particles that escape from a NE230 detector will be smaller than that from a NE213 detector of the same size [Br04, Zi06].

The aim of the present work was to measure neutron energy spectra as a function of position in a water phantom irradiated by neutrons of energy up to ~ 64 MeV. The measurements were carried out using a spectrometer based on a small NE230 deuterated liquid scintillator of dimensions 25 mm diameter x 25 mm. Thus, for the in-phantom measurements the NE230 detector assembly was immersed in the phantom and moved under computer control to positions along and off the beam axis. In the present study a series of detailed measurements was taken at positions in the phantom along the axis of the neutron beam while exploratory runs were made off the beam axis. Pulse height spectra produced by recoil deuterons and heavier charged particles generated in the scintillator by neutrons were selected by means of PSD. These pulse height spectra were unfolded into neutron energy spectra; using the Bayesian unfolding code MAXED [Re02].

For the purpose of unfolding, the required pulse height response functions of the detector were obtained by measurement. Pulse height response functions were determined at 43 quasi-mono-energetic neutron energies ranging from 5 to 64 MeV. The pulse height response functions were derived from time-flight-measurements as follows: A number of different targets were used to produce as wide a range of neutron energies as possible. Specific neutron energies were selected by imposing time windows appropriately, during off-line analysis.

Experiments were conducted at the neutron time-of-flight facility at the iThemba LABS in South Africa. Neutrons of energy up to ~ 64 MeV were produced by bombarding a pulsed beam of 66 MeV protons from the iThemba LABS separated sector cyclotron onto either a Li metal target or a Be metal target or a graphite target. Two types of measurements were made in the experiments (a) in-air measurements and (b) in-phantom measurements. The in-air measurements were used for two purposes: (1) to determine the response matrix of the NE230 detector as mentioned above and (2) to determine the efficiency of the NE230 detector as a function of neutron energy. The latter exercise was carried out with reference to an NE213 detector. In addition, the validity of the unfolding procedure was checked by comparing energy spectra obtained from time-of-flight measurements with energy spectra obtained by unfolding the associated pulse height spectra. The results from the in-phantom measurements were compared with Monte Carlo simulations.

CHAPTER 2

EXPERIMENTS AND DATA REDUCTION

2.1 Neutron production

As described in section 1.4 two types of measurements were carried out: (a) in-air and (b) in-phantom. Experiments were conducted at the neutron time of flight facility at the iThemba LABS in Faure, outside Cape Town, South Africa [ITH]. Fig. 2.1 is a schematic diagram showing the details of the neutron beam line, the shielding in the experimental area and the positions of the detectors including the neutron monitor. Neutrons were produced by bombarding either a Li metal target (thickness 1 mm) or a Be metal target (thickness 10 mm) or a graphite target (thickness 10 mm) with a pulsed beam of 66 MeV protons from the iThemba LABS separated sector cyclotron. A 2 m thick shielding wall (concrete and iron) separated the experimental area from the target. A circular aperture (25 mm diameter) in the wall provided a collimated neutron beam at angle 0° to the proton beam direction. A neutron beam monitor was permanently mounted in a separate neutron beam that viewed the target from an angle of 8° to the proton beam direction. The neutron beam monitor used was a NE213 liquid organic scintillator, which was optically coupled to a RCA8850 photomultiplier using silicone jelly. The distance from the target to the neutron monitor was 8.05 m. Protons that passed through the targets were removed from the neutron beam by a system of clearing magnets into a beam dump including a Faraday cup. Protons that were not removed from the neutron beam by the clearing magnets were stopped by a 6.5 cm thick graphite block put in front of the collimator side facing the target. The in-phantom measurements were carried out in the 0°- neutron beam with the phantom mounted at a distance of 7.53 m (to the front face of the tank) from the target. For the in-air measurements the detector was mounted in the 0°- neutron beam at a distance of 7.71m from the target.

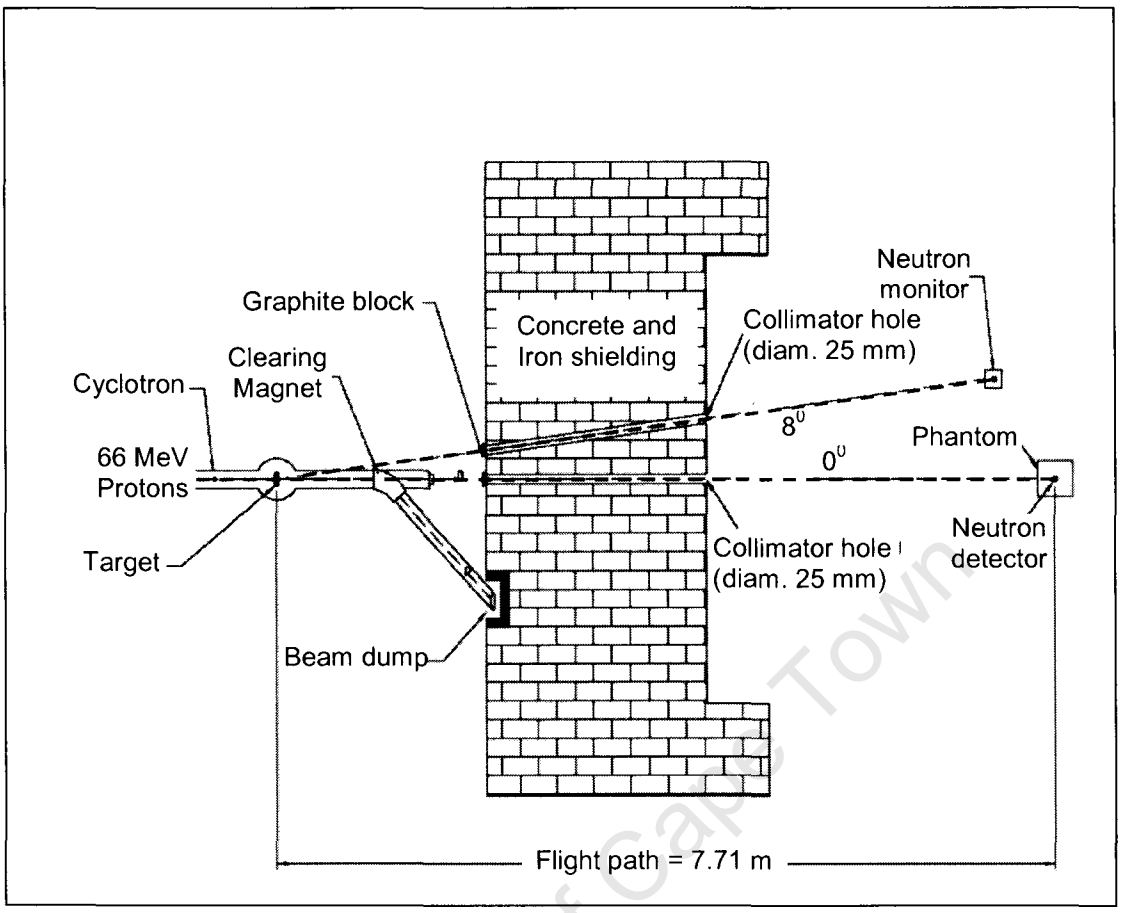

Fig. 2.1 *Schematic diagram of the neutron beam line, shielding and detector.*

2.2 Beam profile measurements

A cylindrical anthracene crystal (10 mm diam. x 20 mm) was used for making measurements of the beam profile. The crystal was optically coupled to a RCA8850 photomultiplier using silicone jelly. For the neutron beam profile measurements the anthracene detector was mounted horizontally in air in the 0°- neutron beam with its axis aligned parallel to the 0°- neutron beam. The measurements were taken at a position of 7.71m from the target. Horizontal and vertical scans were made across the neutron beam, recording the number of events detected in the crystal for a fixed integrated proton charge. Fig. 2.2 shows the results of the measurements obtained for the scans as a function of distance from the centre position in the beam. The intensity profile of the neutron beam was found to be uniform over a circular area of diameter 50 mm. Thus, the dimensions of the detectors used in the experiments (see section below) were such that the beam fully illuminated the detectors at all the positions in-air and along the beam axis in the phantom at which measurements were taken.

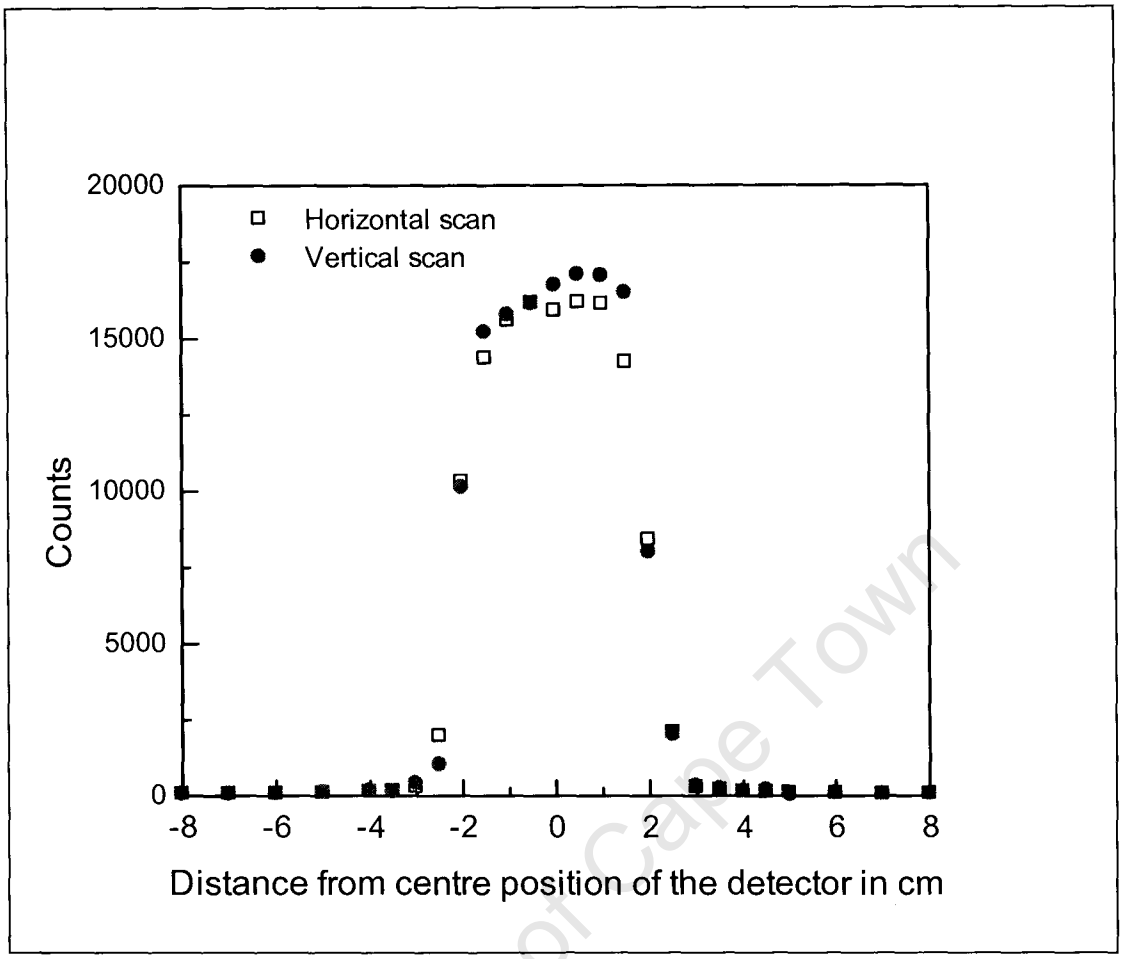

Fig. 2.2 *Beam profile measurements obtained for the horizontal and vertical scans as a function of distance from the centre in the 0°- neutron beam. The detector was placed in the 0°- neutron beam at a distance of 7.71m from the target.*

2.3 Neutron detectors

Two neutron detectors were used for the measurements. Both detectors were developed locally [Pa73, Bu90]. The first comprised a cylindrical cell of NE213 organic liquid scintillator (diam. 50 mm x 50 mm), optically coupled to an RCA8850 photomultiplier with silicone jelly. This detector system was used only for in-air measurements. The second detector consisted of a single cylindrical cell of deuterated liquid organic NE230 scintillator (diam. 25 mm x 25 mm) encapsulated in glass. The window of the cell was optically coupled to a RCA8850 photomultiplier with silicone jelly. The scintillator was inserted into a thin latex sheath and the photomultiplier into a thin walled PVC tube to ensure that the detector assembly was completely watertight. This detector system was used both for the in-phantom measurements as

well as for in-air measurements. Table 2.1 lists the physical properties of the NE213 and NE230 scintillators.

Table 2.1: *Physical properties of the NE213 and NE230 liquid scintillators [Kn89]*

	NE213	NE230
Density	0.874 g.cm^{-3}	0.945 g.cm^{-3}
Mass % of D	0	14.2
Mass % of C	92.3	85.7
Mass % of H	7.7	0.1
H:C atomic ratio	1.211	0.984

Both the NE230 and NE213 scintillators have excellent capabilities for discriminating against gammas as well as between protons, deuterons and alphas by means of pulse shape discrimination [Pa75, Br04, Zi06, Br07]. As noted in section 1.2.2, the neutron detector system that is used for the in-phantom measurements should distort the measured spectra as little as possible. Thus, the effect of the NE230 detector assembly on the measured spectra was investigated using the Monte Carlo code MCNPX. The results indicated that the NE230 detector assembly would have a negligible effect on the measured spectra (see section 4.3.1). NE213 and NE230 no longer in use and alternative to these are BC501A or EJ301 and BC537 or EJ315 which can be obtained from Bicron Radiation measurement products or Eljen Technology.

2.4 Electronics

Fig. 2.3 shows details of the electronic circuit that was used in the experiments. Two independent signal processing chains were set up in order to process the signals from the neutron detector (either NE213 or NE230) and the neutron monitor, respectively. Signals were produced from either the NE230 detector assembly or the NE213 detector, the beam monitor detector and the time reference pulses from the RF cycle of the injector cyclotron. In this case, for the 66 MeV protons produced by the cyclotron, the time reference pulses were 61 ns apart. However, in order to prevent overlapping of events from successive beam pulses every fifth pulse was selected giving a time spacing of 305 ns between pulses. A timing output T_{stop}, synchronized

to this pulse was generated and used to stop the two time-to-amplitude converters TAC_A and TAC_M that were used for timing neutrons in the circuit.

The output from the anode of the photomultiplier tube of the neutron detector (either NE213 or NE230) was fed into a modified Link System Model 5010 pulse shape discriminator unit ($LINK_A$) [Ad78], which produced four outputs, L, F, $T_{start(A)}$ and a logic pulse n. The pulse height, L was generated by integrating the scintillation pulse over a period of 500 ns while the F signal was generated by integrating over 30 ns [Sm87]. The electronic threshold for the neutron detectors was set at neutron energy of 5 MeV. The timing signal $T_{start(A)}$ was used to start the (TAC_A) that measured the neutron time of flight, T. The logic pulse n was produced by the pulse shape discrimination circuitry and was used to discriminate between the gamma and neutron events. The output from the dynode of the photo multiplier tube of the neutron detector was fed into a pre-amplifier and amplifier chain and used as an independent pulse height measurement, parameter D.

The output from the anode of the photomultiplier tube of the monitor detector was fed into $LINK_M$, which was used to select neutron events identified by PSD via the logic signal n. During calibration runs it was also possible to select an alternative logic signal ($n\gamma$) that allowed all events i.e. those associated with both neutrons and gamma rays to be included. $LINK_M$ also provided a timing signal $T_{start(M)}$, which was used to start TAC_M.

Two universal coincidence (UCO) units were used as follows. UCO_A formed the basis of the coincidence logic for the neutron detector while UCO_M processed events associated with the neutron monitor. UCO_A, produced an output pulse whenever the following two signals were present at the same time, namely, the time window (w) from TAC_A and PSD (n) from $LINK_A$. A pulse from the computer indicating that it was "not busy" was also fed into the UCO_A. The output pulse from UCO_A was used to open a gate that allowed T, L, F and D to be recorded by the computer. The events passed were used to gate the linear gate and stretcher (LGS) units allowing the data to be passed to the ADCs for analogue to digital conversion, and also to trigger the acquisition computer. Although T was recorded when either the NE213 or NE230 detector was being used it played no role in the off-line analysis of the NE230 data.

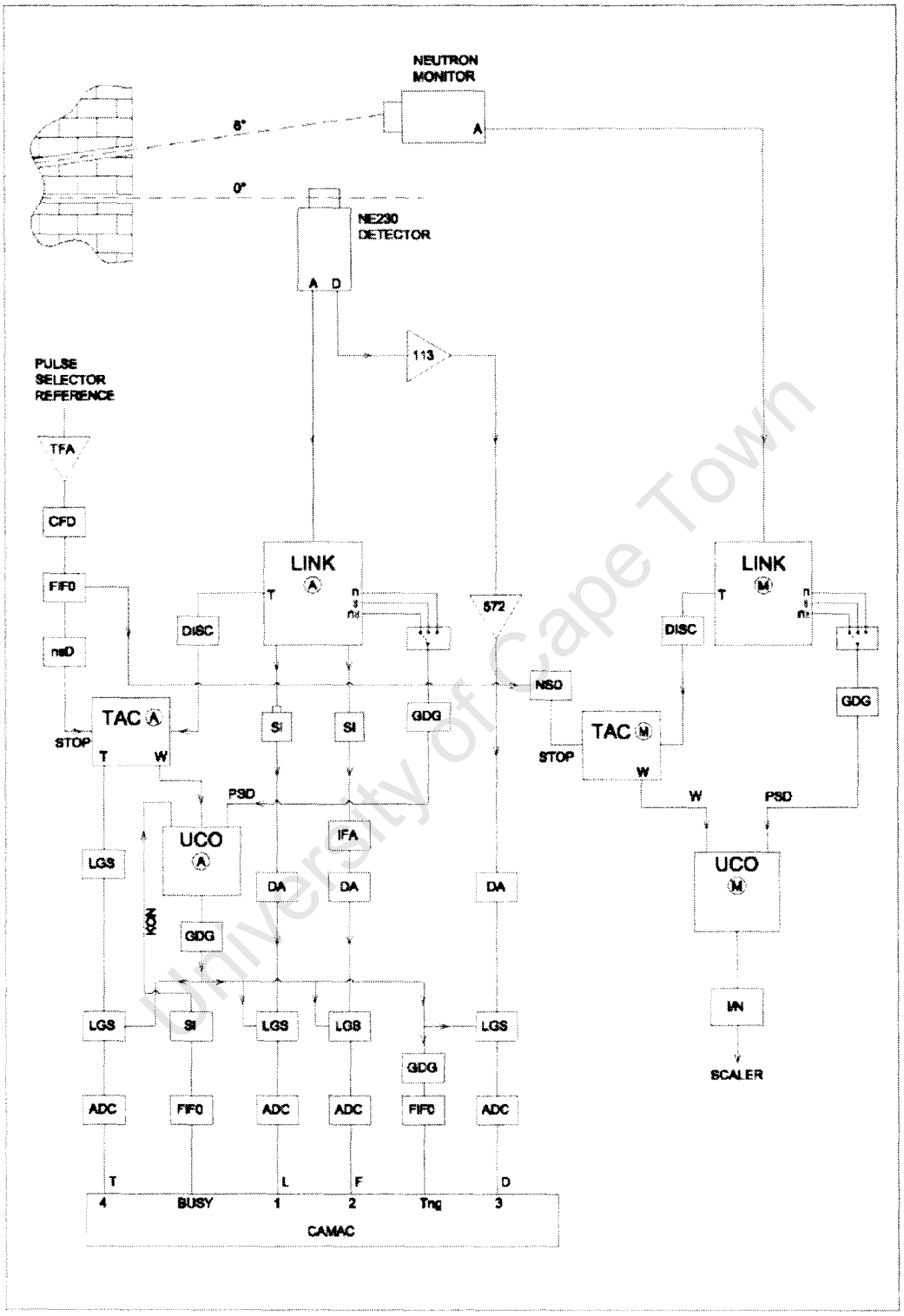

Fig. 2.3 *Diagram of the full electronic circuit used for pulse processing in the experiments.*

The coincidence logic for the neutron monitor was controlled by UCO_M, which produced an output pulse whenever the following two signals were present at the same time, namely, the time window (w) from TAC_M and PSD (n) from $LINK_M$. The output pulse from UCO_M was fed directly into a scalar and recorded.

All phases of the data acquisition were monitored on a system of displays to detect any electronic drifts. The output from the ADCs were fed into a CAMAC interface which was linked to VAX 730 computer running XSYS data acquisition software, via a Micro Branch Driver. Event by event data were recorded for the parameters L, F, T and D in memory and buffered in 4k blocks to magnetic tape for off-line analysis. The analysis of the data was done off-line using the computer program GNU [GNU], which is available at the University of Cape Town.

2.5 Particle identification and event selection

Ionisation and excitation produced by charged particles released in neutron interactions in the scintillator medium gave rise to scintillation light. The scintillation time can be described as the sum of a fast exponential component (with a decay time of a few nanoseconds) and a slow exponential component (with a decay time of several hundred nanoseconds). The intensities of these fast and slow scintillation components are dependent on the type and energy of the charged particle that produced it [Bi64]. This provides a method to discriminate between the different charged particles and forms the basis of pulse shape discrimination (PSD) [Br79, Pe79, Br88]. As pointed out in section 2.4, by using the PSD function of the LINK modules, events in the scintillators associated with gamma rays (detected via Compton electrons) were rejected and only those associated with neutrons (detected via recoiling charged particles, other than electrons) were accepted. In the off-line analysis, PSD was further used to identify the different charged particles produced from neutron interactions in the NE230 and NE213 detector mediums. This was carried out by computing a scintillation pulse shape parameter, S from the L and F outputs from $LINK_A$ as follows

$$S = L - kF + C \tag{2.1}$$

where k and C are arbitrary constants that are chosen to optimize the differences between the particle loci in a display of L versus S . The value of k determines the angle of the loci in the LS-display and the value of C determines the position of these loci along the S-axis. The events corresponding to different ionising particles each have a unique set of L and S values which depend on the type, and the energy of the ionising particle. Figs. 2.4 and 2.5 show perspective plots of counts (vertical) versus pulse height (L) and pulse shape (S) for events detected by the NE213 detector and NE230 detector respectively, when exposed to neutrons from 66 MeV protons incident on the 1 mm thick Li-target.

It can be seen from these plots that the events corresponding to different ionising particles lay on well-defined ridges that are resolved in the LS-plane. At higher values of L these ridges are clearly separated, but the separation diminishes with decreasing L due to poorer photomultiplier statistics. The ridges shown in fig. 2.4 for the events in NE213 are associated with protons (p) arising from n-p elastic scattering and n-C reactions, deuterons (d) and alphas (α) from n-C reactions [Bu90, Br07]. The less prominent ridge (ep) to the left of the (p) ridge arises from the detection of escaping charged particles, mainly protons that exit the scintillator volume. The Compton electrons that would have given rise to a ridge to the left of the (ep) ridge have been suppressed by the LINK as noted earlier. The ridges shown in fig. 2.5 for the events in NE230 are associated with protons (p) arising from the breakup of deuterons and n-C reactions, charged particle escapes (ep), deuterons (d) from n-d elastic scattering and n-C reactions, alphas (α) from n-C reactions. The continuum between the d- and α-ridges is attributed to heavier charged particles like tritons or to the simultaneous detection of two or more charged particles [Pa73, Br07].

The figs. 2.4 and 2.5 also show the LS-cuts, C_1, C_2, C_3 and C_4 used to separate and select all the proton and heavier charged particle events in the NE213 detector and all the deuteron and heavier charged particle events in the NE230 scintillator. The cuts were set where the ridges of the different particle events overlap least. Fig 2.6 show pulse shape (S) spectra for different pulse height (L) channels for the events measured in the NE230 scintillator. It can be seen from the spectra that the cut C_3 will not separate all the proton events from the deuteron and heavier charged particle events because of the overlap of the ridges. It was calculated that the proton events "leaking"

through to the deuteron and heavier charged particle ridge was of the order of 4%. The projection of these events onto the *L*-axis gives the corresponding pulse height spectra for the NE213 detector (fig. 2.7(a)) and the NE230 detector (fig. 2.7(b)), respectively.

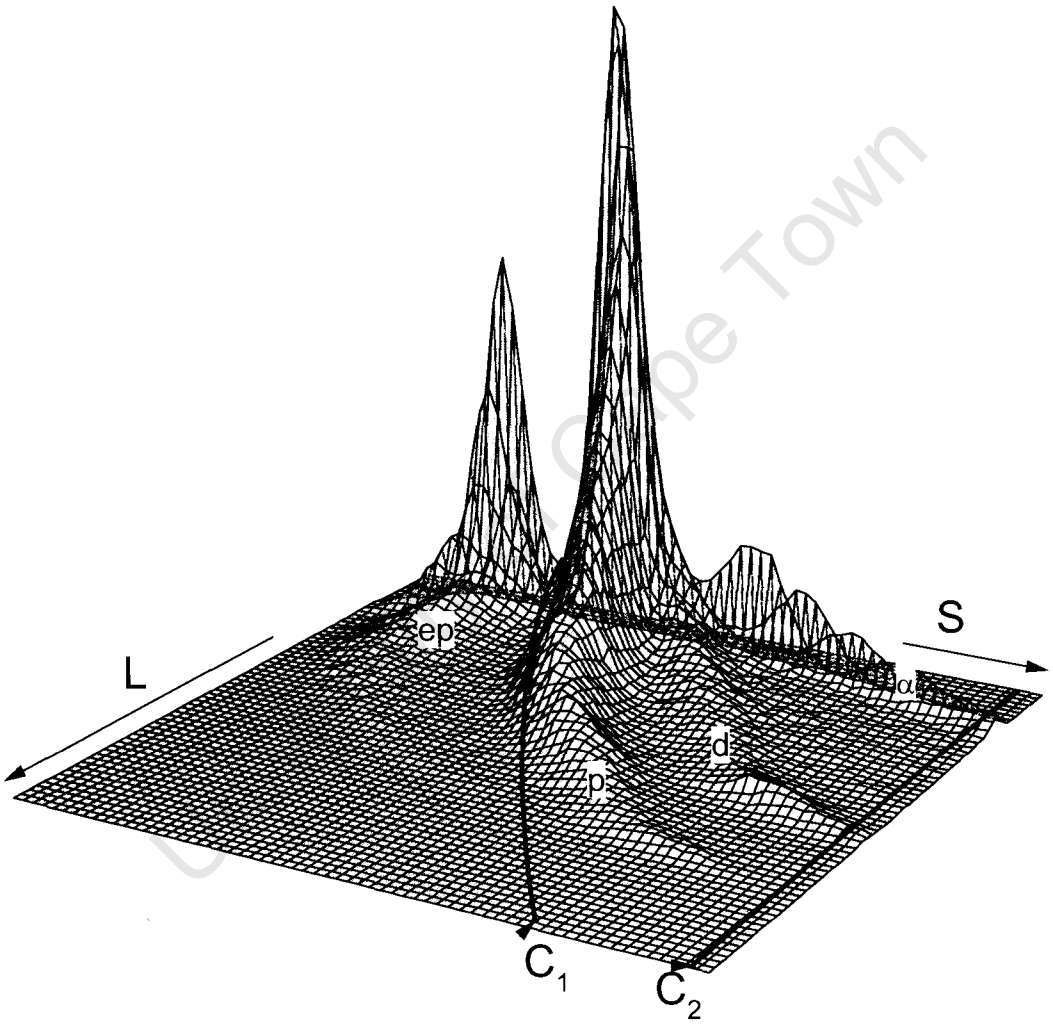

Fig. 2.4 *Perspective views of counts (vertical was set to 8000 counts) as a function of pulse height, L, and pulse shape, S, for the charged particle events detected by NE213 detector when exposed to neutrons from 66 MeV protons incident on the 1 mm thick Li-target. The ridges correspond to protons (p), escaping protons (ep), deuterons (d) and alphas (α). The solid lines in the plot indicate the LS-cuts C_1 and C_2 used to select the proton and heavier charged particle events. (See figure 2.7(a)).*

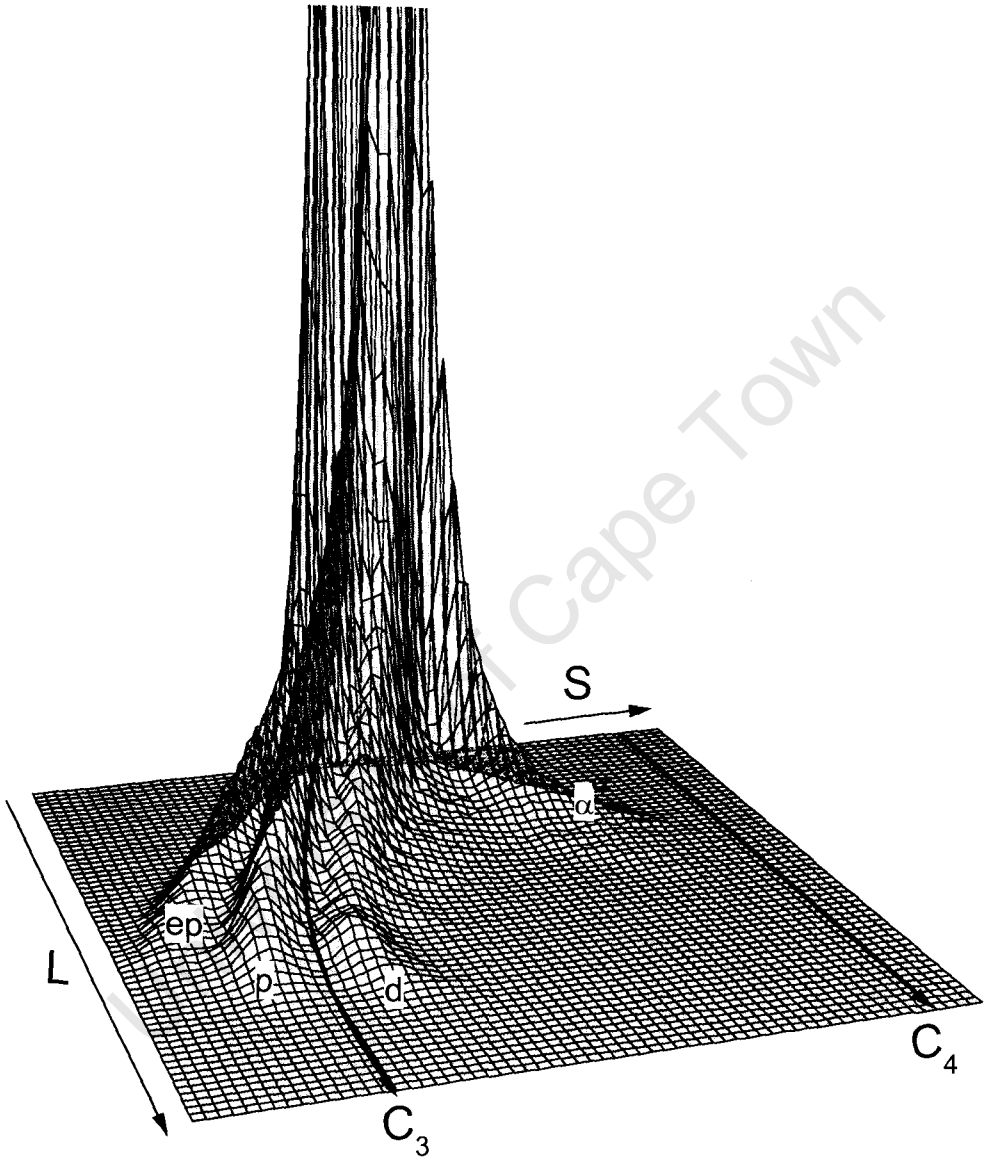

Fig. 2.5 *Perspective views of counts (vertical was set to 8000 counts) as a function of pulse height, L, and pulse shape, S, for the charged particle events detected by NE230 detector when exposed to neutrons from 66 MeV protons incident on the 1 mm thick Li-target. The ridges correspond to protons (p), escaping protons (ep), deuterons (d) and alphas (α). The solid lines in the plot indicate the LS-cuts C_3 and C_4 used to select the deuteron and heavier charged particle events. (See figure 2.7(b))*

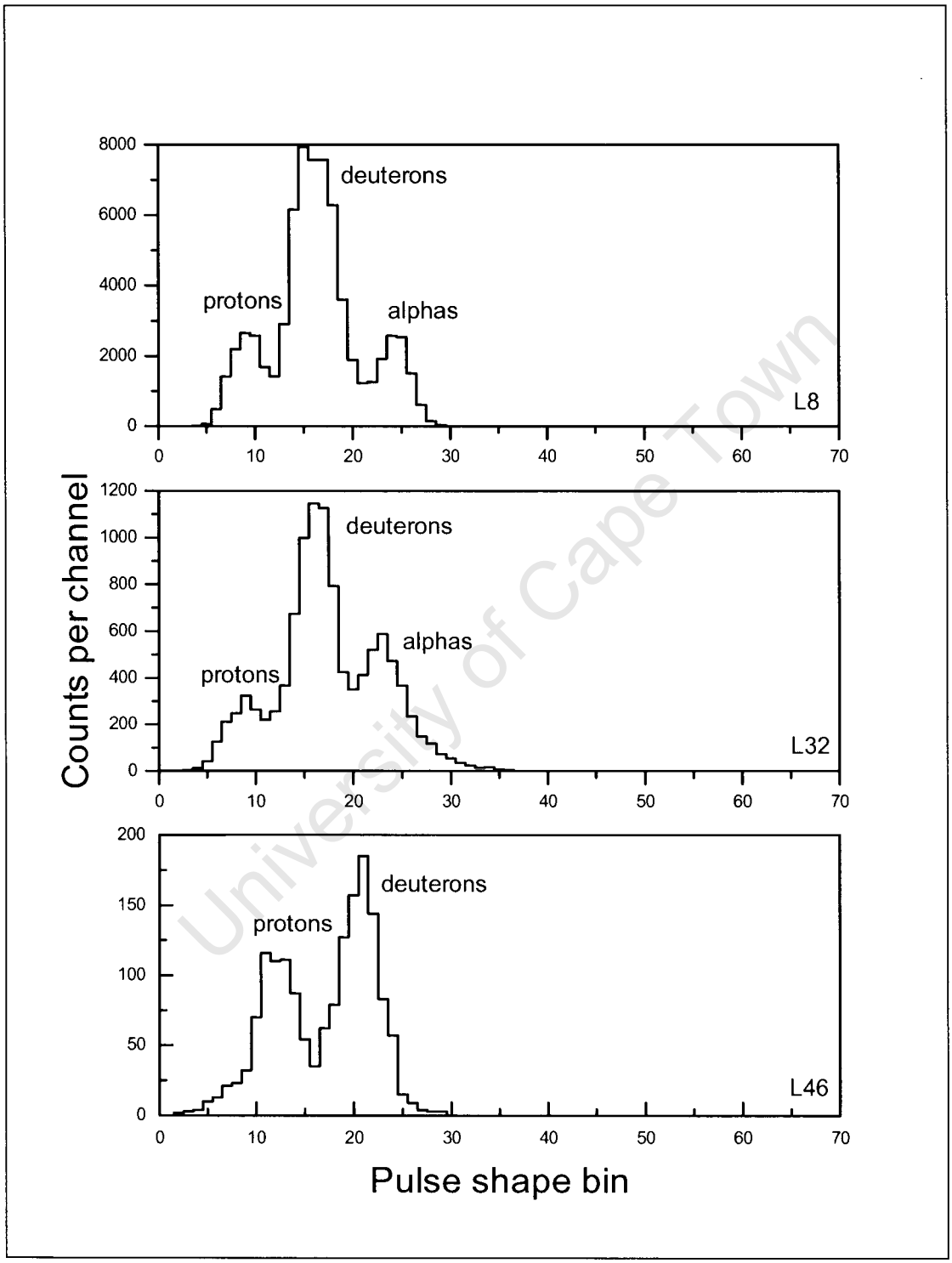

Fig.2.6 *Pulse shape S spectra for different pulse height L channels for the charge particle events detected by NE230 when exposed to 66 MeV protons incident on the 1 mm thick Li-target.*

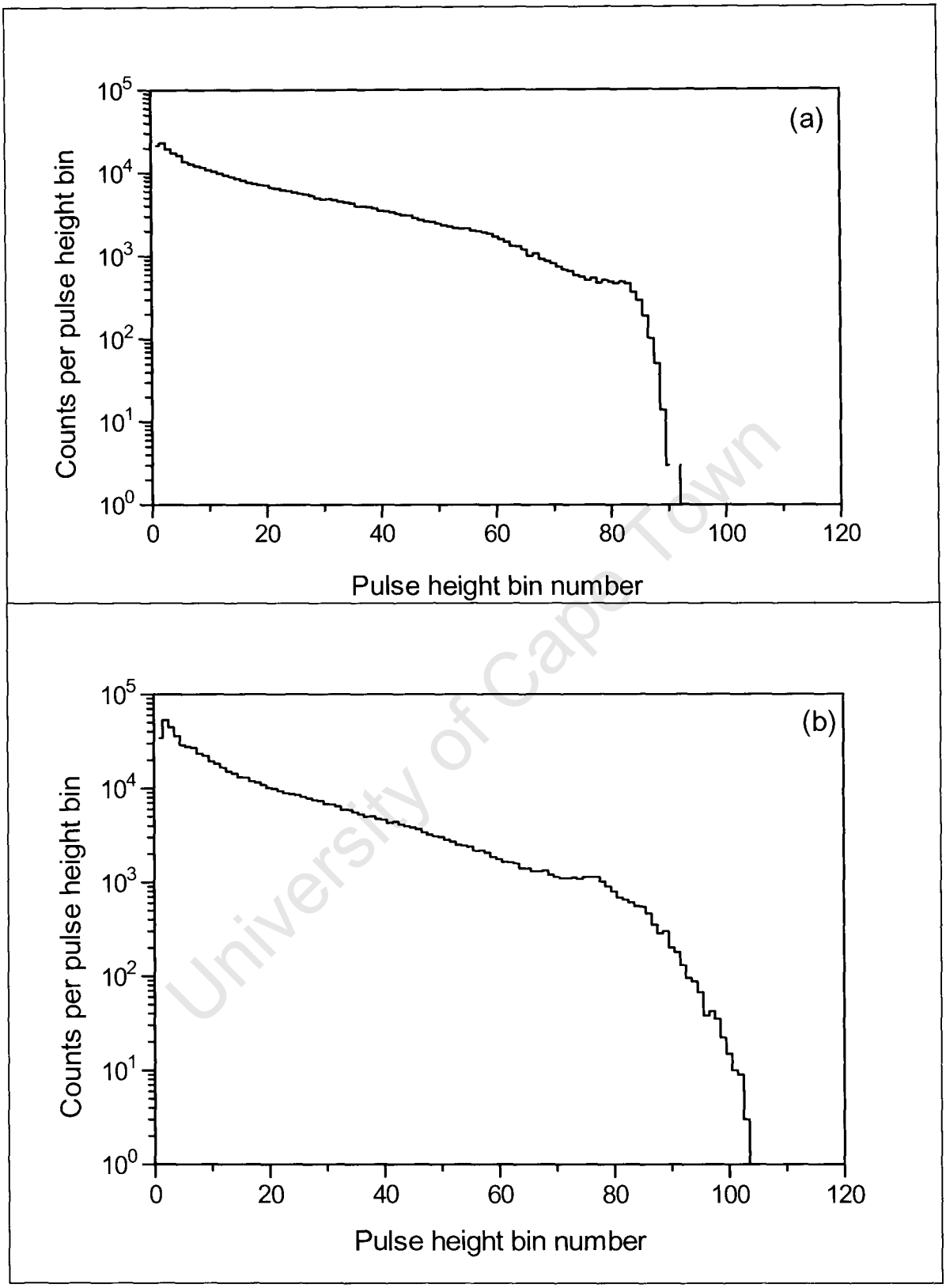

Fig. 2.7(a) *Pulse height spectrum measured by the NE213 detector for proton and heavier charged particle events and* (b) *pulse height spectrum measured by the NE230 detector for deuteron and heavier charged particle events, when exposed to neutrons produced by 66 MeV protons incident on a 1 mm thick Li-target.*

2.6 In-air measurements

A series of measurements in-air were made for the following purposes: (a) to determine the response matrix required for the unfolding of the pulse height spectra and (b) to measure the detector efficiency of the NE230 detector (relative to n-p elastic scattering). Ideally, a "white" neutron source covering the energy range from 5 to 64 MeV was required for the exercise. The most appropriate, available target for the measurements was a 10.0 mm thick ^{12}C. However, although the ^{12}C target provided a suitable target, the high Q-value (-18.14 MeV, see table 2.2) of the $^{12}C(p,n)^{12}N$ reaction restricted the neutrons produced to a maximum energy of about 48 MeV because the proton energies produced by cyclotron was limited to 66 MeV. In order to cover the higher energies up to 64 MeV a 10.0 mm thick ^{9}Be target was also used. This allowed neutrons of up to 63 MeV to be produced. In addition the 1mm thick ^{7}Li target (used for the in-phantom measurements) was also used to obtain 64 MeV neutrons. Thus, measurements were made using neutron beams produced by all three targets, Li, Be and C. A series of time-of-flight measurements was carried out with both the NE213 and NE230 neutron detectors. Each detector was mounted horizontally in air in the 0°- neutron beam with its axis aligned perpendicular to the 0°- neutron beam at a distance of 7.71m from the respective targets. Six measurements were made, three with each detector and one of each target. Table 2.2 shows the set of measurements done with the neutron detector and target used for each measurement.

Table 2.2 *Summary of the in-air measurements*

Measurement	Detector used	Target (mm)	Q-values	$E_n(max)$
M1	NE213	Li (1)	-1.64 MeV	64 MeV
M2	NE213	Be(10)	-1.85 MeV	63 MeV
M3	NE213	C(10)	-18.12 MeV	48 MeV
M4	NE230	Be(10)	-1.85 MeV	63 Mev
M5	NE230	C(10)	-18.12 MeV	48 MeV
M6	NE230	Li(1)	-1.64 MeV	64 MeV

2.6.1 Pulse height (L) and time-of-flight (T) spectra

Pulse height spectra (in ADC channels (L)) and the corresponding time-of-flight spectra (in ADC channels (T)) were obtained for each target for neutrons of energy 5 to 64 MeV. Pulse height spectra measured by the NE213 detector for proton and heavier charged particle events for the different targets are shown in fig. 2.8(a) and pulse height spectra measured by the NE213 for deuteron and heavier charged particle events for the targets are shown in fig. 2.8(b). In each plot the pulse height spectra of the C-target has fewer high pulse height pulses than the spectra of the other targets. This may be attributed to the high Q-value (see table 2.2) of the $^{12}C(p,n)^{12}N$ reaction. The effect of target thickness is also evident in these spectra in the case of the thin Li-target the spectra has well-defined upper edges and one can identify the upper pulse height limits for n-C reactions, n-p (fig. 2.8(a)) and n-d (fig. 2.8(b)) elastic scattering in the respective spectra while the thicker targets have broader upper edges corresponding to a wide range of energies.

Figs. 2.9 and 2.10 show the neutron time-of-flight spectra of the targets measured by the NE213 and NE230 detectors, respectively. The spectra measured by the detectors have similar features for the same target. The effect of the Q-values (see table 2.2) for the respective (p,n) reactions can also be seen from the upper edges of the time of flight spectra that shift towards lower time-of-flight channels with increasing Q-value. The effect of target thickness is also evident in the spectra as the thicker targets have spectra with broader peaks. The time-of-flight spectrum of the ^{7}Li -target (Q = -1.64 MeV) shows that the highest energy neutrons of 64 MeV produced fall, within a sharp high-energy peak. This peak arises principally from the transition to the unresolved ground and first excited states of ^{7}Be in the $^{7}Li(p, n)^{7}Be$ reaction. The rest of the spectrum consists of a broad lower energy tail, which arises from excitation of the higher states in ^{7}Be or from break up reactions leading to three or more particles in the final state. The time of flight spectrum of the ^{9}Be target shows that the highest energy neutrons of 63 MeV target (Q = -1.85 MeV) produced, fall within a broader peak, which arises from the transition to the unresolved ground, of the first and second excited states of ^{9}Be in the $^{9}Be(p,n)^{9}B$ reaction. The peak in the time of flight spectrum of the ^{12}C target is much broader than in the case of the peaks in the spectra of the Li-target and Be-target. The neutrons (most energetic produced

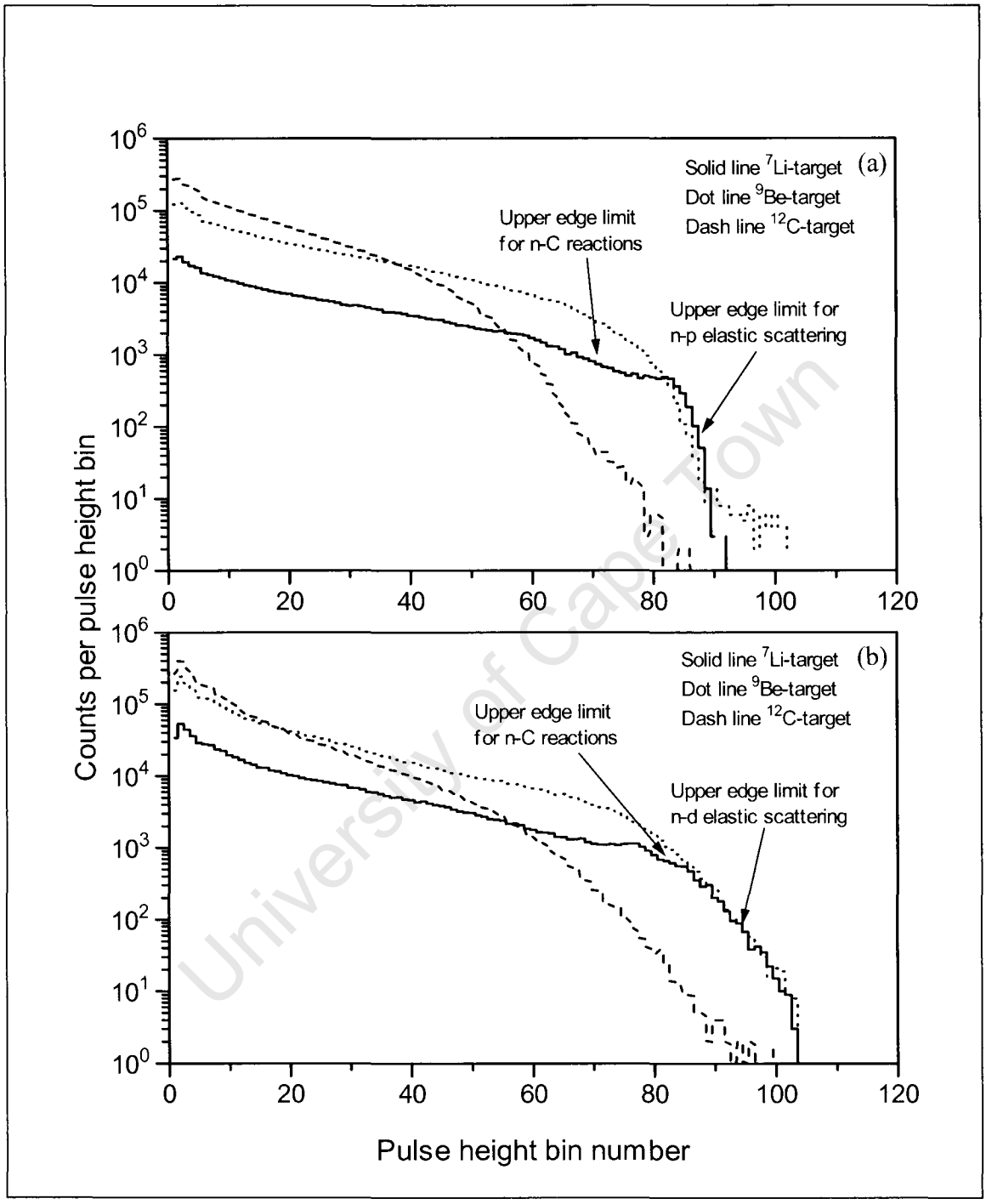

Fig. 2.8(a) *Pulse height spectrum measured by the NE213 detector for proton and heavier charged particle events and* (b) *pulse height spectrum measured by the NE230 detector for deuteron and heavier charged particle events, when exposed to neutrons of energy 5 to 64 MeV produced by 66 MeV protons on the 1 mm thick Li-target, 10 mm thick Be-target and 10 mm thick C-target.*

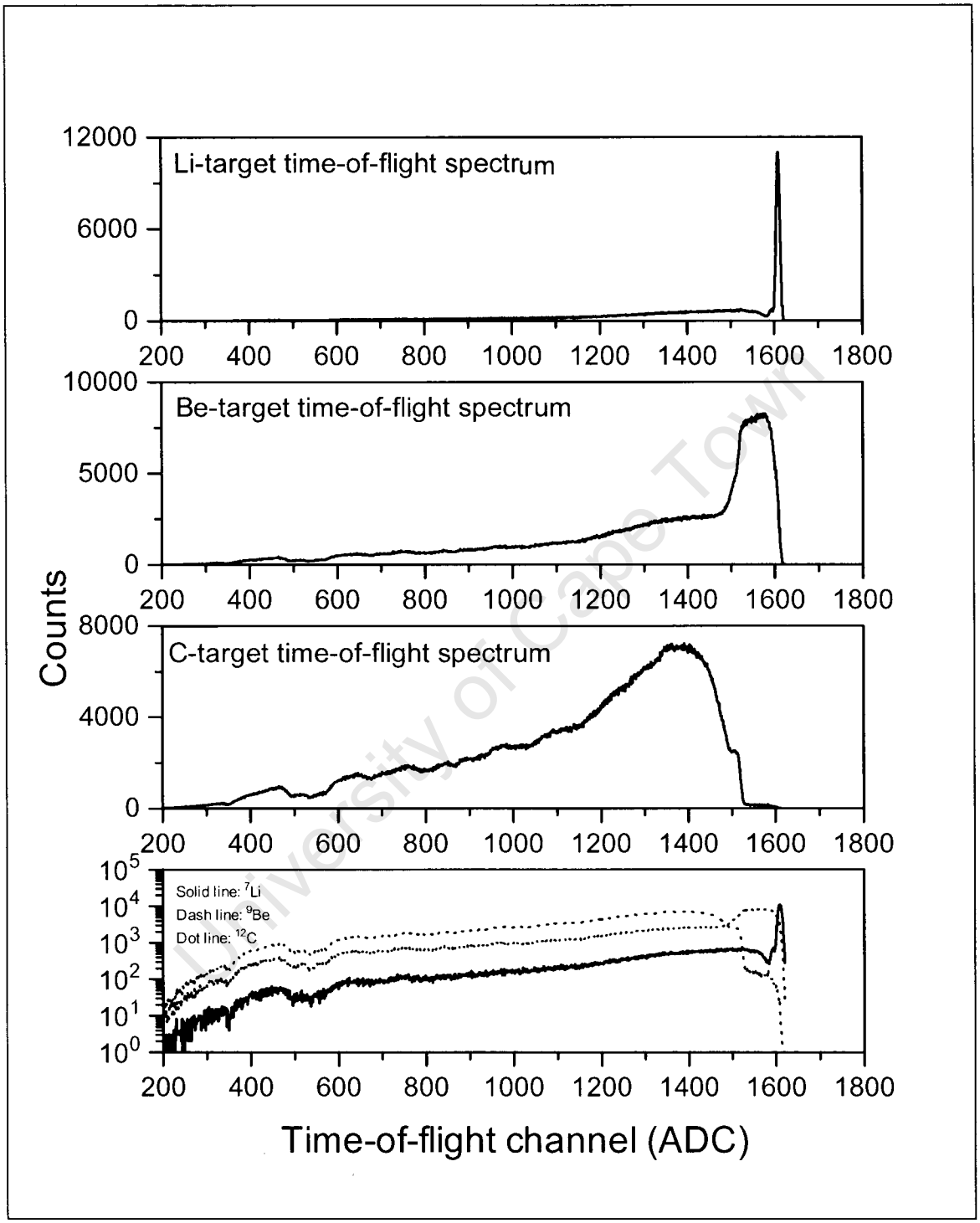

Fig. 2.9 *Time-of-flight spectra of the Li-target, Be-target and C-target measured by the NE213 detector for neutrons of energy 5 to 64 MeV.*

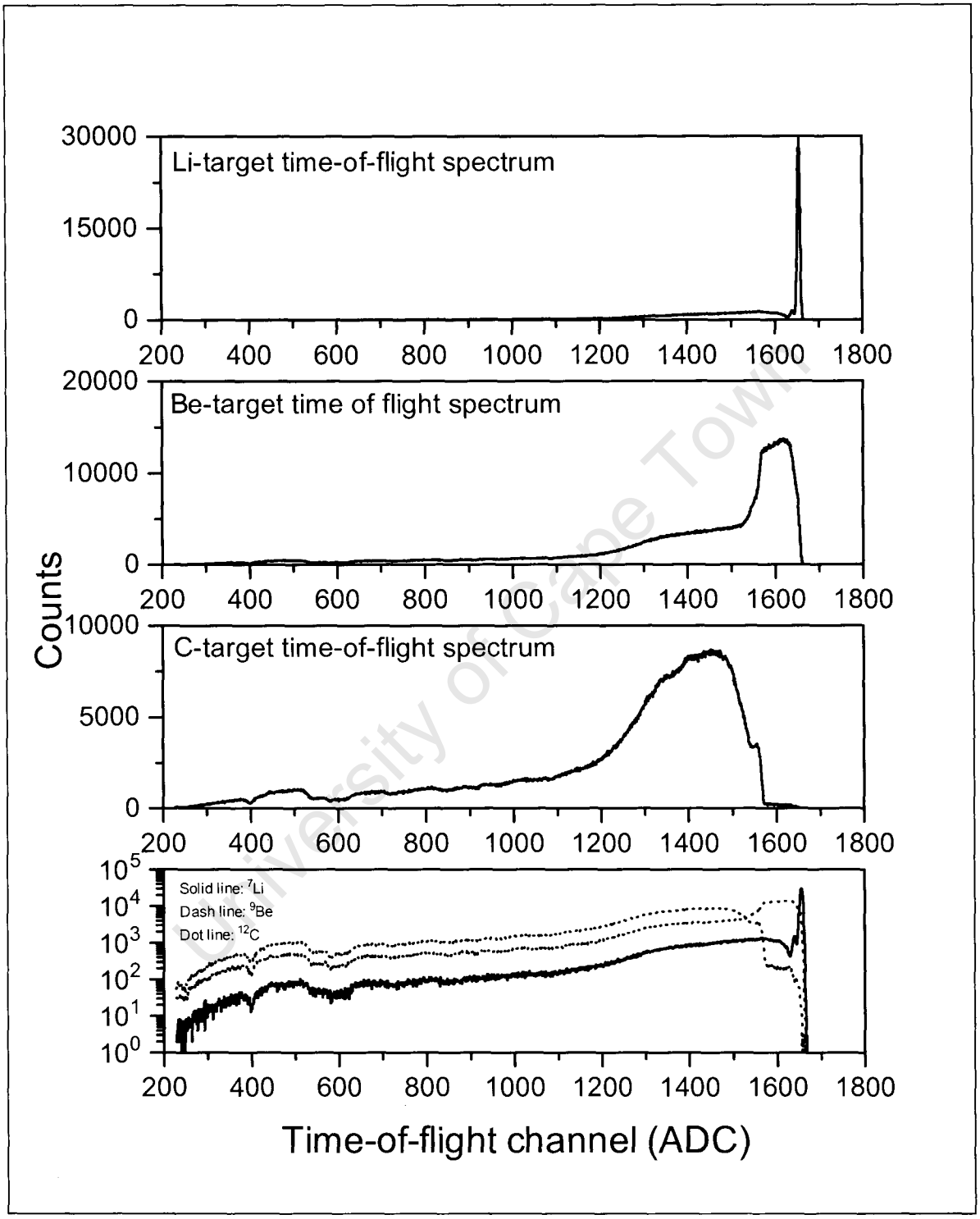

Fig. 2.10 *Time-of-flight spectra of the Li-target, Be-target and C-target measured by the NE230 detector for neutrons of energy 5 to 64 MeV.*

48 MeV and Q = -18.12 MeV) in the peak arises from the transition to the unresolved ground and excited states of ^{12}B in the $^{12}C(p,n)^{12}B$ reaction which cannot be resolved by the energy resolution of the detectors. The humps observed in the time-of-flight spectra between T = 300 and 900 ADC are attributed to resonances of ^{12}C associated with the 6.5 cm thick graphite block put in front of the collimator side facing the target.

2.6.2 Time-of-flight to neutron energy calibration

For calibration purposes two short runs in which gamma events were also included in the time-of-flight spectra were obtained. Figs. 2.11(a)-(b), show the time-of-flight spectra measured in ADC channels (T) for NE213 and NE230 respectively. Each spectrum includes sharp peaks at high ADC channel numbers (above the neutron peaks) that are associated with gamma events. The most prominent gamma peaks can be seen at channels 2005 (fig. 2.11(a)) and at 2052 (fig 2.11(b)) and are attributed to gammas produced in, or around, the target in the proton beam line. The gammas at 1980 and the humps observed in the spectra in the tail region of the spectra below the neutron peak are attributed to resonances of ^{12}C associated with the 6.5 cm thick graphite block put in front of the collimator side facing the target. A flat, time-independent gamma ray background continuum is also evident in the spectra. The full width at half maximum of the gamma peak (7 ADC channels) provides a measure of the intrinsic time resolution of the detector system.

In order to convert the neutron time of flight data from T scale in ADC channels to a time scale in nanosecond, the time calibration constant (ADC channels per nanosecond) was found as follows: TAC_A was operated with two known delay cables respectively, and the change in the position of the neutron peak in the time of flight spectrum was recorded from which a calibration constant of 8.33 channels/ns was calculated. The average energy of the neutrons in the sharp high-energy peak was estimated as follows: For the 66 MeV incident protons on the 1 mm ^{7}Li-target a energy loss of 0.44 MeV was calculated using ELOSS [Ji84] assuming linear energy loss through the target. The energy of the proton emerging from the target was therefore calculated to be 65.56 MeV. The energy of the proton at the centre of the target was assumed to be halfway between 66 MeV and 65.56 MeV and was estimated to be 65.78 MeV. Using the Q-value for $^{7}Li(p,n)^{7}B$ reaction of –1.644 MeV

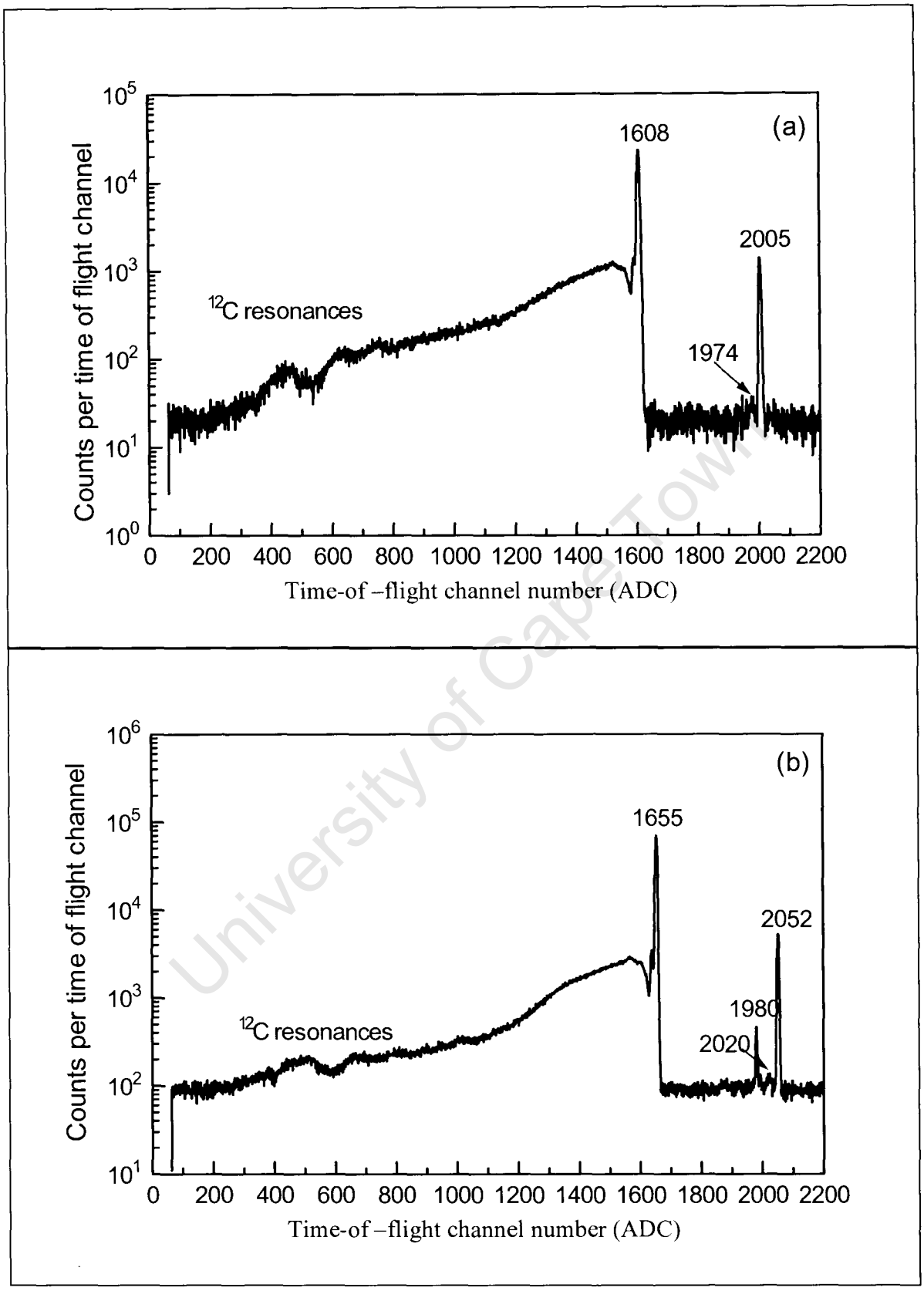

Fig. 2.11(a) *Time-of-flight spectrum measured by NE213 detector for proton and heavier charged particle events and (b) time-of-flight spectrum measured by NE230 detector for deuteron and heavier charged particle events, when exposed to neutrons produced by 66 MeV protons incident on the 1 mm thick Li-target.*

(see table 2.2) the energy of the neutrons at the centre of the neutron peak was estimated to be about 64 MeV using the reaction kinematic equations [Bl55]. The time of flight of 64 MeV neutrons over a flight path of 7.71 m was calculated to be 73.14 ns, using the relativistic relationship

$$E_n = m_o c^2 \left[\frac{1}{\sqrt{1-\left[\frac{d}{tc}\right]^2}} - 1 \right] \tag{2.2}$$

with

$$t = \frac{d}{c\sqrt{1-\left[\frac{m_o c^2}{E_n + m_o c^2}\right]^2}} \tag{2.3}$$

The relationship between the neutron time-of-flight scale T in ADC channels, and the neutron time of flight scale t in nanosecond, is given by

$$t = \frac{T_{\max} - T}{k_{cal}} + t_{\max} \text{ ns} \tag{2.4}$$

Combining equations (2.2) and (2.4) the neutron time-of-flight channels T was calibrated into neutron energy and is given by

$$E_n = m_o c^2 \left[\frac{1}{\sqrt{1-\left[\frac{d}{\left(\frac{T_{\max - T}}{k_{cal}} + t_{\max}\right)c}\right]^2}} - 1 \right] \tag{2.5}$$

where

T: The time-of-flight channel number in ADC.

T_{max}: Position of the most energetic neutrons in ADC

t_{max}: Neutron flight time of the most energetic neutrons in ns (73.14 ns)

k_{cal}: Time calibration constant in channels/second (8.33 channels/ns)

d: Flight path of the neutrons in meters (7.71 m)

m_0: rest mass of the neutron (939.57 MeV/c^2)

c: the speed of light (3×10^8 m.s^{-1})

The time resolution, Δt_γ of the time of flight measurements were determined from the FWHM of the gamma peak in the time of flight spectra, produced by proton-induced reactions in the targets. The time resolution at FWHM of the gamma peak was measured as 0.84 ns. The energy resolution, ΔE_n of the time of flight measurements depends on the time resolution and the uncertainty in the flight path, Δd of the neutrons. In the limit $\frac{\Delta t_\gamma}{t} \rangle\rangle \frac{\Delta d}{d}$ the energy resolution, ΔE_n is given by

$$\Delta E_n = \left[\left(1+\frac{E_n}{m_o c^2}\right)\left(2+\frac{E_n}{m_o c^2}\right)E_n\right]\frac{\Delta t_\gamma}{t} \qquad (2.6)$$

This implies an energy resolution of 0.06 MeV at 5.36 MeV and 1.62 MeV at 64 MeV. Fig. 2.12 shows energy resolution ΔE_n as a function of neutron energy E_n for neutron energies between 5 to 64 MeV.

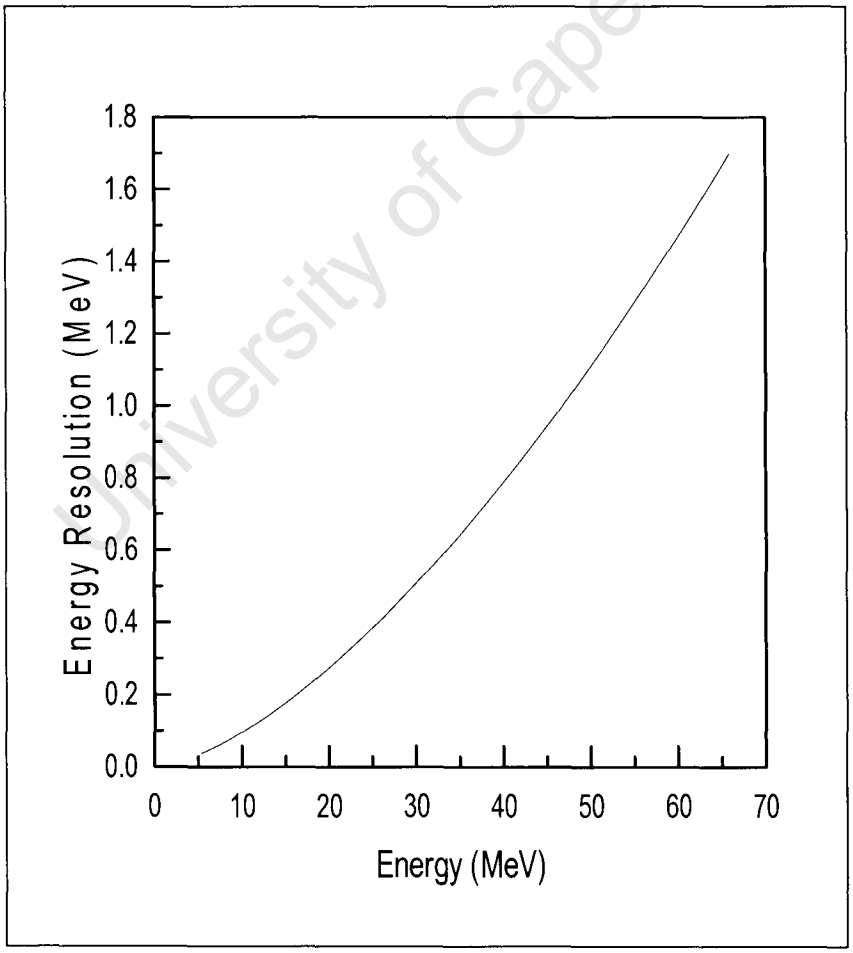

Fig. 2.12 *Energy resolution as a function of the neutron energy between 5 MeV and 64 MeV.*

2.6.3 Example of obtaining a response function at a specific neutron energy

Figs. 2.13 and 2.14 show perspective plots of counts (vertical) versus L (charged particle energy) and T (incident neutron energy) for the selected events detected by the NE213 and NE230 detectors in-air when exposed to neutrons from 66 MeV protons incident on the 1 mm thick Li-target. The main features for the selected proton and heavier charged particle events detected by NE213 shown in LT-plot (fig. 2.13) are the curved ridge on the left marking the upper pulse height L, limit for recoiling protons from n-p elastic scattering events. The maximum proton energy associated with the n-p ridge edge is equal to the incident neutron energy. The ridges more to the right are due to protons events from n-C reactions. The second ridge at lower pulse height is associated with the maximum pulse height for proton recoils from n-C reactions. The strong ridge at the far right corresponds mainly to the intense forward peak of 64 MeV neutrons from the ^{7}Li(p,n)^{7}B reaction. It can be seen in the plot that at low L values, i.e. low neutron energy, the ridges from n-p and n-C are more distinguishable than at high L values; this is due to an increase in proton escapes from the detector with increasing neutron energy.

The main features for the selected deuteron and heavier charged particle events detected by NE230 shown in LT-plot (fig. 2.14) are the curved ridge on the left marking the upper pulse height, L, limit for forward deuteron recoils from n-d elastic scattering events and the ridges more to the right are due to the deuteron and heavier charged particle events from n-C reactions. The maximum deuteron energy associated with the n-d ridge edge are equal to eight-ninths the incident neutron energy. As in the case with the NE213 detector the ridges from n-d and n-C are less distinguishable at high L values due to increase in deuteron escapes from the detector with increasing neutron energy. The strong ridge due to the intense forward peak of 64 MeV neutrons from the ^{7}Li(p,n)^{7}B reaction is also seen in this plot.

Figs. 2.13 and 2.14 also show an example of a time window setting on the T-axis used to select neutrons of energy $E = 39\ MeV$. The projection of the events in the time window on the LT-plane onto the L-axis gives the detector response function to neutrons of energy 39 MeV. Figs. 2.15(a)-(b) show the response functions at E = 39 MeV for the NE213 detector (fig. 2.15(a)) and NE230 detector (fig. 2.15(b)) obtained in this way. The two edges defining the upper pulse height limits for n-C

reactions, n-p (fig. 2.15(a)) and n-d (fig. 2.15(b)) elastic scattering are clearly identifiable in the figures and are well-defined functions of neutron energy. The NE230 response matrix was determined in this way for all the energies of interest.

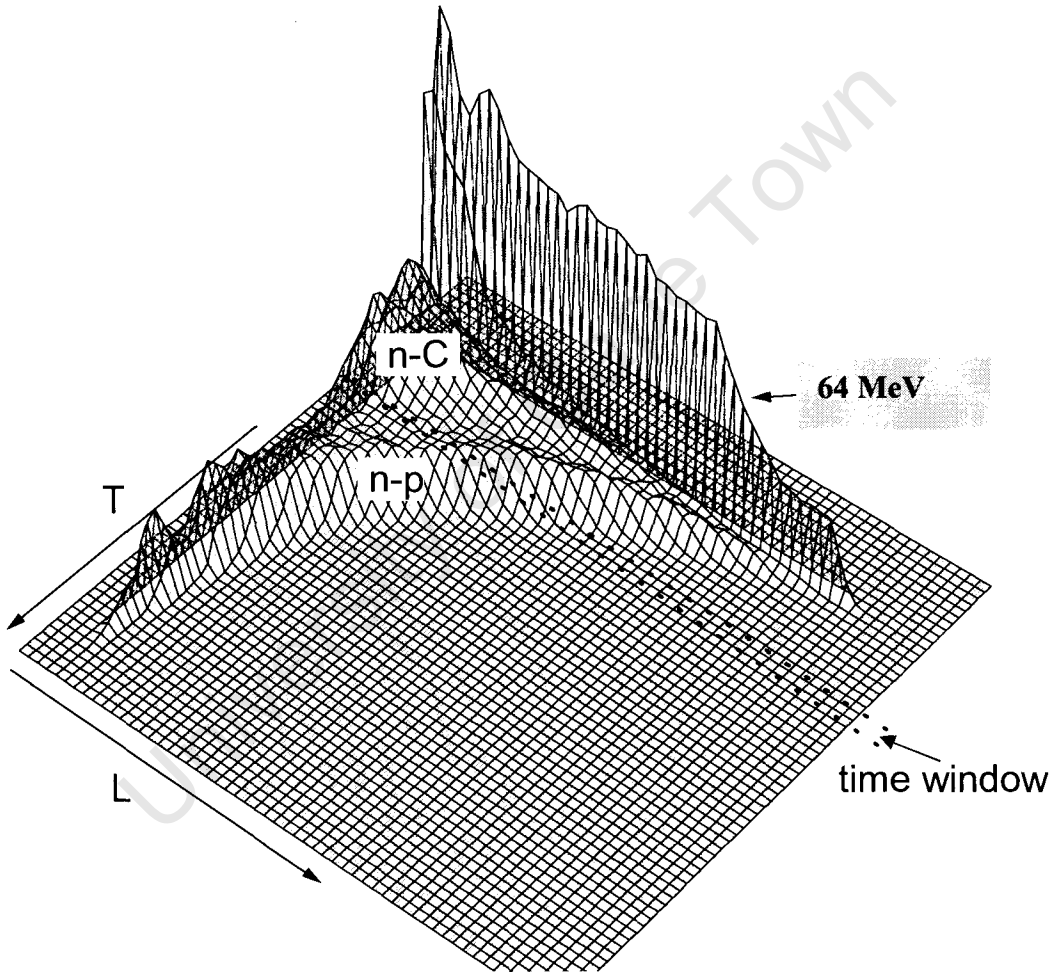

Fig. 2.13 *Perspective views of counts (vertical) as a function of pulse height, L, and time-of-flight, T, for the proton and heavier charged particle events detected by NE213 when exposed to neutrons produced by 66 MeV protons incident on the 1 mm thick Li-target. The dashed lines in the plots indicate the time window used to select neutrons of 39 MeV*

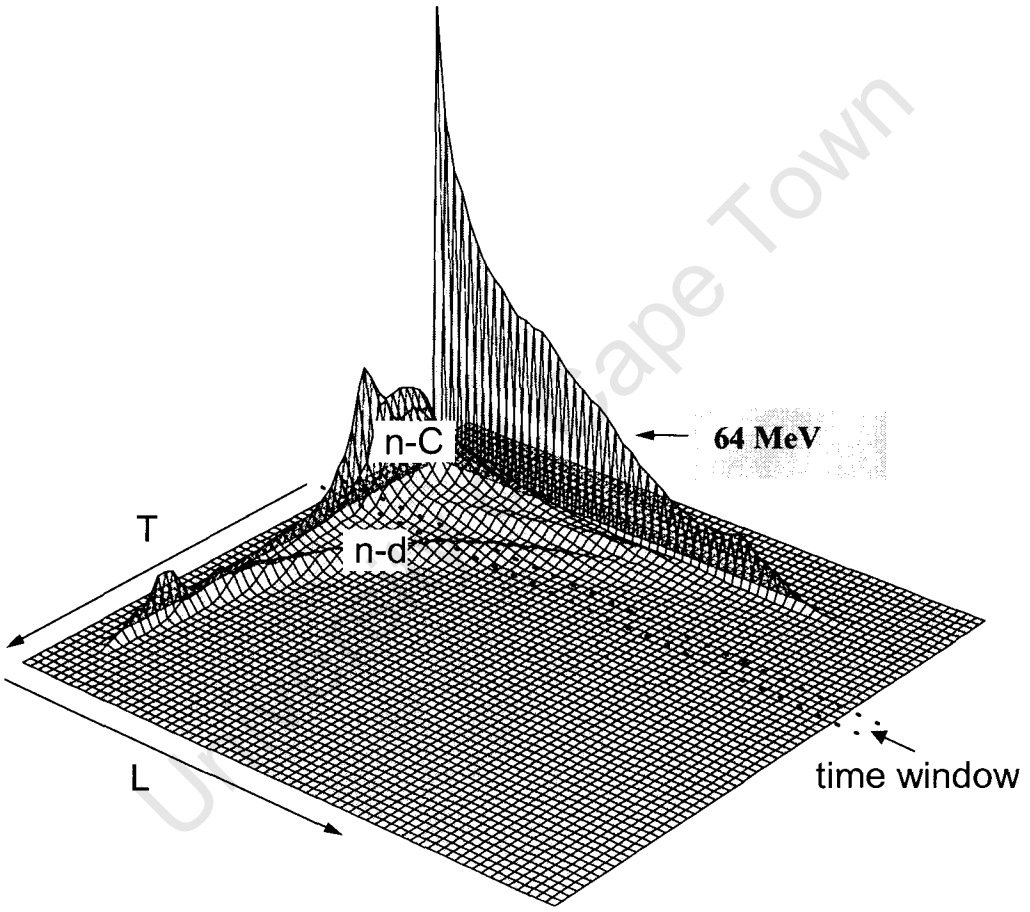

Fig. 2.14: *Perspective views of counts (vertical) as a function of pulse height, L, and time-of-flight, T, for the deuteron and heavier charged particle events detected by NE230 when exposed to neutrons produced by 66 MeV protons incident on the 1 mm thick Li-target. The dashed lines in the plots indicate the time window used to select neutrons of 39 MeV.*

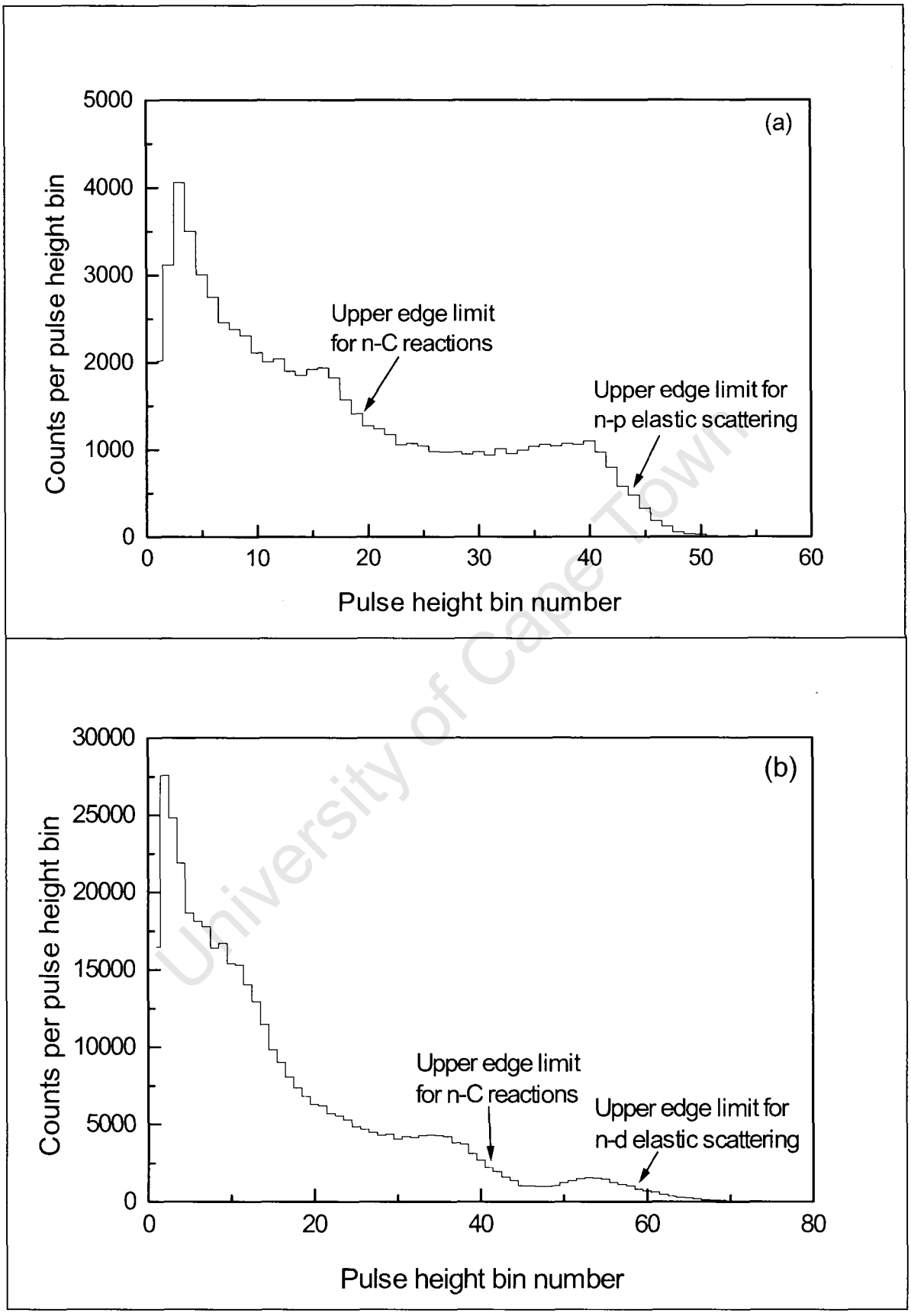

Fig. 2.15 (a) *Response functions measured by the NE213 and (b) theNE230 detectors, when exposed to 39 MeV neutrons. The upper edges of these response functions are well-defined functions of neutron energy.*

2.6.4 Neutron detection efficiency

The NE230 neutron detection efficiency $\varepsilon_D(E_n, L_D)$ as a function of neutron energy E_n above a pulse height threshold L_D was determined by experiment using an NE213 detector for which the n-p elastic scattering cross-section was known. Appendix A contains a detailed description of how the efficiency was determined. The final results are plotted in fig. 2.16 that shows the neutron detection efficiency for the NE230 detector as a function of neutron energy for L_D corresponding to a neutron energy threshold of 5 MeV (used in the off-line analysis as noted in Appendix A). From the plot it can be seen that the efficiency decreases sharply from a maximum just above the low energy threshold to a minimum at about 20 MeV. The efficiency then rises to a maximum at about 25 MeV and then decreases with increasing neutron energy. The trend of the curve is explained by the fact that at energies below 20 MeV the contribution of efficiency is mainly from n-d elastic scattering while above 20 MeV the contribution to the efficiency from n-C reactions increase with increasing neutron energy.

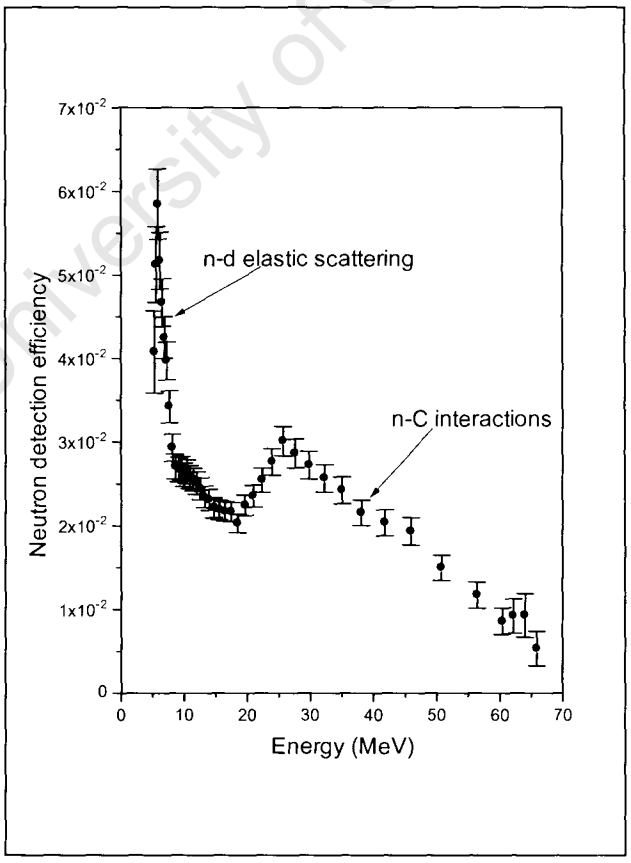

Fig. 2.16 *Neutron detection efficiency for the NE230 detector as a function of neutron energy for a detection energy threshold 5 MeV. (See Appendix A for details).*

2.7 In-phantom measurements

A series of measurements was carried out using a water phantom with dimensions 600 mm x 600 mm x 600 mm using neutrons produced by the 1 mm thick Li-target. The phantom was mounted with its centre orientated along the 0°- neutron beam at a distance of 7.53 m (to the front face of tank) from the Li target. The NE230 detector assembly was mounted in the water phantom at 60° to the horizontal (with the detector axis aligned perpendicular to the 0°- neutron beam as for the in air-measurements) and connected to a remote control system as shown in fig 2.17. The orientation of the detector was dictated by the need to keep the expansion chamber of the NE230 cylindrical cell upright. Measurements were made at positions along and off the beam axis at positions shown in fig. 2.18 indicated in coordinate form *(d, r)*, where *d* is depth in cm along beam axis and *r* is the lateral distance in cm from the beam axis. The diameter of the beam as it entered the phantom was 2.5 cm (due to the collimation) while at a depth of 20 cm it was measured to be about 5.0 cm in diameter (section 2.2). The shaded region indicates the cone defined by these measurements. A more detailed profile of the beam flux based on Monte Carlo calculations is discussed in section 4.3.2.

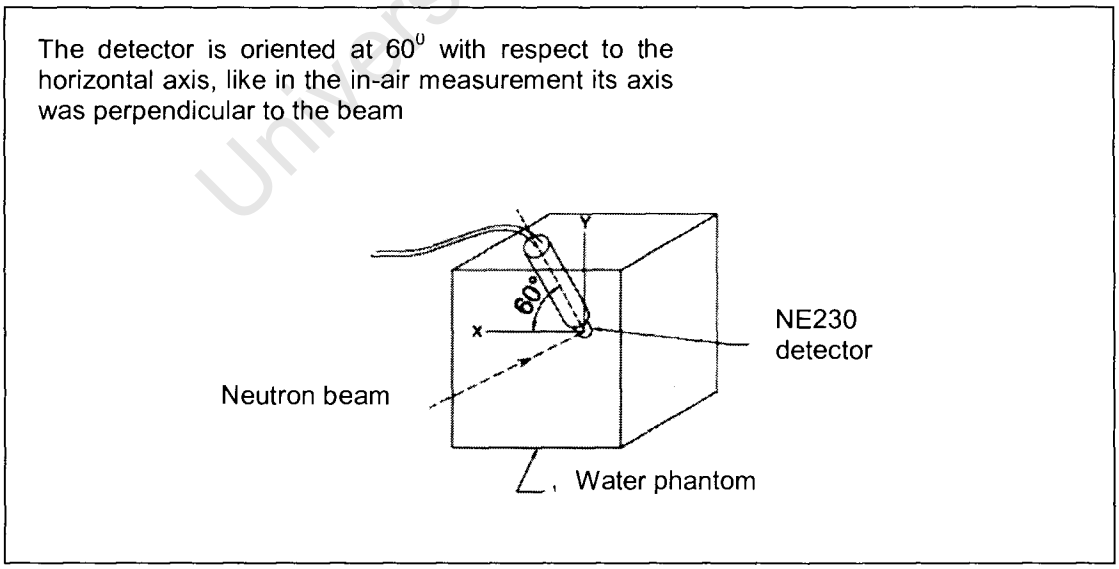

Fig. 2.17 *Schematic diagram of the detector immersed in the water phantom*

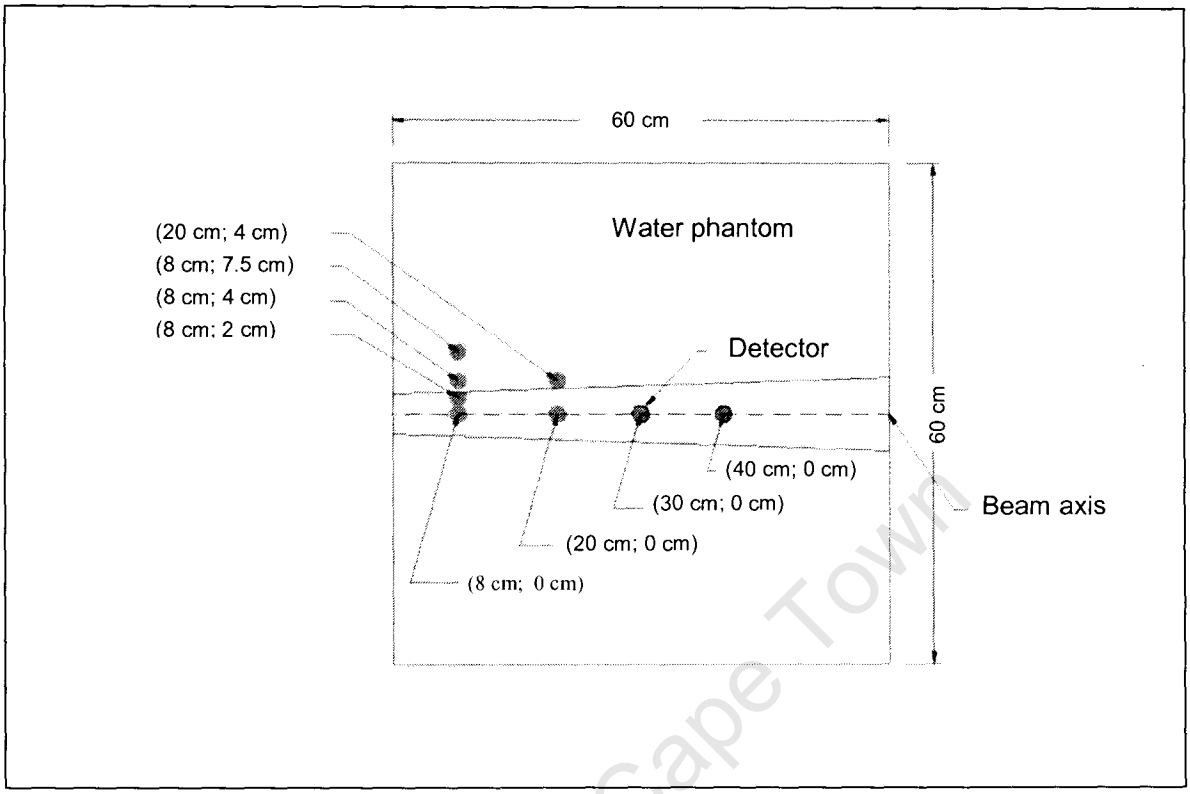

Fig. 2.18: *Schematic diagram showing the different positions in the phantom where measurements were made. The shaded region indicates the straight line geometrical path of the beam (see text).*

Although the same parameters *T, L, F* and *D* were recorded as for the in-air measurements *T* was not analysed as the time-of-flight for a neutron that is detected in water is not well-defined. As described in detail in section 2.5 events associated with deuterons and heavier charged particles were selected by applying appropriate cuts to the data in the *LS* plane. The resulting pulse height spectra, obtained by projecting the selected events onto the *L*-axis, are shown in figs. 2.19(a)-(c). The spectra are normalized to the same number of neutrons measured by the neutron monitor.

Fig. 2.19(a) shows spectra measured at different depths along the beam axis into the phantom. The spectral shapes resemble the shape of the in-air spectrum and the upper edge associated with the 64 MeV neutron peak is clearly visible in all five cases. However, as the depth increases it can be seen that the beams are attenuated and that the proportion of high energy neutrons to low energy neutrons increases. (This is often referred to as "hardening' of the spectrum).

Fig. 2.19(b) shows the results of runs for measurements at positions off the beam axis at a depth 8 cm into the phantom. The spectrum measured at position (8 cm, 2 cm) has a similar shape to the in-air spectrum and the upper edge associated with the 64 MeV neutron peak is visible in the spectrum. However, at positions (8 cm, 4 cm) and (8 cm, 7.5 cm) the shapes of the spectra no longer resemble the in-air spectrum and the upper edges of the spectra associated with the 64 MeV neutron peak are no longer present. At all three off-axis positions the beam has also "softened", i.e. the proportion of low energy neutrons to high energy neutrons has increased and that the softening increases with increasing lateral distance. Fig. 2.19(c) shows spectra measured at depths 8 cm and 20 cm at a lateral distance 4 cm from the beam axis in the phantom. The spectrum at position (20 cm, 4 cm) shows the edge associated with the 64 MeV neutron peak while the peak is absent in the (8 cm, 4 cm).

The effects that are observed are attributed to the fact that neutrons that enter the detector at these positions have first undergone scattering. Due to the kinematics involved the scattering angle of these scattered neutrons increases as their energy decreases, thus explaining why the spectrum at (20 cm, 4 cm) shows the edge associated with the 64 MeV neutron peak since it is at a more forward angle than the other two positions.

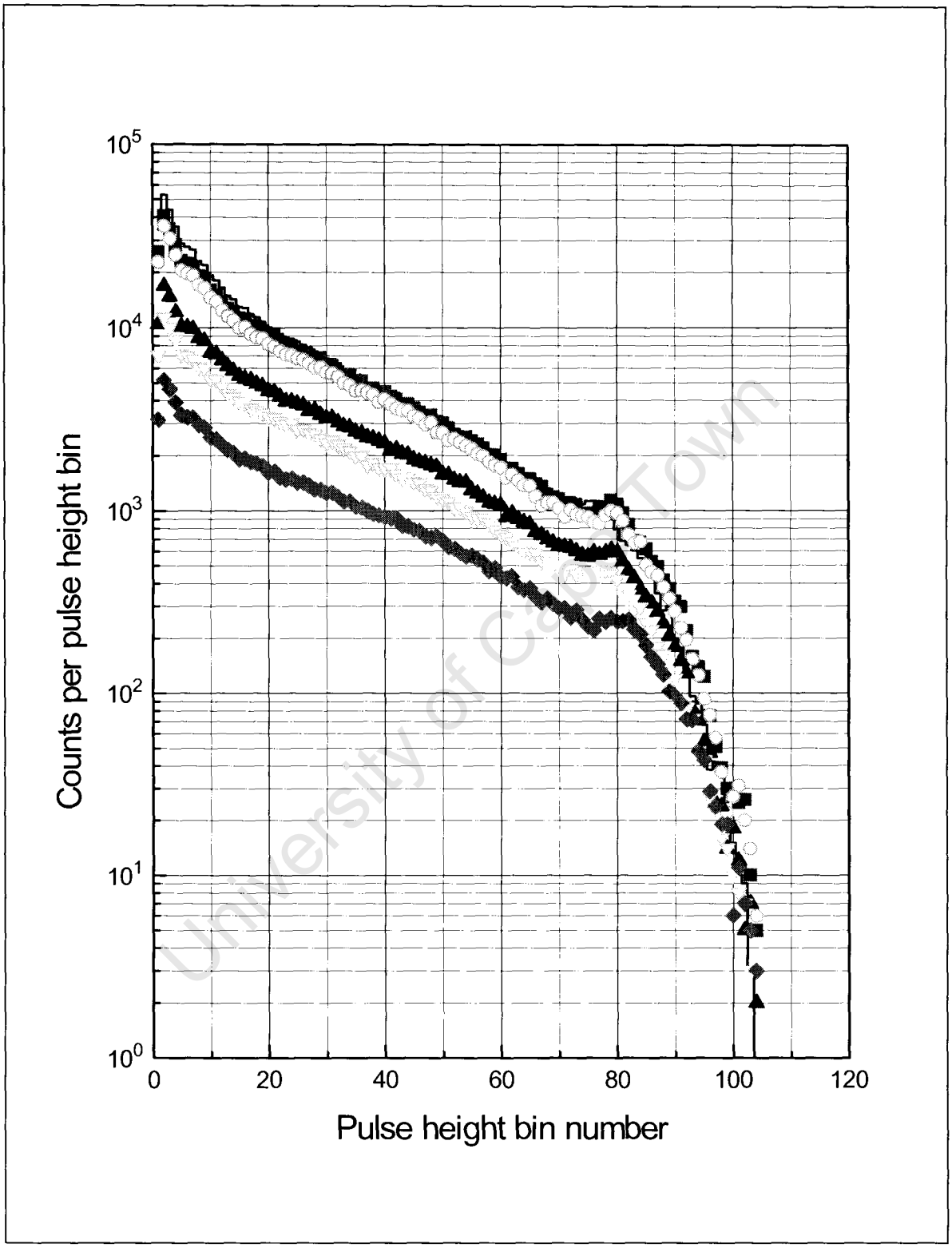

Fig. 2.19(a) *Comparisons of pulse height spectra measured in-air (histogram) and at positions (6 cm, 0 cm) (solid squares); (8 cm, 0 cm) (open circles); (20 cm, 0 cm) (solid up triangles); (30 cm, 0 cm) (open down triangles) and (40 cm, 0 cm) (solid diamond) along the beam axis in the phantom.*

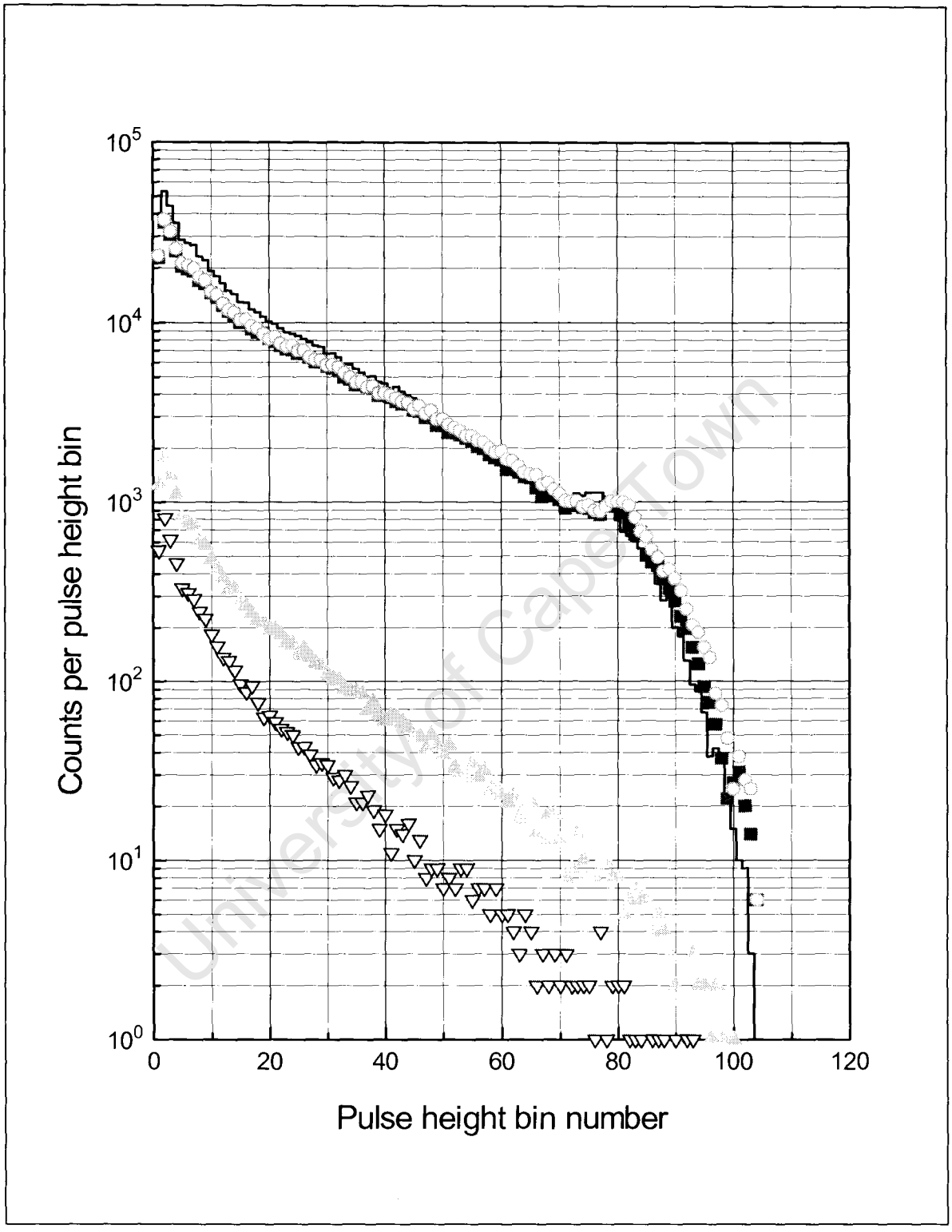

Fig. 2.19(b) *Comparisons of pulse height spectra measured in-air (histogram) and at positions (8 cm, 0 cm) (solid squares); (8 cm, 2 cm) (open circles); (8 cm, 4cm) (solid up triangles) and (8 cm, 7.5 cm) (open down triangles) off the beam axis at a depth 8 cm in the phantom.*

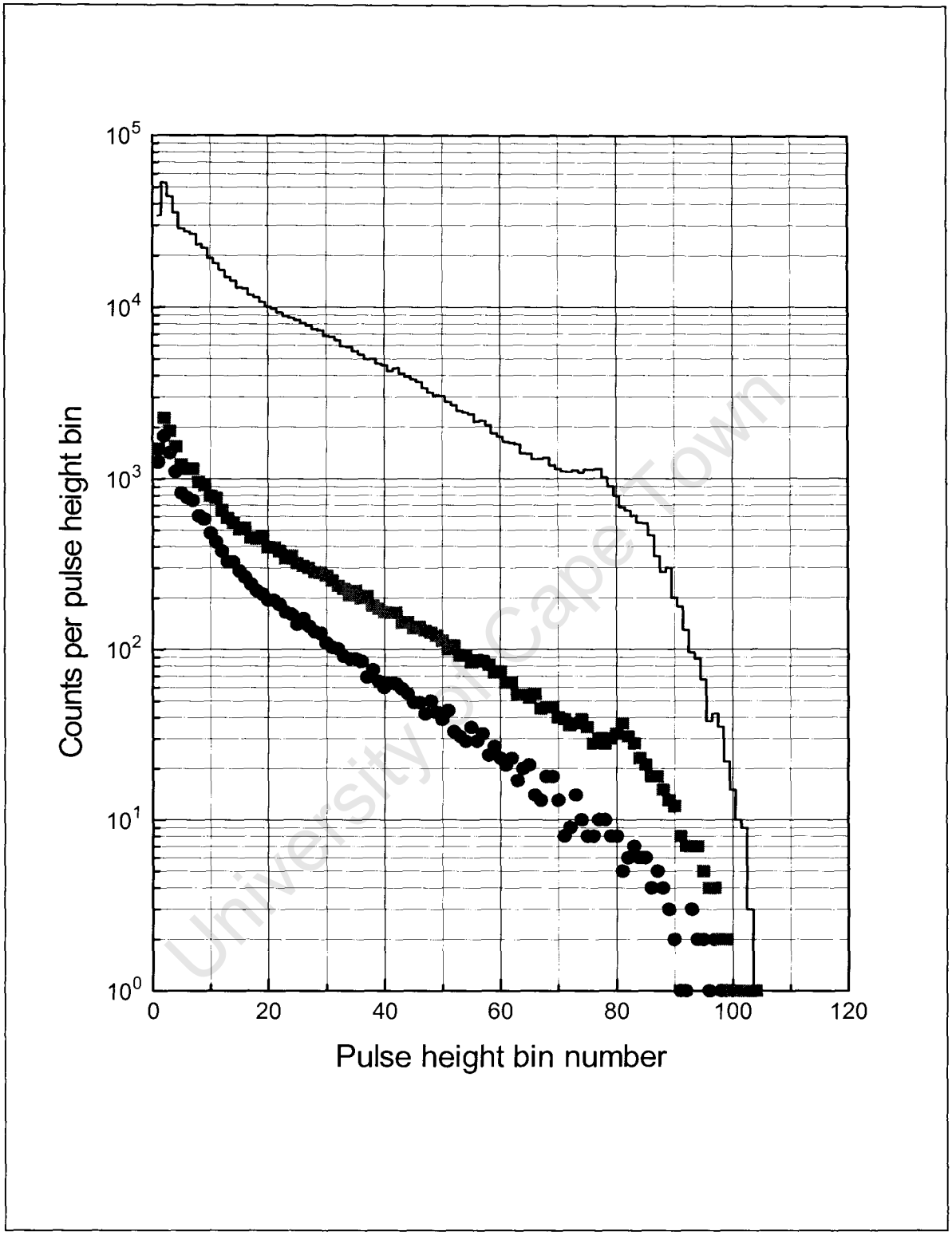

Fig. 2.19(c) *Comparisons of pulse height spectra measured in-air (histogram) and at positions (8 cm, 4 cm) (solid circles) and (20 cm, 4 cm) (solid square) off the beam axis in the phantom.*

CHAPTER 3

NEUTRON ENERGY SPECTRA

3.1 Unfolding of pulse height spectra

The neutron energy spectrum $N(E)$ and the measured pulse height spectrum $L(E)$ are related as follows:

$$L(E) = \int_0^{\alpha} R(E,E')N(E')\,dE' \tag{3.1}$$

where $R(E,E')$ is the response function of the detector. The response function represents the probability that a neutron of energy E' will deposit an amount of scintillation light of energy E in the detector. When the response function of the detector is known at discrete energies E_k , the discrete form of equation 3.1 can be written as

$$L_k = \sum_{i=1}^{n} R_{ki} a_i \quad \text{for} \quad k = 1 \text{ to } m \tag{3.2}$$

Where, L_k is the number of counts (amount of scintillation light) in the k th pulse height bin of the measured pulse height spectrum $L(E_k)$, R_{ki} is the response matrix relating the counts in the k th pulse height bin to neutrons in the i th energy bin, and a_i is the average number of neutrons in the i th energy bin of the neutron energy spectrum $N(E_i)$. Equation 3.2 can be solved in a number of different ways to obtain the neutron energy spectrum $N(E)$ from the measured pulse height spectrum $L(E)$, provided that the response matrix is known over the whole energy range.

The response matrix can be determined either by calculation, usually via Monte Carlo simulation, or by measurement. Monte Carlo codes that are used include Stanton [St71], O5S [Mc75], SCINFUL [Di88], and MCNPX [Wa02]. However, the simulations not suitable because the nuclear data tables used contain only emission spectra and do not preserve the correlation of several particles resulting from a single neutron interaction, while the nuclear models are to schematic to predict the

correlations correctly at the energies consider in this work. In the present work where organic liquid scintillators were used, the cross-sections for n-C reactions play a important role but these cross-sections are not well known above about 20 MeV [Br02b] and for the reasons mentioned above the in-air measurements described in section 2.6 were carried out.

A comparison of the various ways in which unfolding can be accomplished is presented by Reginato [Re06]. A brief summary of some of the methods is provided in Appendix B. Based on the arguments presented in [Re06] as well as the availability and support of the code the Bayesian unfolding code MAXED was used. The MAXED unfolding code was developed for the unfolding of Bonner sphere neutron spectrometer data, but was modified for the unfolding of multi-channel data, such as recoil spectrometer data [Re99, Re02]. In the present work measured pulse height spectra were unfolded into neutron energy spectra by MAXED using a response matrix that was determined experimentally as described below (Appendix B also contains brief details of the input required by MAXED).

3.2 Determination of the response matrix for the NE230 detector

Equation 3.2 was solved for 43 neutron energies using the time-of-flight data measured with the NE230 neutron detector in-air as described in section 2.6. The 43 neutron energies were chosen to produce a response matrix with energy resolution that could resolve the structure attributed to resonances of ^{12}C associated with the 6.5 cm thick graphite block put in front of the collimator side facing the target and the intense forward peak of 64 MeV neutrons from the $^{7}Li(p,n)^{7}Be$ reaction, in the energy spectrum of the Li-target measured in-air. The response matrix of the NE230 detector to these energies was obtained in the form of a set of response functions (pulse height spectra), where each response function in the set is a measure of the response of the detector to each of the 43 neutron energies. After applying the *LS*-cut to select deuteron and heavier charged particle events as described in section 2.5, the response functions were determined from the combined two-parameter (*LT*) data obtained using the Li, Be and C target. As detailed in Table 3.1, the time range was divided into 3 regions of different time resolution with each region further subdivided into a

Table 3.1 *Results of calibration of time windows into energy bins*

Bin Number *J*	Time window (ADC channel)		Centre of energy bin (MeV)	Energy bin widths (MeV)	Energy bin parameters (MeV)	
	Lower	Upper			Lower	Upper
1	227	275	5.36	0.26	5.23	5.49
2	275	323	5.63	0.28	5.49	5.77
3	323	371	5.92	0.30	5.77	6.07
4	371	419	6.23	0.32	6.07	6.39
5	419	467	6.56	0.35	6.39	6.74
6	467	515	6.93	0.38	6.74	7.12
7	515	563	7.32	0.41	7.12	7.53
8	563	611	7.75	0.45	7.53	7.98
9	611	659	8.22	0.49	7.98	8.47
10	659	707	8.65	0.54	8.47	9.01
11	707	739	9.20	0.39	9.01	9.40
12	739	771	9.60	0.41	9.40	9.81
13	771	803	10.03	0.44	9.81	10.25
14	803	835	10.49	0.48	10.25	10.73
15	835	867	10.97	0.50	10.73	11.23
16	867	899	11.50	0.54	11.23	11.77
17	899	931	12.06	0.59	11.77	12.36
18	931	963	12.67	0.63	12.36	12.99
19	963	995	13.32	0.67	12.99	13.66
20	995	1027	14.02	0.73	13.66	14.39
21	1027	1059	14.78	0.80	14.39	15.19
22	1059	1091	15.61	0.86	15.19	16.05
23	1091	1123	16.51	0.94	16.05	16.99
24	1123	1155	17.49	1.02	16.99	18.01
25	1155	1187	18.56	1.12	18.01	19.13
26	1187	1219	19.73	1.23	19.13	20.36
27	1219	1251	21.02	1.35	20.36	21.71
28	1251	1283	22.43	1.49	21.71	23.20
29	1283	1315	24.00	1.65	23.20	24.85
30	1315	1347	25.75	1.84	24.85	26.69
31	1347	1379	27.69	2.06	26.69	28.75
32	1379	1411	29.87	2.30	28.75	31.05
33	1411	1443	32.31	2.60	31.05	33.65
34	1443	1475	35.08	2.95	33.65	36.60
35	1475	1507	38.23	3.36	36.60	39.96
36	1507	1539	41.83	3.86	39.96	43.82
37	1539	1571	45.97	4.47	43.82	48.29
38	1571	1603	50.78	5.20	48.29	53.49
39	1603	1635	56.42	6.11	53.49	59.60
40	1635	1643	60.44	1.70	59.60	61.30
41	1643	1651	62.18	1.78	61.30	63.08
42	1651	1659	63.99	1.85	63.08	64.93
43	1659	1667	65.89	1.94	64.93	66.87

number of equal time widths. Thus, the first region was divided into 10 time windows, the second region into 29 time windows and the third time region into 4 time windows. Fig. 3.1 shows a perspective plot of counts (vertical) as a function of pulse height L and neutron time of flight T, for the time of flight data measured with the NE230. The 3 time regions used to select the 43 neutron energies are also labelled in the plot. Each time window corresponds to a neutron energy bin of different energy and energy width. Time windows centres (in ADC channels) were converted to neutron energy bins, using equation (2.4).

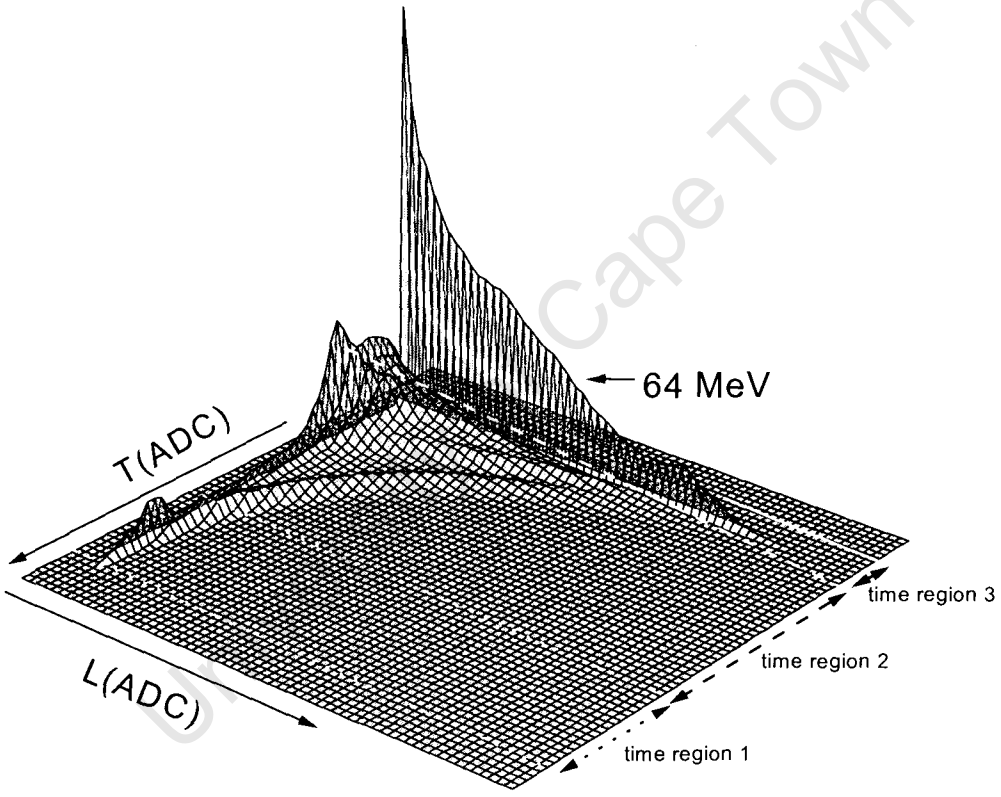

Fig. 3.1 *Counts as a function of pulse height, L, and time-of-flight, T, for the data obtained using the Li-target. The 3 different time regions referred to in the text are indicated.*

The events within each time window (energy bin) in the LT-plane were projected onto the L-axis as described in section 2.6.3. Forty-three response functions were obtained, each of k = 1 to 104 pulse height bins. Each pulse height spectrum was normalized to 50000 integral counts. The response functions were then combined to form a response matrix of dimensions 43(E)x104(L).

The forty-three response functions (pulse height spectra) comprising the response matrix are shown in figs. 3.2(a)-(g). Using $j = 25$ as an example, the peak labelled D_f is attributed to forward recoiling deuterons from n-d elastic scattering and is clearly distinguishable from deuterons or alpha particles from $^{12}C(n,d)$ and $^{12}C(n,\alpha)$ reactions, labelled D_r and α_1, respectively. For the first six low energy response functions (j = 1 - 6) only the upper edge of the D_f peak is seen, since the lower edge is below the energy threshold of 5.0 MeV that was set for the measurements. In general, the response functions show that as the neutron energy increases the upper edge of D_f shifts towards higher pulse heights as expected. However, for the highest range of response functions, for example, from about $j = 37$ upward the peak becomes difficult to identify.

The peak due to deuterons from the $^{12}C(n,d)^{11}B$ reaction D_r is visible in the higher energy response functions from about $j = 25$ upward. As the neutron energy increases the peak shifts towards D_f until they overlap as can be seen in the response functions j = 38 - 43. This is attributed to a kinematic effect caused by the larger increase in the energy of the outgoing deuterons from the $^{12}C(n,d)^{11}B$ reaction compared with the relatively smaller increase in the energy of the forward recoil deuterons as the neutron energy increases. It can also be seen that the peaks D_f and D_r diminish with increasing neutron energy. This is due to the fact that the deuteron range increases as the neutron energy increases leading to an increase in escaping deuterons with increasing neutron energy. The deuteron range in NE230 is 0.066 cm, 0.465 cm and 1.170 cm for 10 MeV, 30 MeV and 50 MeV deuterons, respectively. For the detector in question, this implies that about 3%, 23% and 57% of the deuterons will escape, respectively. The "escape effect" was corrected for in the calculation of the neutron detection efficiency of the NE213 detector as a function of neutron energy, as detailed in appendix A. A correction for deuteron escape events in the NE230 was not necessary.

The contribution of the alpha particles to the response functions comes about mainly due to the ground state transition of the $^{12}C(n,\alpha)^{9}Be$ reaction and the $^{12}C(n,n')3\alpha$ reaction. The peak due to alpha particles from the $^{12}C(n,\alpha)^{9}Be$ reaction is clearly visible in the response functions j = 15-34. As the neutron energy increases the contribution due to alphas from the $^{12}C(n,n')3\alpha$ reaction become more dominant.

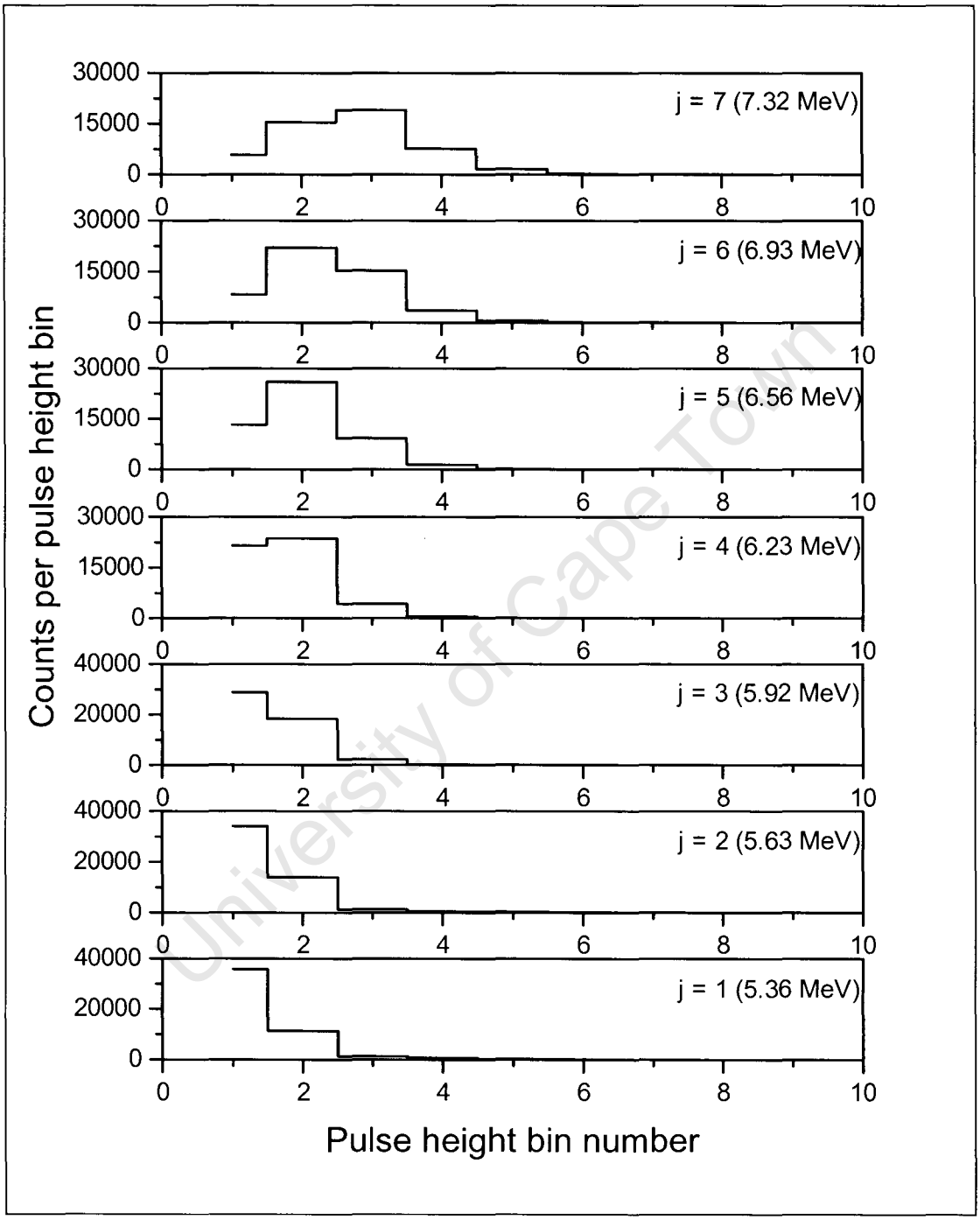

Fig. 3.2(a) *Response functions, (j = 1 to 7) of the NE230 detector when exposed to neutrons of energy indicated.*

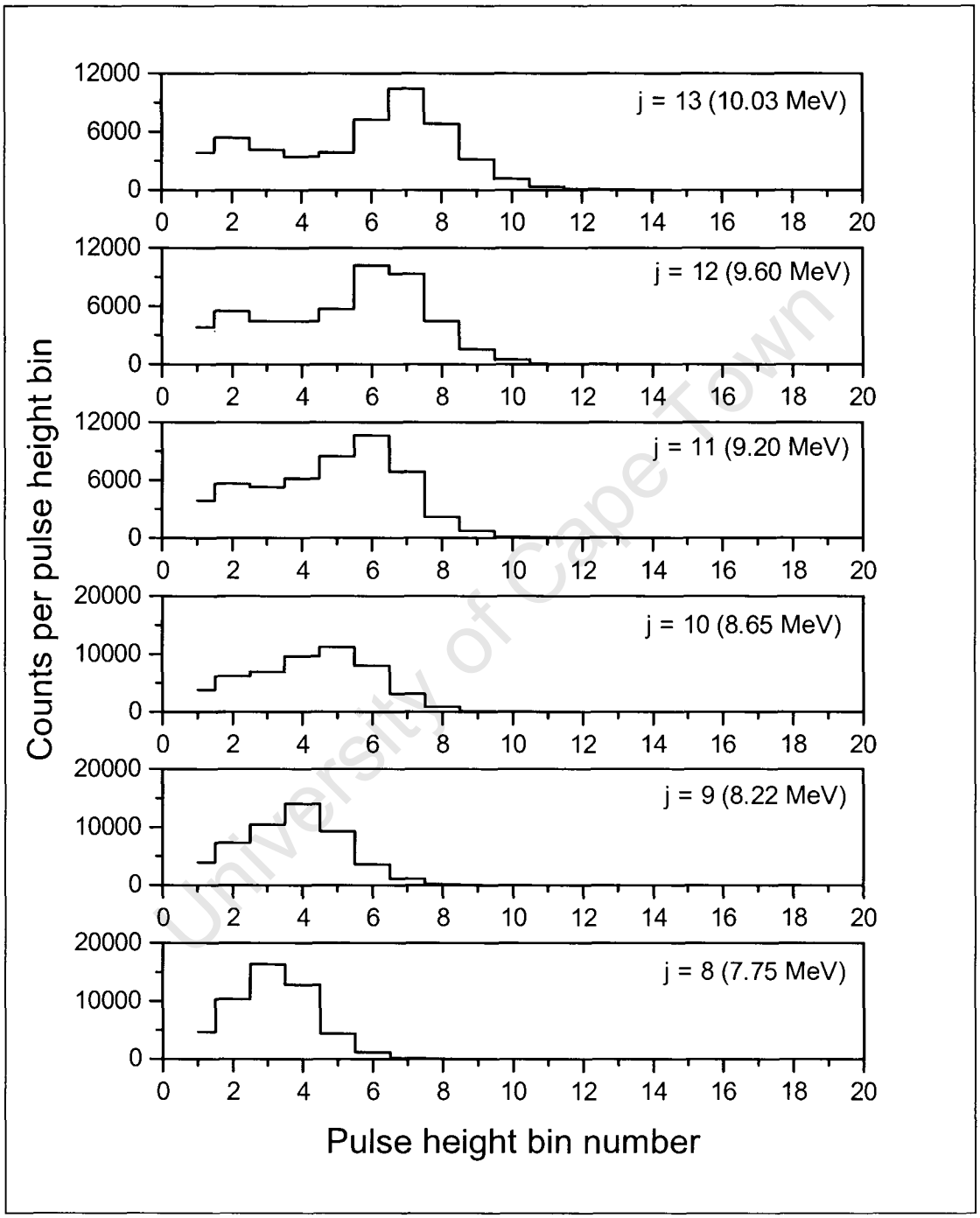

Fig. 3.2(b) *Response functions,(j = 8 to 13) of the NE230 detector when exposed to neutrons of energy indicated.*

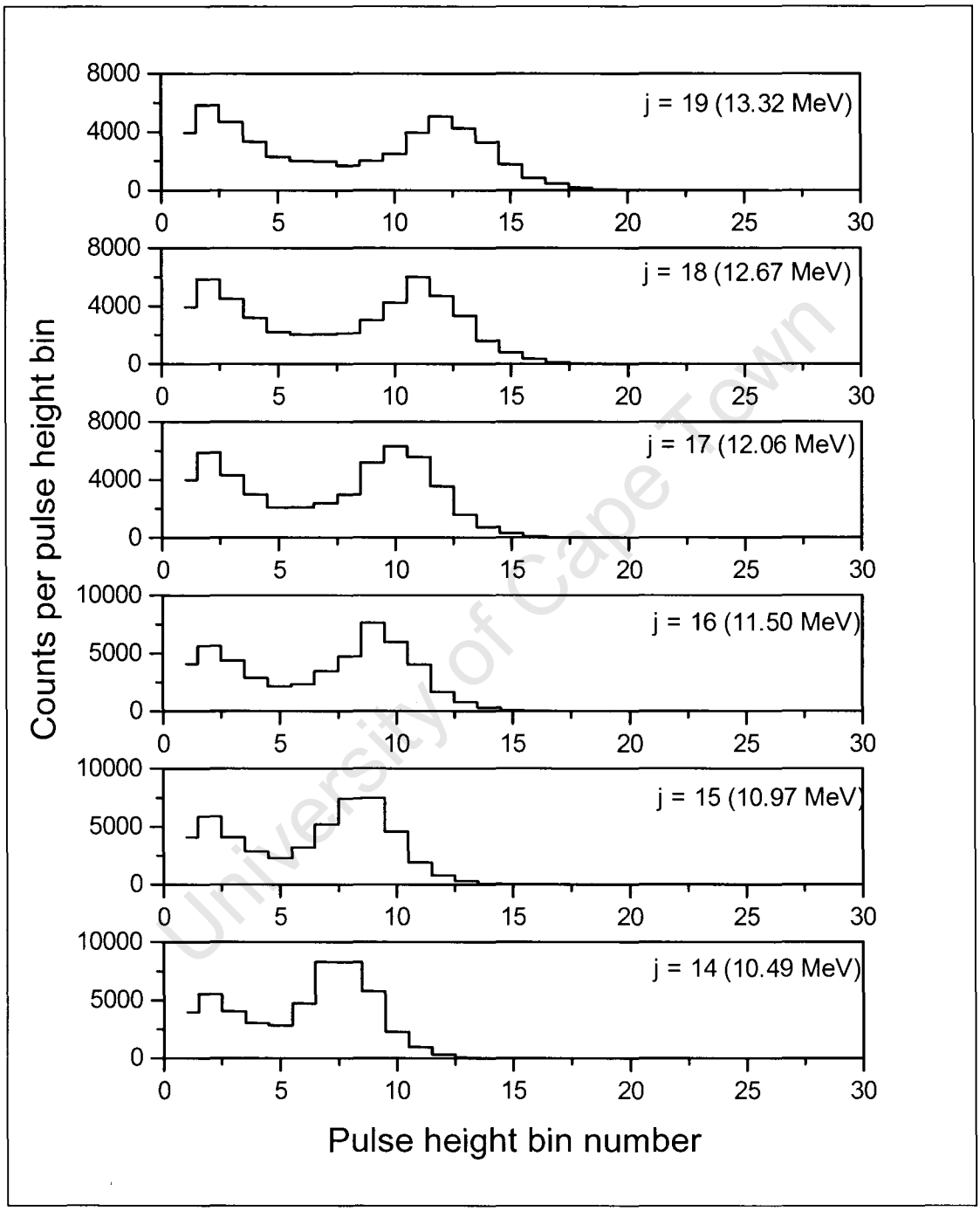

Fig. 3.2(c) *Response functions,(j = 14 to 19) of the NE230 detector when exposed to neutrons of energy indicated.*

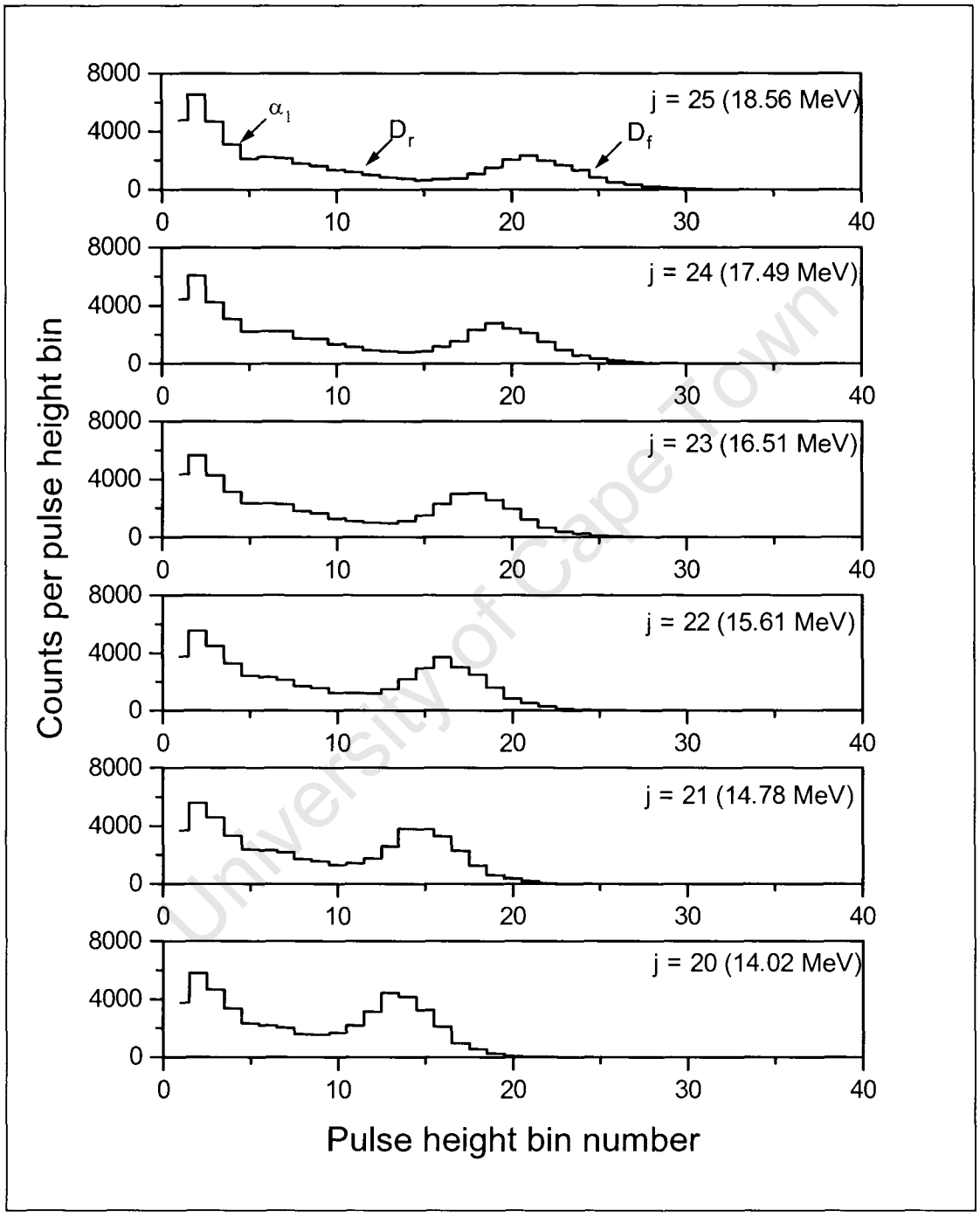

Fig. 3.2(d) *Response functions,(j = 20 to 25) of the NE230 detector when exposed to neutrons of energy indicated.*

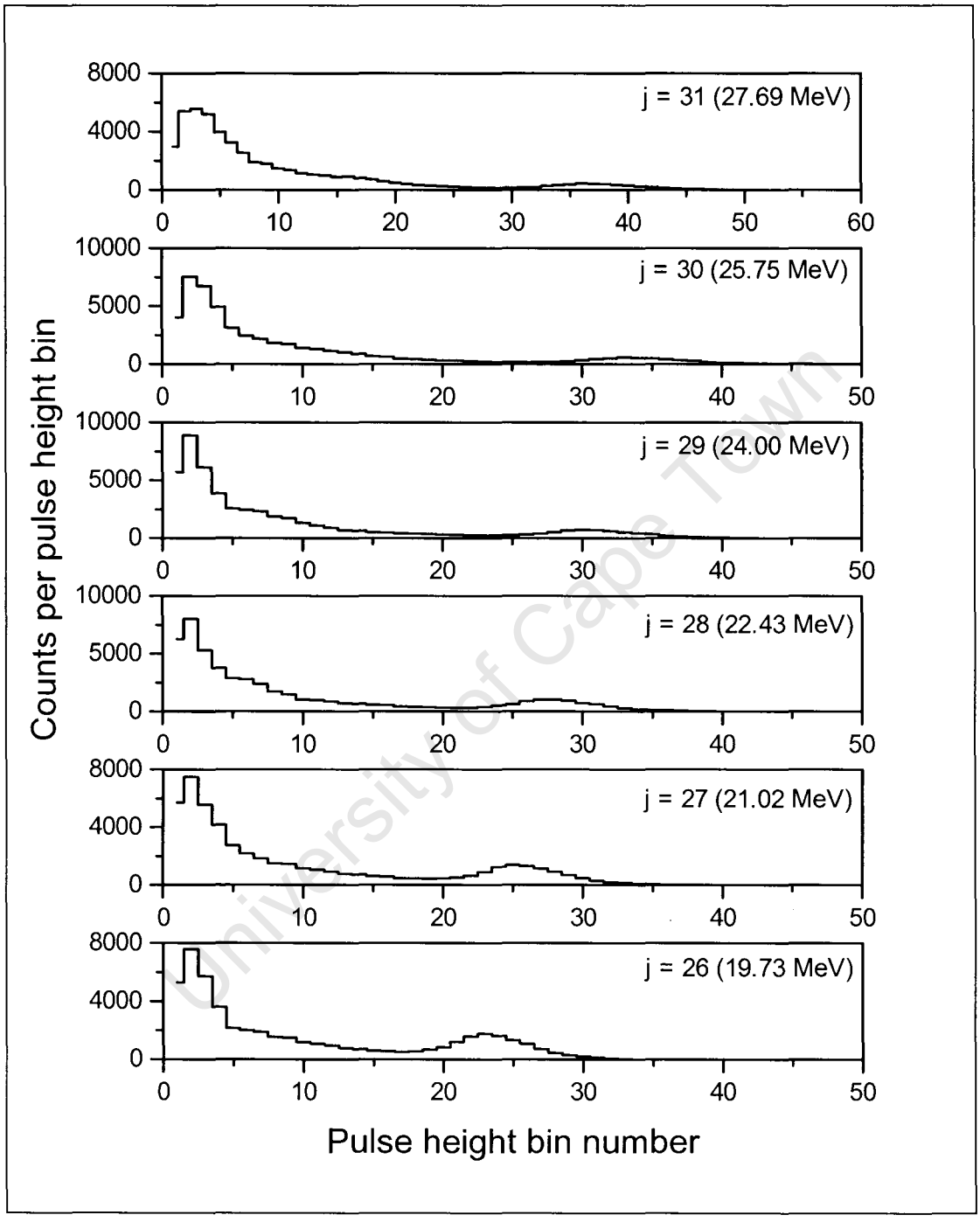

Fig. 3.2(e) *Response functions,(j = 26 to 31) of the NE230 detector when exposed to neutrons of energy indicated.*

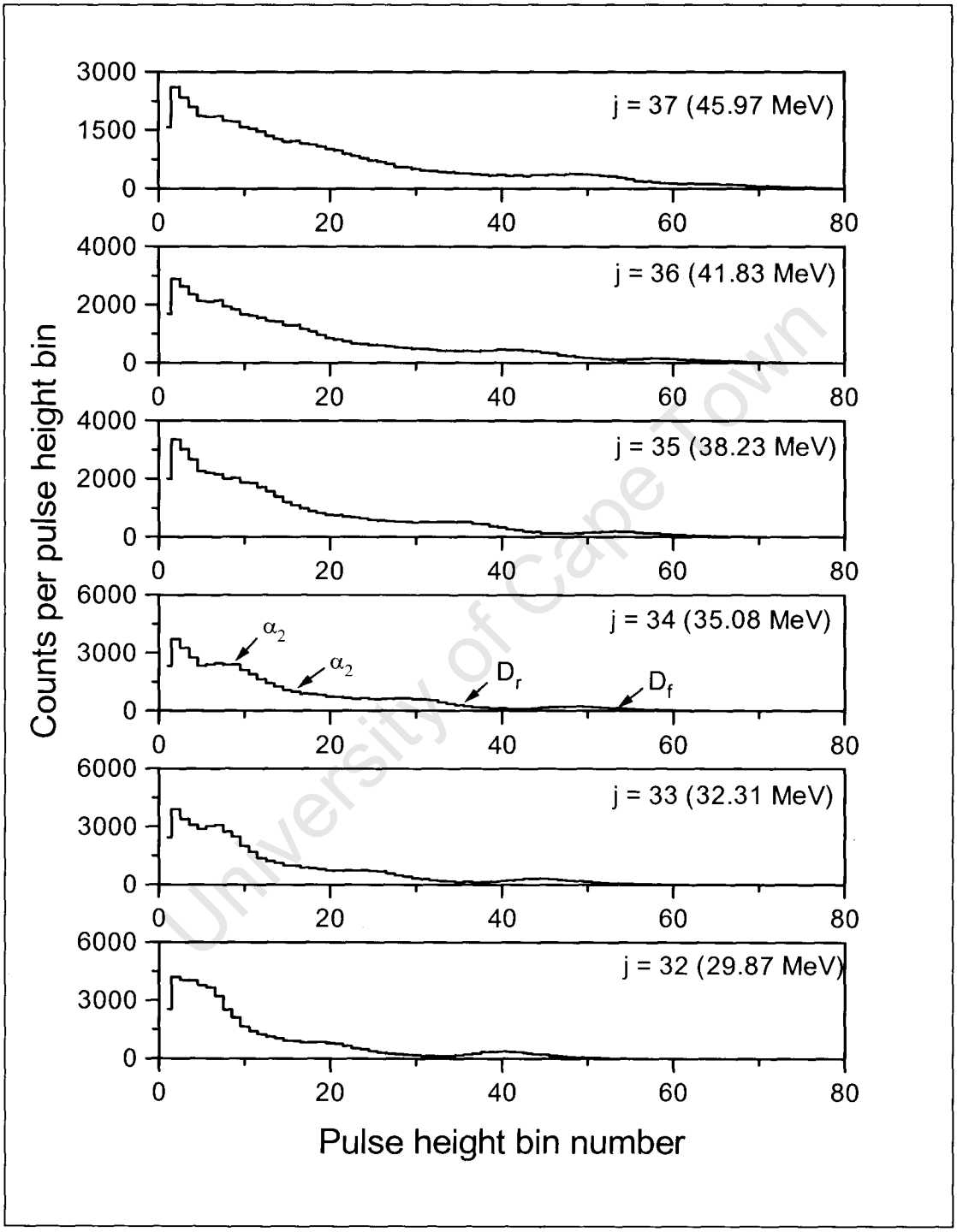

Fig. 3.2(f) *Response functions,(j = 32 to 37) of the NE230 detector when exposed to neutrons of energy indicated.*

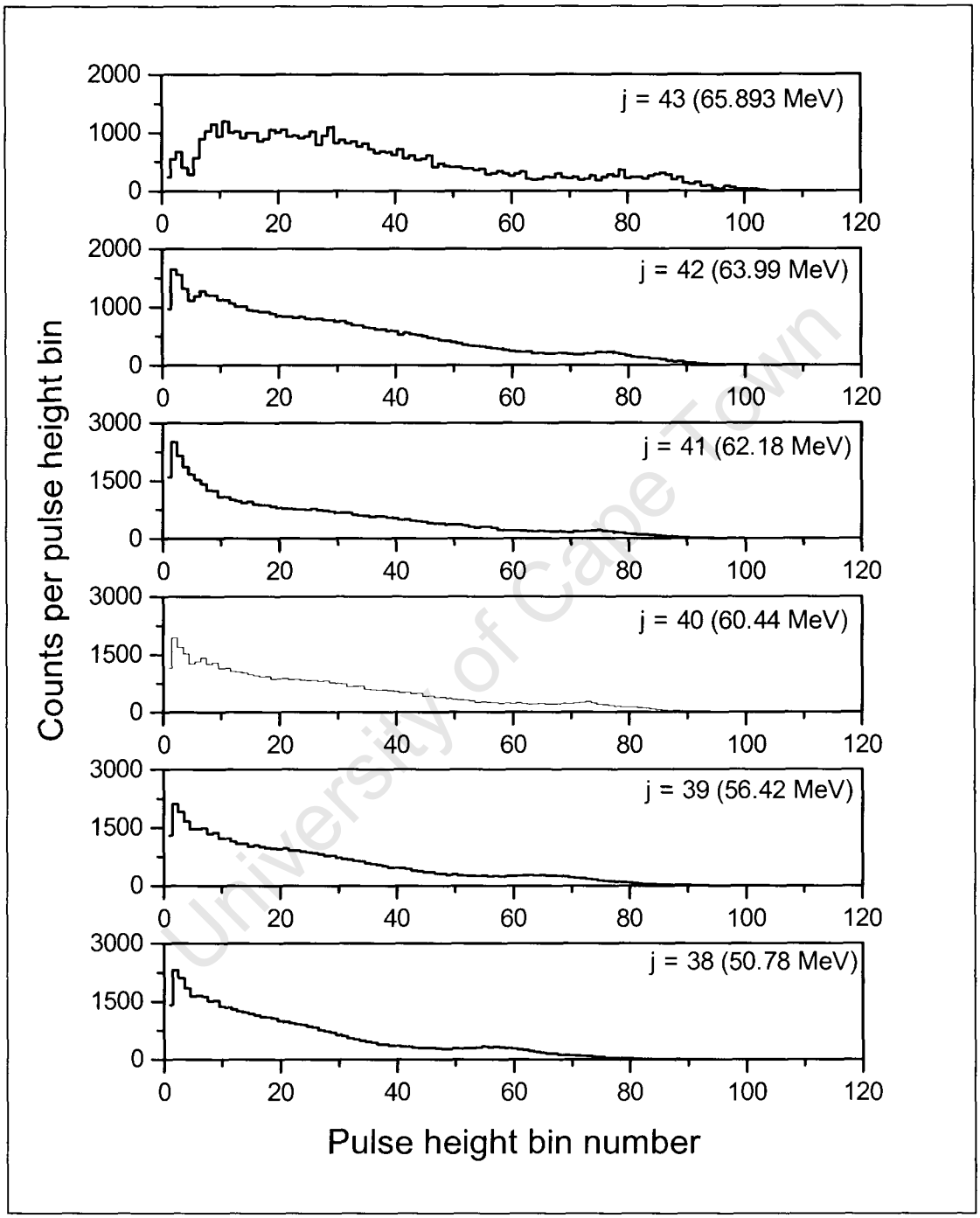

Fig. 3.2(g) Response functions, (j = 38 to 43) *of the NE230 detector when exposed to neutrons of energy indicated.*

The alpha contributions from the two reactions are distinguishable in the response function j = 34 where the label α_2 indicates alphas from the $^{12}C(n,n')3\alpha$ reaction. Note that for alpha particles of energy 10 MeV, 20 MeV and 50 MeV, the percentage that escape from the detector are about 0%, 3% and 9%, respectively.

3.3 Validation of the unfolding procedure using MAXED

Tests of the unfolding procedures were done to validate the reliability of the unfolding code by inputting the pulse height spectra for a number of known energy spectra and comparing the latter with the output from the code. The Li, Be and C spectra that were measured with the NE230 detector using time-of-flight (see section 2.6) were used individually in the initial tests. In each case the energy spectrum produced by MAXED using only the measured pulse height data as input was in excellent agreement with the measured spectrum. More stringent tests were undertaken by constructing four composite spectra from the Li, Be and C data by combining these data in various proportions as indicated in Table 3.2. Fig. 3.3(a)-(b) shows the pulse height spectra and the corresponding energy spectra for each composite spectrum.

Table 3.2: *Percentages of data from Li, Be and C targets used to construct composite spectra A, B, C and D.*

Composite spectrum	Percentage of data used from target (%)		
	Be	C	Li
A	0	25	75
B	0	50	50
C	25	0	75
D	50	0	50

A variety of tests using each of the four pulse height spectra A, B, C and D was carried out in which the prior spectra and the chi-squared criterion were changed in order to see the effect on the output. Two prior spectra were used, namely the energy spectrum from the Li-target determined by time of flight and a "flat" (constant energy) spectrum. The measured response matrix was used in all the tests.

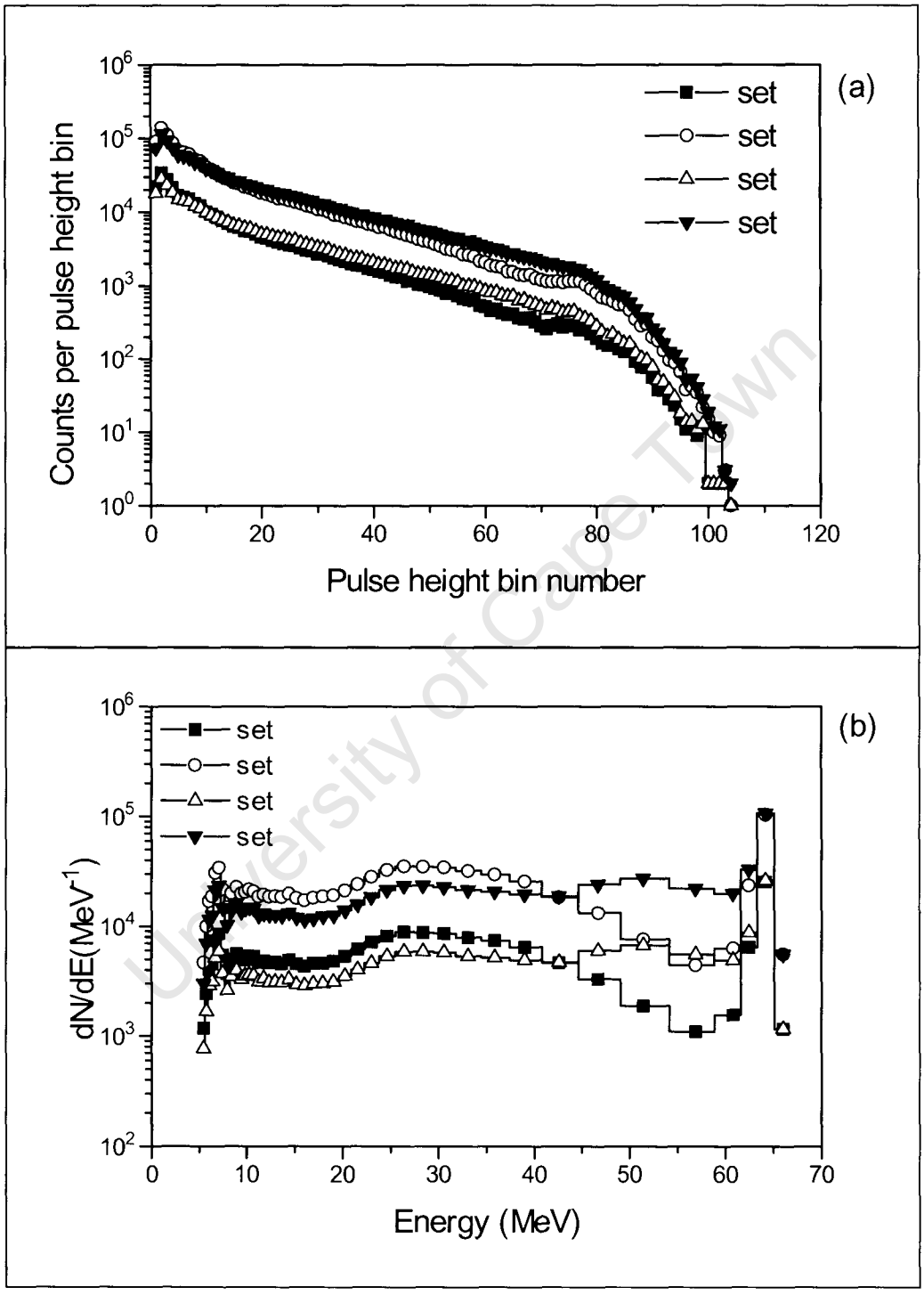

Fig. 3.3 *Composite spectra A-D constructed by combining different proportions of time-of-flight data obtained with the Li, Be and C targets. The upper panel (a) shows pulse height spectra while lower panel (b) shows the corresponding energy spectra.*

The influence of different prior spectra on the results from MAXED is shown in fig. 3.4(a)-(d) while the effects of using different chi-squared criteria are shown in fig. 3.5(a)-(b). In order to facilitate comparison all the spectra are normalised to the same total counts per MeV obtained when using the Li prior spectrum. To facilitate more detailed comparison, the ratios of the unfolded energy spectra to the composite are also presented in table 3.3. The statistical uncertainties for the energy spectra are of the order of the symbols used to indicate the energy spectra and those for the ratios in table 3.3 vary between 1% and 3%.

Fig. 3.4(a)-(d) shows the unfolded energy spectra obtained from MAXED (solid squares spectra obtained with Li prior and open squares spectra obtained with flat prior) compared with the composite spectra that were constructed from the time-of-flight data (solid histogram). The prior spectra are indicated by the dashed (flat) and dotted histogram (Li prior), respectively. The figures and table 3.3 show that all the unfolded energy spectra agree well with the composite spectra across the whole energy range and that the agreement is overall within 10% except in the region 50-65 MeV were it is less in some cases. However, where the composite spectrum includes a strong component from the neutron peak at 64 MeV (fig. 3.4 (a), (b) and (d)), the results using the Li prior spectrum are in better agreement in the region 50-65 MeV, as expected. In the case of the Li prior the agreement is overall within 15% while in the case of the Flat prior the agreement is overall within 20%. In the case of fig. 3.4(c) the composite spectrum does not have a strong peak in this region and the use of the flat prior gives results that are in better agreement (within10%) than with the Li prior. This demonstrates one of the features of Bayesian unfolding in that prior information plays a strong role in the unfolding process, in particular where the data are sparse or where the response matrix have a lower sensitivity to neutron energies. In particular in this case the response matrix had a lower sensitivity to neutron energies at energies > 55 MeV, possibly due to forward recoil deuteron escapes

Fig. 3.5(a)-(b) displays the effects on the output spectra when different chi-squared values are used to terminate the unfolding process. For chi-squared values of 1 and 5, consistent results were obtained and the unfolded energy spectra and the composite spectra agree well over the entire range. Similar results were obtained for the other composite spectra. It is interesting to note that for very large chi-squared values the

unfolded energy spectra converge to the prior spectra as expected. Specifying chi-squared values of less than 1 leads to poorer agreement at both extreme ends of the energy spectrum where the statistical fluctuations in the data are high.

In summary, the results from the tests that were carried out demonstrated that the unfolding process could, in principle, provide meaningful and reliable output from the measured data using a response matrix that was determined by experiment. In addition the ratios in table 3.3 also provide an estimate of the uncertainty associated with the unfolding

Table 3.3 *Ratios of unfolded (MAXED) energy spectra to composite spectra for validation of the unfolding procedures using different prior spectra.*

	Li prior spectrum				Flat prior spectrum			
Composite spectrum / Energy (MeV)	A	B	C	D	A	B	C	D
5.36	1.13	1.23	0.97	1.23	2.33	2.73	2.41	2.80
5.63	1.18	1.26	0.93	1.16	1.23	1.41	1.14	1.34
5.92	1.08	1.16	0.94	1.11	0.91	1.02	0.89	1.03
6.23	0.96	1.04	0.92	1.01	1.11	1.22	1.11	1.30
6.56	0.92	0.97	0.91	0.93	0.89	0.95	0.86	1.01
6.93	0.93	0.97	0.98	0.97	0.83	0.89	0.83	0.96
7.32	0.98	1.04	1.03	1.06	1.11	1.22	1.22	1.36
7.75	0.95	1.07	0.93	1.06	1.26	1.48	1.52	1.71
8.22	0.92	1.08	0.95	1.13	0.87	1.05	1.11	1.27
8.65	0.96	1.06	1.16	1.14	0.95	1.03	1.05	1.19
9.20	0.92	1.00	1.12	1.06	1.05	1.09	1.24	1.31
9.60	0.95	1.01	0.99	0.98	0.98	1.01	1.10	1.15
10.03	1.00	1.04	0.88	0.96	0.91	0.96	1.01	1.01
10.49	1.16	1.11	0.99	0.97	1.18	1.10	1.03	0.98
10.97	1.12	1.07	1.30	1.09	1.26	1.19	1.23	1.26
11.50	0.97	1.01	1.01	1.01	0.92	0.92	1.05	1.03
12.06	0.93	1.00	1.06	1.05	0.86	0.92	1.06	1.11
12.67	0.94	0.97	0.81	0.88	0.92	0.88	0.96	0.87
13.32	1.01	0.99	1.00	0.96	1.06	1.05	1.02	1.01
14.02	0.95	0.95	0.97	0.94	0.88	0.83	0.96	0.90
14.78	0.97	0.97	1.06	1.04	0.95	0.96	1.08	1.03
15.61	0.97	0.96	1.01	1.02	0.98	0.96	1.09	1.02
16.51	0.98	0.94	0.96	0.97	1.00	0.95	1.03	0.93
17.49	0.99	0.94	0.97	0.96	0.96	0.88	1.01	0.84
18.56	1.00	0.96	1.10	1.05	0.95	0.91	1.07	0.89
19.73	1.07	0.98	1.06	1.00	1.07	0.92	1.05	0.84
21.02	1.05	1.00	1.09	1.07	1.02	0.94	1.02	0.90
22.43	1.06	1.01	1.07	1.06	1.03	0.97	0.94	0.88
24.00	1.06	1.00	1.07	1.01	1.00	0.92	0.86	0.84
25.75	1.05	0.98	0.94	0.92	0.99	0.91	0.77	0.76
27.69	1.06	1.00	0.83	0.88	0.97	0.90	0.73	0.72
29.87	1.01	0.97	0.86	0.91	0.98	0.95	0.76	0.80
32.31	0.94	0.94	0.87	0.95	0.92	0.99	0.86	0.93
35.08	0.94	0.91	0.99	0.99	0.96	0.99	1.01	1.02
38.23	0.94	0.91	1.03	1.00	1.04	1.03	1.12	1.04
41.83	1.04	1.06	1.17	1.15	1.09	1.16	1.21	1.19
45.97	1.19	1.15	0.98	0.97	1.13	1.07	0.93	1.01
50.78	1.65	1.27	0.96	0.92	1.41	1.05	0.82	0.87
56.42	0.91	1.02	0.73	0.66	1.69	1.55	0.96	1.08
60.44	0.85	0.97	0.48	0.61	2.78	2.84	1.18	1.75
62.18	1.15	1.09	1.15	1.08	1.52	1.38	1.13	1.25
63.99	0.94	0.94	1.52	1.15	0.47	0.61	0.63	0.55

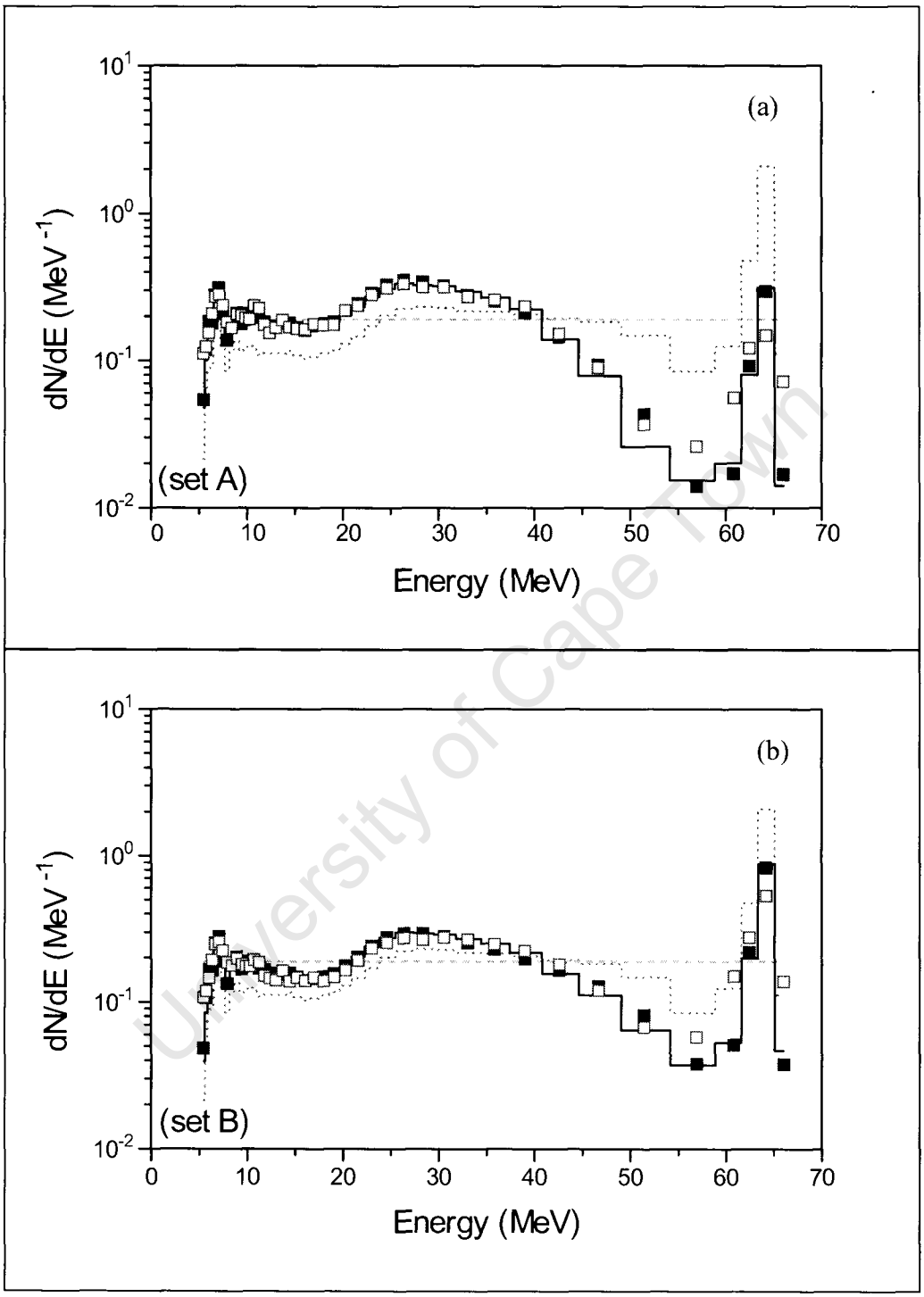

Fig. 3.4 *Unfolded energy spectra obtained from MAXED (solid squares spectra obtained with Li prior (dotted histogram) and open squares spectra obtained with flat prior (dashed line)) compared with the composite spectrum that were constructed from the time-of-flight data (solid histogram). The upper panel (a) shows results for composite spectrum A while the lower panel (b) shows results for composite spectrum B.*

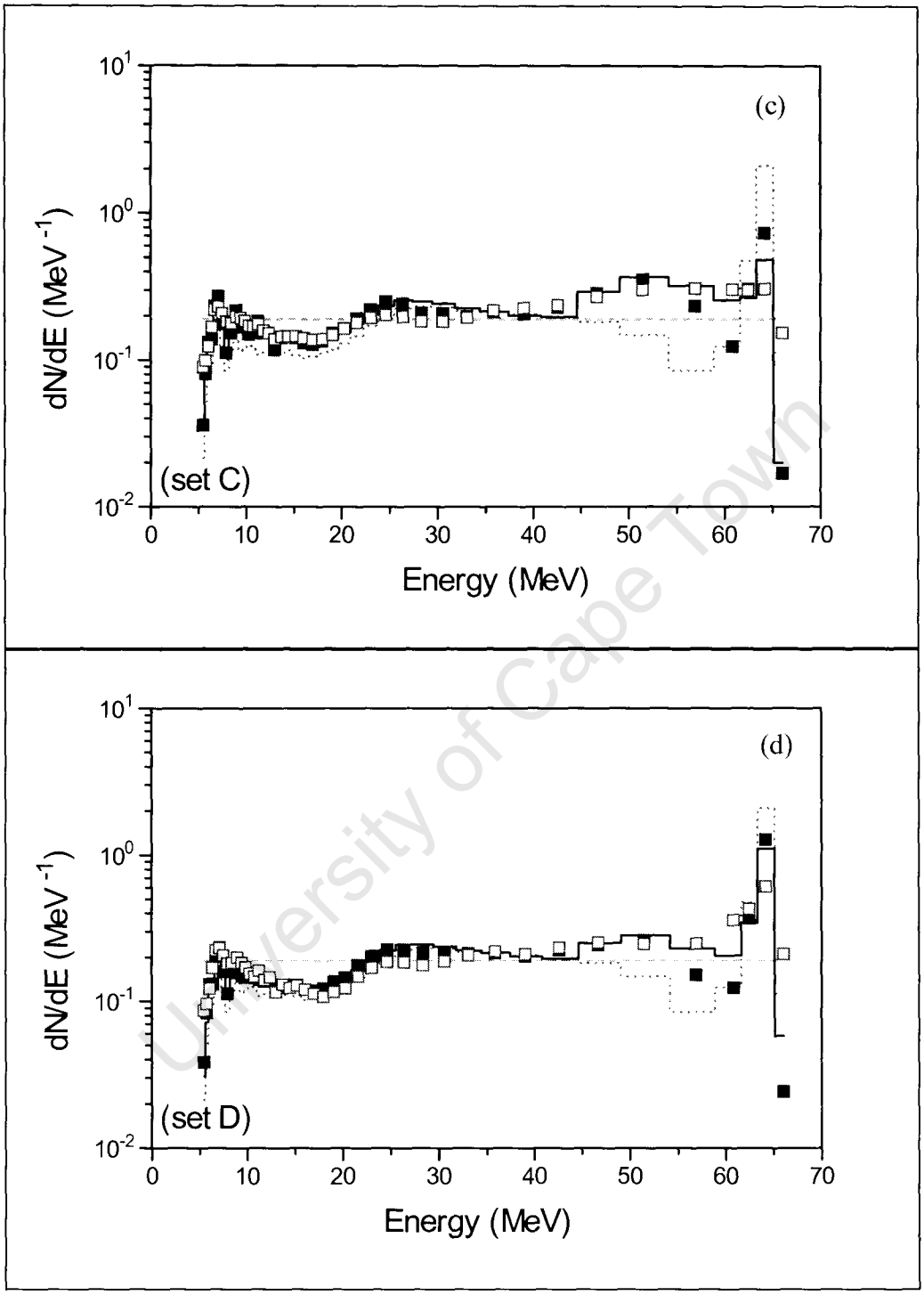

Fig. 3.4 *Unfolded energy spectra obtained from MAXED (solid squares spectra obtained with Li prior (dotted histogram) and open squares spectra obtained with flat prior (dashed line)) compared with the composite spectrum that were constructed from the time-of-flight data (solid histogram). The upper panel (c) shows results for composite spectrum C while the lower panel (d) shows results for composite spectrum D.*

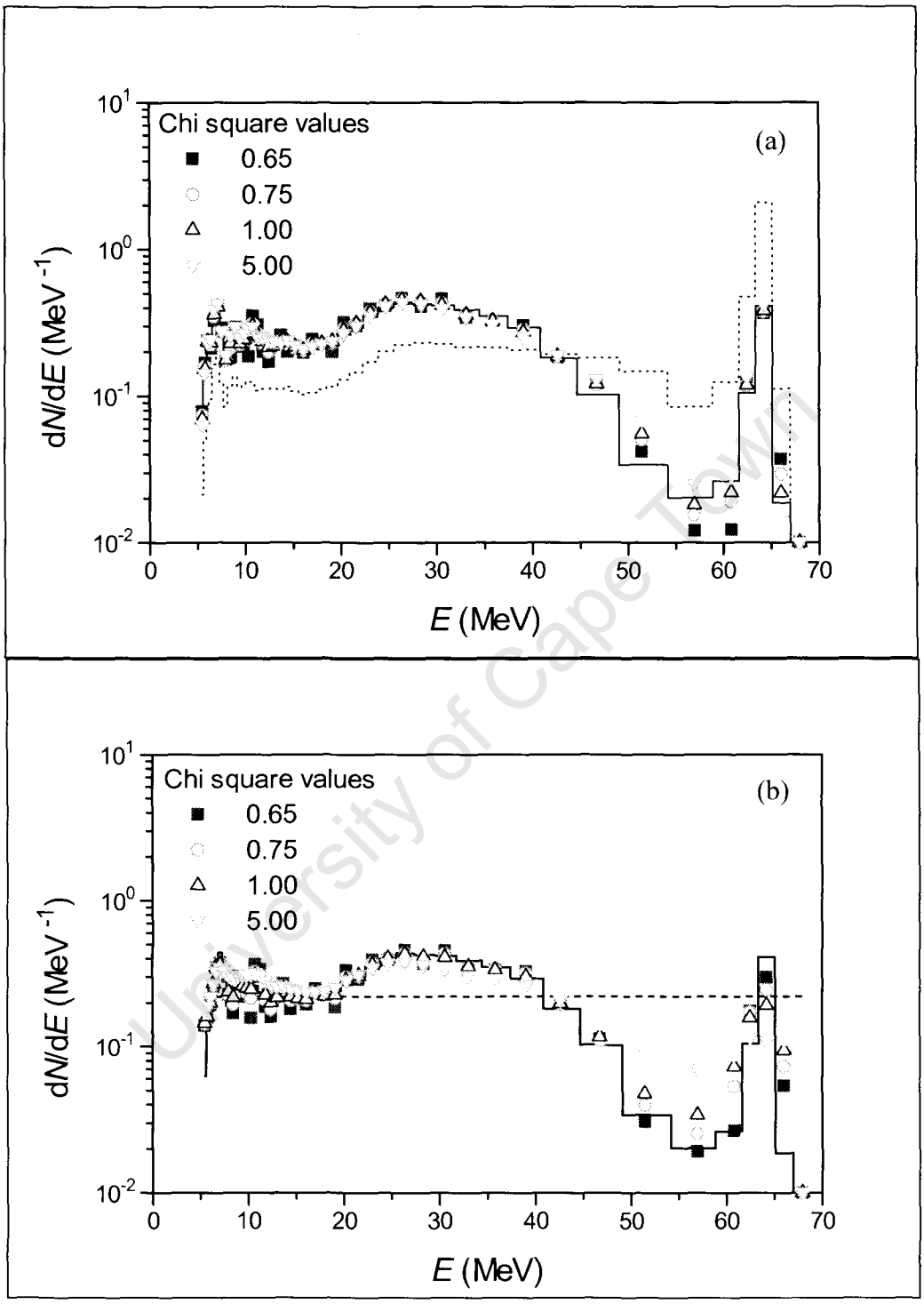

Fig. 3.5 *Composite energy spectrum determined by time-of-flight (solid histogram) compared with unfolded energy spectra obtained for different chi-squared values used. The upper panel (a) shows results obtained for different chi-squared values used with the Li prior(dotted histogram) while the lower panel (b) shows results for different chi-squared values used with the flat prior (dashed line).*

3.4 Unfolding of the in-phantom measurements

The pulse height spectra from the in-phantom measurements (figs. 2.18(a)-(c)) were unfolded into neutron energy spectra via MAXED using the experimentally measured response matrix for NE230 (see section 3.2). Each response function was normalized to 50000 integral counts. The Li spectrum was used as prior information in all the cases discussed below. The MAXED unfolding of a measured pulse height spectrum L_k, for k = 1 to 104 pulse height bins, determined a set of energy bin values a_i, for i = 1 to 43 energy bins, of the neutron energy spectrum $N_i(E_i)$, see equation (3.2). The energy bin value a_i for neutron bin i is related to the number of incident neutrons N_{oi} in the energy range corresponding to this bin by

$$a_i = \frac{\varepsilon_D(E_i, L_D) N_{oi}}{50000} \tag{3.3}$$

Where $\varepsilon_D(E_i, L_D)$ is the neutron detection efficiency of the NE230 detector (see appendix A) for incident neutrons of energy E_i corresponding to bin i and pulse height threshold L_D. The number of neutrons N_i for bin i (defined here as the number of incident neutrons per unit energy delivered to the NE230 detector) is given by

$$N_i = \frac{50000 a_i}{\Delta E_i \varepsilon_D(E_i, L_D)} \tag{3.4}$$

Where ΔE_i is the width of energy bin i. The neutron energy spectrum $N_i(E_i)$ for each set of measurements was determined using

$$N_i(E_i) = \frac{50000 a_i}{\Delta E_i \varepsilon_D(E_i, L_D)} \quad \text{for } i = 1 \text{ to } 43 \text{ energy bins} \tag{3.5}$$

The uncertainty $\Delta N_i(E_i)$ in the neutron energy spectrum $N_i(E_i)$ arises from the input quantities used in equation (3.5). The uncertainty of the energy bin value a_i is due to uncertainties in the response matrix, the prior spectrum and pulse height spectra used as input in MAXED. The main sources of systematic uncertainty in these are due finite size of the detector, which includes deuteron escapes and multiple neutron scattering. For the respective energies 10 MeV and 50 MeV about 3% and 57% of the deuterons would escape from the detector. The "escape effect" was corrected for in

the calculation of the neutron detection efficiency of the NE213 detector as a function of neutron energy, as detailed in appendix A and which is accurate to within 10% based on the method used over the range of neutron energies [Bu90]. The uncertainty due to multiple neutron scattering is small due to the size of the detector and is estimated to be within 3% over the range of neutron energies [Pa73]. Other sources of systematic uncertainty are a result of the data reduction and include the loci in the L-S plots to select the particles of interest (see section 2.5), time-of-flight to neutron energy calibration (section 2.6.2) and the measurement of peaks and edges in the response functions (section 2.6.3). The uncertainties associated with these are difficult to assess and was estimated by repeating analysis and to observe any differences in the results. This has been done at different neutron energies and the difference observed in the results was of the order of 4 %. The overall systematic uncertainty was calculated by the quadratic summations of the components discussed above and is in the order of 11%. This will be similar for all the spectra measured and as a consequence, the differences in the measured neutron energy spectra observed are therefore significant. The statistical uncertainty in the response matrix, the prior spectrum and pulse height spectra are mainly due to the uncertainties in the total number of counts in each spectrum. The statistical uncertainty was estimated to be less than 2% as the number of counts in each spectrum was greater than 10000.

How these systematic and statistical uncertainties propagate through the unfolding is difficult to assess [Ma02] and still remains a challenge [Th02]. The uncertainty in the energy bin value a_i has been taken to 10% of the value of a_i obtained from the unfolding which is within 10% the result of overall agreement between composite and unfolded spectra obtained in validation tests of the unfolding procedures (see section 3.3). The neutron detection efficiency $\varepsilon_D(E_i, L_D)$ with uncertainty $\Delta\varepsilon_D(E_i, L_D)$ was calculated for each energy bin, as detailed in appendix A. The uncertainty in ΔE_i the width of energy bin was calculated using equation (2.6) section 2.6.2. The combined statistical uncertainty $\Delta N_i(E_i)$ was calculated by the quadratic summations of these components for equation (3.5) from which $N_i(E_i)$ were calculated.

The final results (neutron energy spectra with respective statistical uncertainties) from the unfolding of the measurements carried out at various positions in the phantom are

shown in figs. 3.6(a)-(c). Positions are indicated as (d, r), where d is the depth in cm along the beam axis and r is the lateral distance in cm from the beam axis. The spectra shown in the figures are normalized to the same number of neutrons measured by the neutron monitor per MeV. For the purposes of comparison between the various spectra, integral counts in the peak region (56.42 to 65.89 MeV) and the tail region (5.36 to 56.42 MeV) were calculated and the ratios computed. These ratios, summarised in Table 3.4, are an indication of the proportions of high energy neutrons (peak region) to low energy neutrons (tail region). The uncertainties shown in the table for each integral count was calculated by the quadratic summations of the uncertainty $\Delta N_i(E_i)$ from each $N_i(E_i)$ obtained as discussed above. The uncertainty shown with the ratio was calculated by the quadratic summations of the uncertainties in the peak and tail for the ratio.

Table 3.4: *Integral counts in the peak and the tail regions of the neutron spectra together*

Position (d, r) cm	Integral Counts		Ratio (Peak to Tail)
	Peak region (56.45 to 65.89 MeV)	Tail region (5.36 to 56.45 MeV)	
Air	$12.5\text{x}10^6 \pm 3.6\text{x}10^6$	$93.6\text{x}10^5 \pm 1.5\text{x}10^5$	1.34 ± 0.39
(6, 0)	$12.0\text{x}10^6 \pm 3.4\text{x}10^6$	$91.7\text{x}10^5 \pm 1.6\text{x}10^5$	1.31 ± 0.38
(8, 0)	$11.4\ \text{x}10^6 \pm 3.1\text{x}10^6$	$82.2\text{x}10^5 \pm 0.9\text{x}10^5$	1.38 ± 0.38
(20, 0)	$7.7\text{x}10^6 \pm 2.1\text{x}10^6$	$34.1\text{x}10^5 \pm 0.6\text{x}10^5$	2.27 ± 0.62
(30, 0)	$6.0\text{x}10^6 \pm 1.6\text{x}10^6$	$21.4\text{x}10^5 \pm 0.4\text{x}10^5$	2.82 ± 0.77
(40, 0)	$3.3\text{x}10^6 \pm 0.9\text{x}10^6$	$9.5\text{x}10^5 \pm 0.2\text{x}10^5$	3.47 ± 0.95
(8, 2)	$11.5\text{x}10^6 \pm 3.3\ \text{x}10^6$	$88.1\ \text{x}10^5 \pm 1.5\text{x}10^5$	1.30 ± 0.37
(8, 4)	$1.4\text{x}10^5 \pm 0.3\ \text{x}10^5$	$48.2\text{x}10^4 \pm 0.8\ \text{x}10^4$	0.29 ± 0.06
(8, 7.5)	$1.8\text{x}10^4 \pm 0.5\ \text{x}10^4$	$21.4\text{x}10^5 \pm 0.4\text{x}10^4$	0.088 ± 0.023
(20, 4)	$5.3\text{x}10^5 \pm .4\text{x}10^5$	$51.0\text{x}10^4 \pm\ 0.8\ \text{x}10^4$	1.04 ± 0.27

Fig. 3.6(a) shows the neutron energy spectra for positions along the beam axis in the phantom. The spectra at depths 6 cm to 40 cm are similar in shape to the in-air spectrum. The neutron peak at 64 MeV is reduced in intensity while the resonance structure is well reproduced in the spectra with increasing depth into the water

phantom. The results also indicate that with increasing depth the neutron beam is attenuated but the proportion of high-energy neutrons to low energy neutrons increases as is evident from Table 3.4. This hardening of the spectra with increasing depth is attributed to behaviour of the n-p elastic cross-section which decreases with increasing neutron energy [Ro91]. For example, the n-p elastic cross-section at 10 MeV is 0.92 barn and for 50 MeV neutrons it is 0.16 barn; i.e the lower energy neutrons are scattered out of the beam at a much faster rate than the higher energy neutrons as the beam progresses through the water. Thus, at increasing depths along the beam axis, the neutron beam has a higher proportion of high energy neutrons than low energy neutrons.

Figs 3.6(b) and 3.6(c) show the spectra measured off the beam axis. Fig. 3.6(b) shows the neutron energy spectra for positions off the beam axis at a depth 8 cm into the phantom. The spectra at positions (8 cm, 0 cm) and (8 cm, 2 cm) are similar in shape to the in-air spectrum, and the neutron peak at 64 MeV and resonance structure is similar in strength to the in-air spectrum. Below 55 MeV the shapes of the spectra at positions (8 cm, 4 cm) and (8 cm, 7.5 cm) are different to that of the in-air spectrum. Above 55 MeV the neutron peak at 64 MeV still looks similar to the in-air spectrum although it is smaller. The spectra clearly indicate that with increasing lateral distance from the beam axis, the neutron flux decreases and the proportion of low energy neutrons to high energy neutrons increases (see Table 3.3) due to the kinematic effect.

Fig. 3.6(c) shows comparisons between the neutron energy spectra measured at depths 8 cm and 20 cm, respectively, for lateral distance 4 cm off beam axis in the phantom. The shapes of the spectra are different to each other and also different to the shape of the spectrum in-air. The neutron peaks at 64 MeV are much smaller than for the spectrum in-air and the resonance structure is well reproduced. As expected from kinematic considerations, the spectrum at position (20 cm, 4 cm) shows a higher proportion of high energy neutrons than for the spectrum at (8 cm, 4 cm).

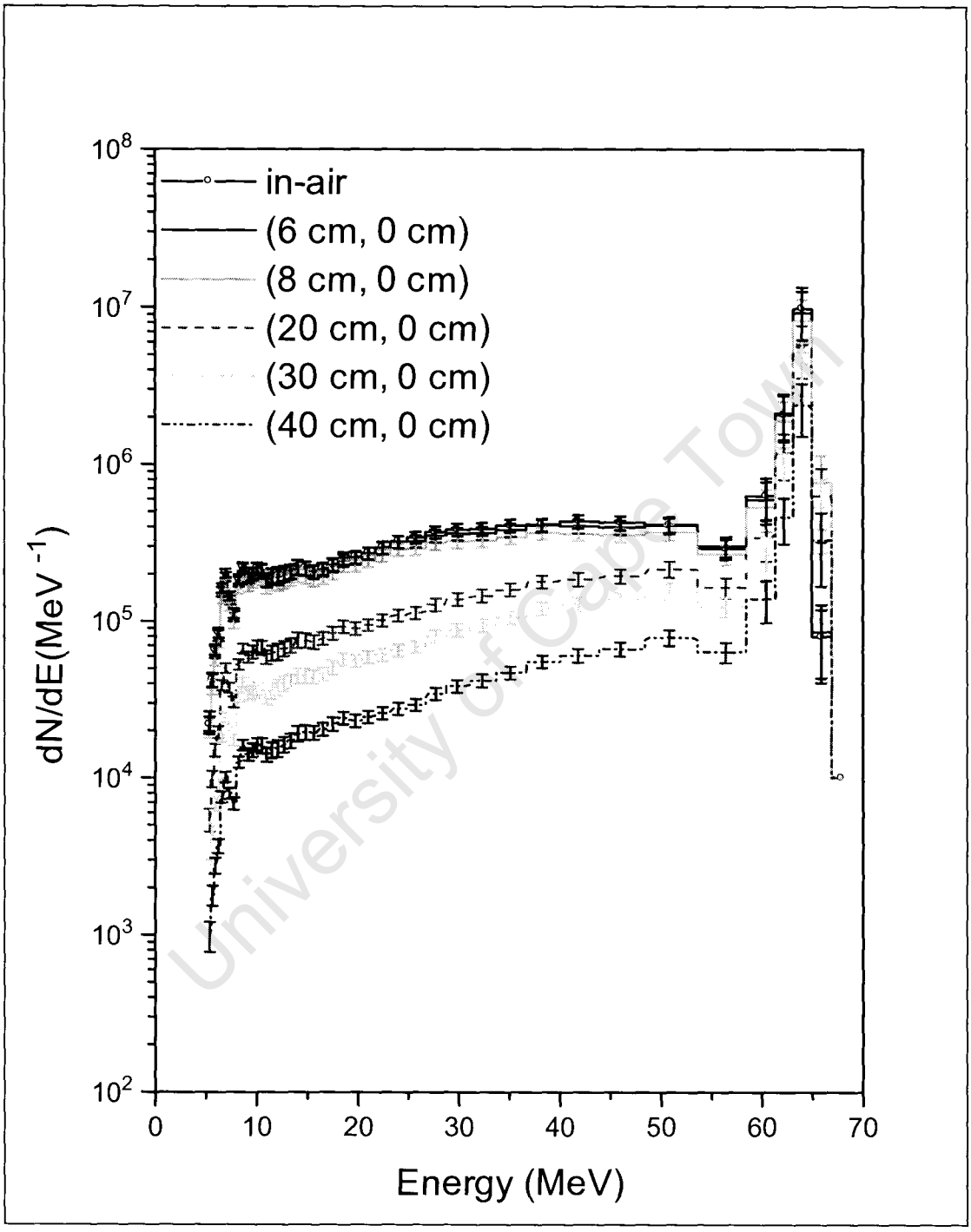

Fig. 3.6(a) E*nergy spectra measured at different depths along the beam axis in the phantom compared with the in-air spectrum.*

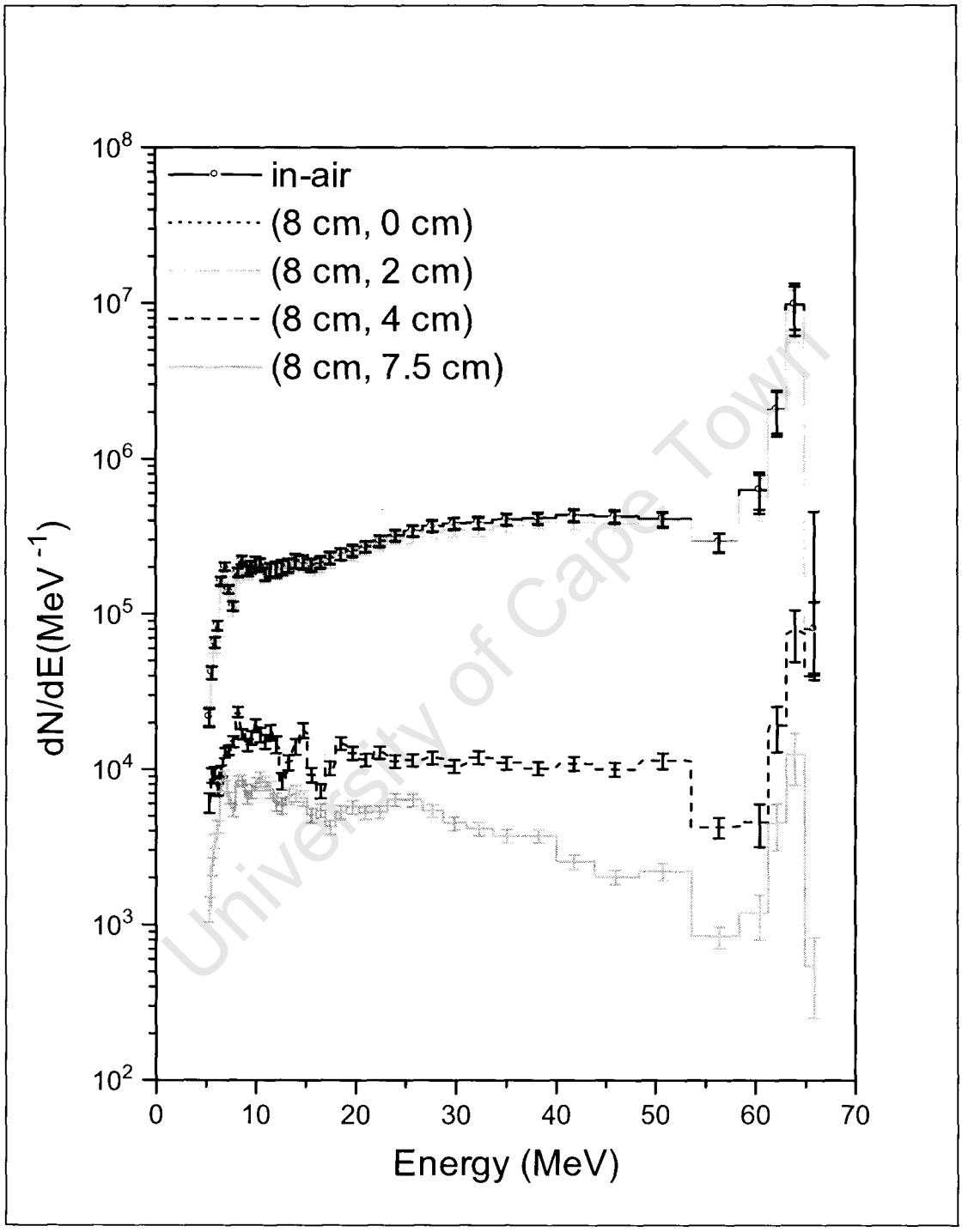

Fig. 3.6(b) E*nergy spectra measured at different positions off the beam axis in the phantom compared with the in-air spectrum.*

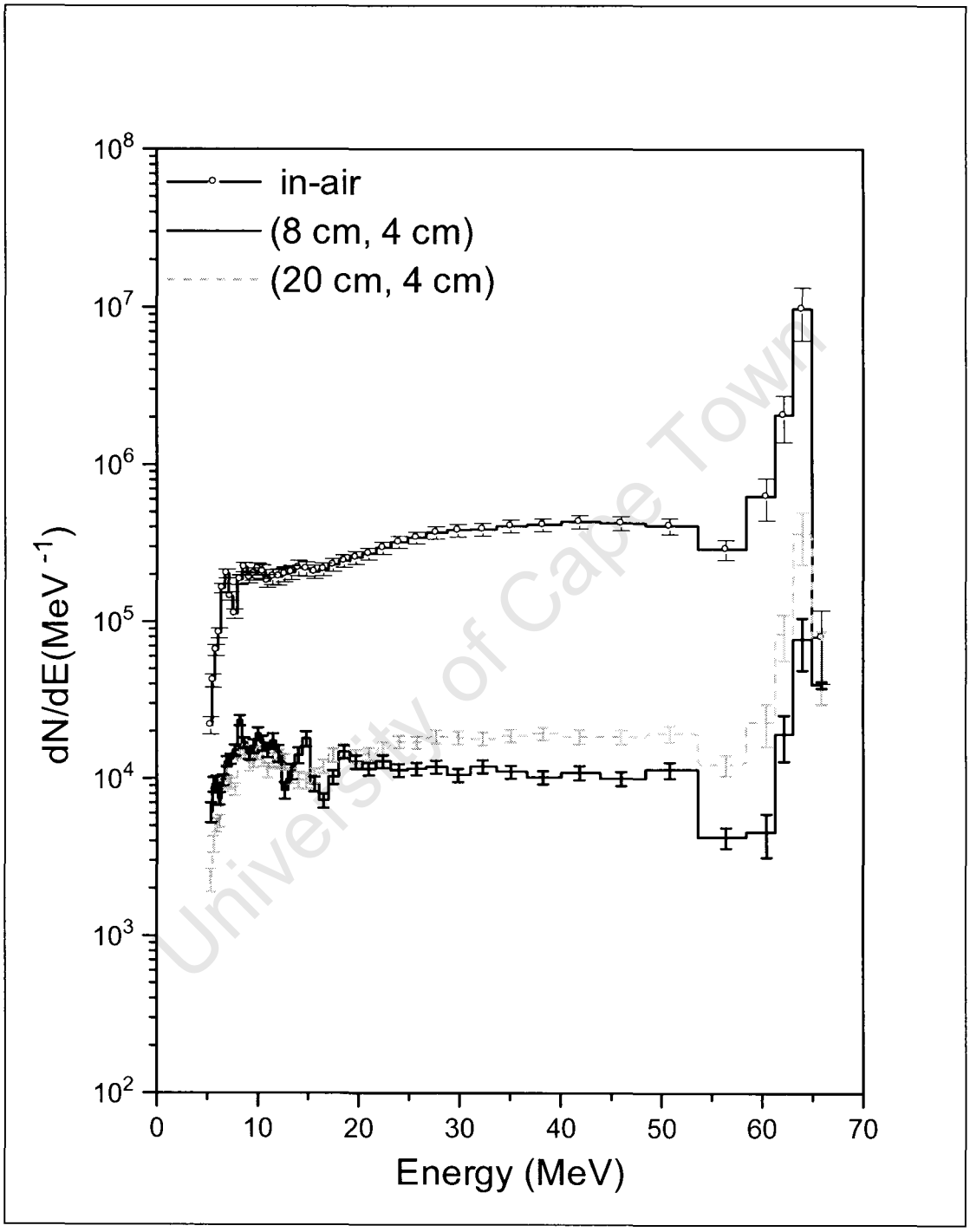

Fig. 3.6(c) *Energy spectra measured at different positions off the beam axis in the phantom compared with the in-air spectrum.*

CHAPTER 4

MCNPX MONTE CARLO SIMULATIONS

4.1 Introduction

The Monte Carlo code MCNPX is widely used in nuclear physics for simulating the transport of particles through matter [Hu97, Wa99]. MCNPX describes the physics of the nuclear interactions that take place by using: (a) evaluated nuclear data libraries (see section 1.2) or (b) various physics models, including intranuclear cascade models [Be69, Ya81] where libraries are not available [Ro91]. In the present work MCNPX was used to simulate the experiments that were carried in chapter 2 in order to calculate how the energy spectrum of the neutron beam (5 to 64 MeV neutrons) varies as a function of position as it passes through the water phantom. In the simulations neutrons were transported through air, water, vacuum, polyvinyl chloride (PVC) and NE230 to detector positions in the phantom where the energy spectrum of the beam was calculated.

Fig. 4.1 shows a flow chart outlining the broad features of a neutron history as it is tracked by MCNPX. Fig 4.2(a) shows details of the initialization of a neutron as it is launched and enters a cell. Fig 4.2(b) shows how the neutron track length is calculated and used for deciding the fate of the neutron, namely, whether or not it experiences an interaction in the cell or passes into the next cell. In the latter case the surface tally is recorded. If the neutron remains in the cell, its energy and position are recorded. Fig. 4.2(c) shows an example of a typical neutron history from source until its energy is tallied in the phantom at the position indicated. As indicated, a neutron collision occurs at event 1 in which the neutron is elastically scattered in a direction that is selected randomly from the physical scattering distribution. At event 2, the neutron is inelastically scattered in the direction shown. A photon produced in this process is scattered at event 4 and leaks out of the water phantom at event 5. At event 3, the inelastically scattered neutron scatters into the detector and the energy distribution is tallied. The neutron terminates in the detector completing its history.

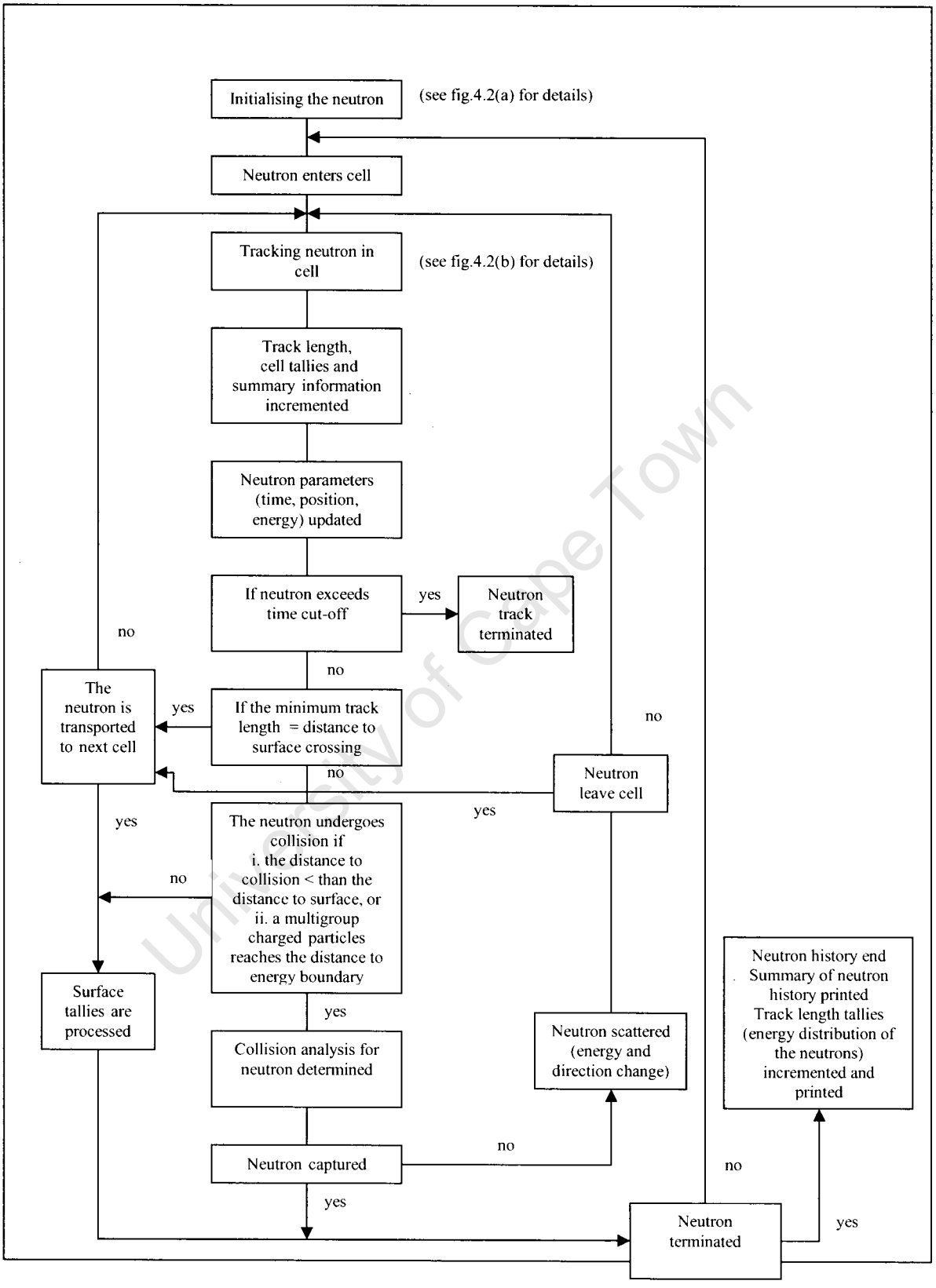

Fig. 4.1 *Flow chart of a neutron history tracked by MCNPX in a cell. See text for details.*

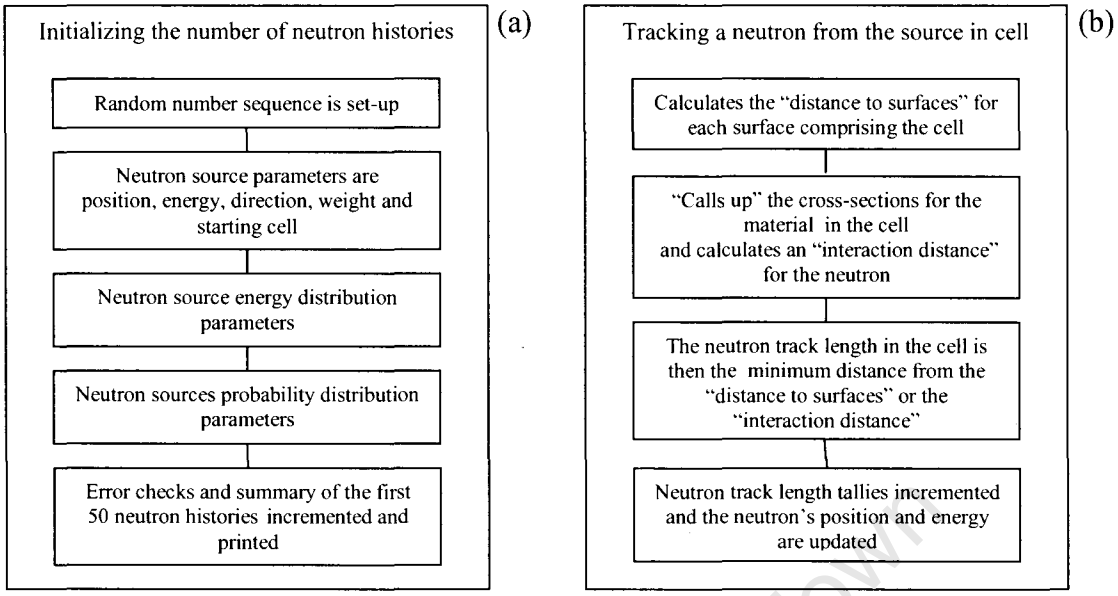

Fig. 4.2 *Details of neutron history showing (a) initialising procedure and (b) tracking routine.*

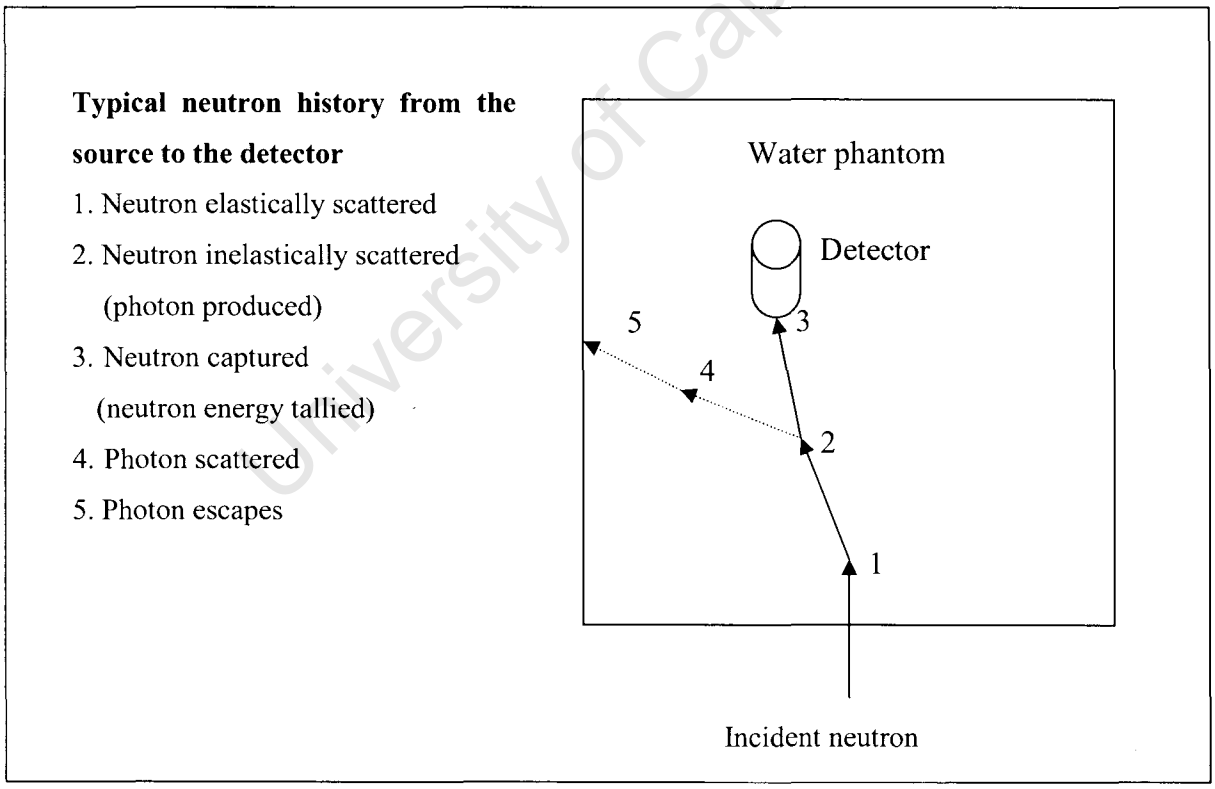

Fig. 4.2(c) *Example of a neutron history in a water phantom.*

4.2 Modelling the source distribution and the geometry

The neutron energy spectrum for the Li-target measured by time-of-flight in-air was used as the neutron source spectrum. The neutron energy spectrum was subdivided into energy bins of different widths, which were identified by the mean energy of each bin as displayed in table 3.1, section 3.2. The neutron source was placed at a distance of 1.5 m from the front face of the phantom along the beam axis and modelled as a circular surface source (diam. 2.5 cm) with the source neutrons emitted in a cone (opening angle of emission of cone 0.795 degrees, see Appendix C) along the beam axis with the diameter of the cone at the centre of the phantom 5.0 cm.

The phantom was modelled as a cube (60 cm x 60 cm x 60 cm) placed in a "room" that was also modelled as a cube (500 cm x 500 cm x 500 cm). The walls of the room and the outside of the room were modelled as vacuums The detector assembly was modelled a series of cylinders that included the detector (diam. 2.5 cm x 2.5 cm), the photo-multiplier tube (PM) (diam. 6.0 cm x 28.75 cm) and the polyvinyl chloride holder (PVC) (diam.7.0 cm x 22.75 cm). Tallying was done on a sphere placed inside the detector. Fig. 4.3, a plot generated by MCNPX, shows the geometry of the detector assembly placed in the path of the neutron beam.

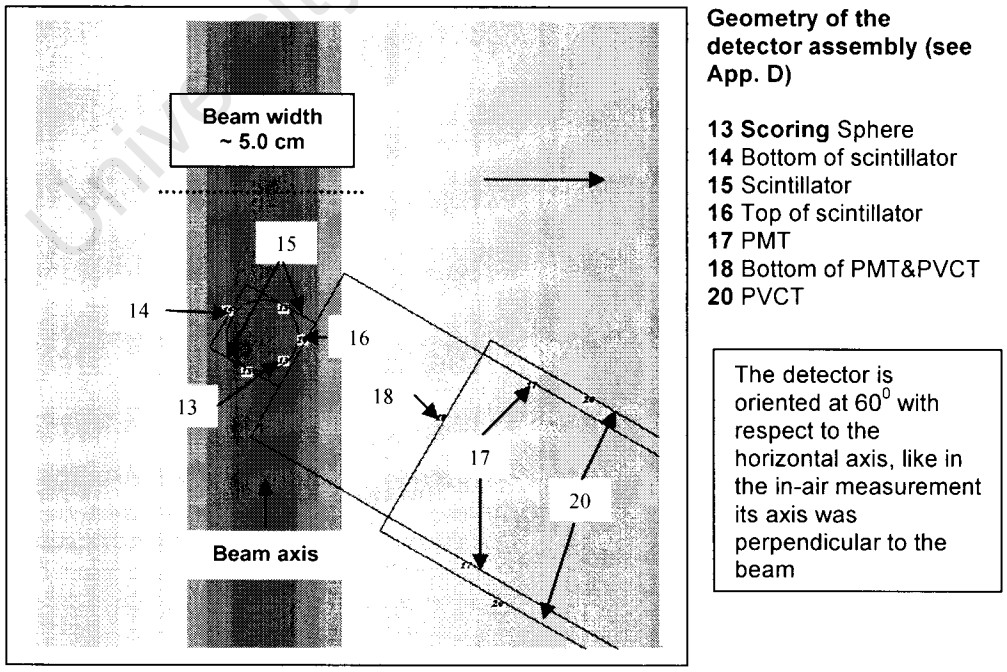

Fig. 4.3 *Plot from MCNPX showing the modelling of the detector assembly. The red-yellow shading indicates the path of the neutron beam. The green shading indicates the background.*

MCNPX was used to simulate the shape of the spectra at various positions in the phantom which were either illuminated directly by the beam at positions (26 cm, 0 cm), (30 cm, 0 cm) and (30 cm, 2 cm) or completely outside the beam at position (30 cm, 7.5 cm). For these calculations all geometric cells in the simulation comprised vacuums and all reaction cross-sections were removed from the MCNPX input file. The results of these simulations (fig 4.4) show that MCNPX reproduced the source energy spectrum as expected at the first three positions while outside the direct path of the beam i.e. at (30 cm, 7.5 cm) no neutrons were counted. The spectrum shown by the histogram and the spectra shown by the dots in the fig. was normalized to per single incident neutron per MeV per cm^2 for comparisons.

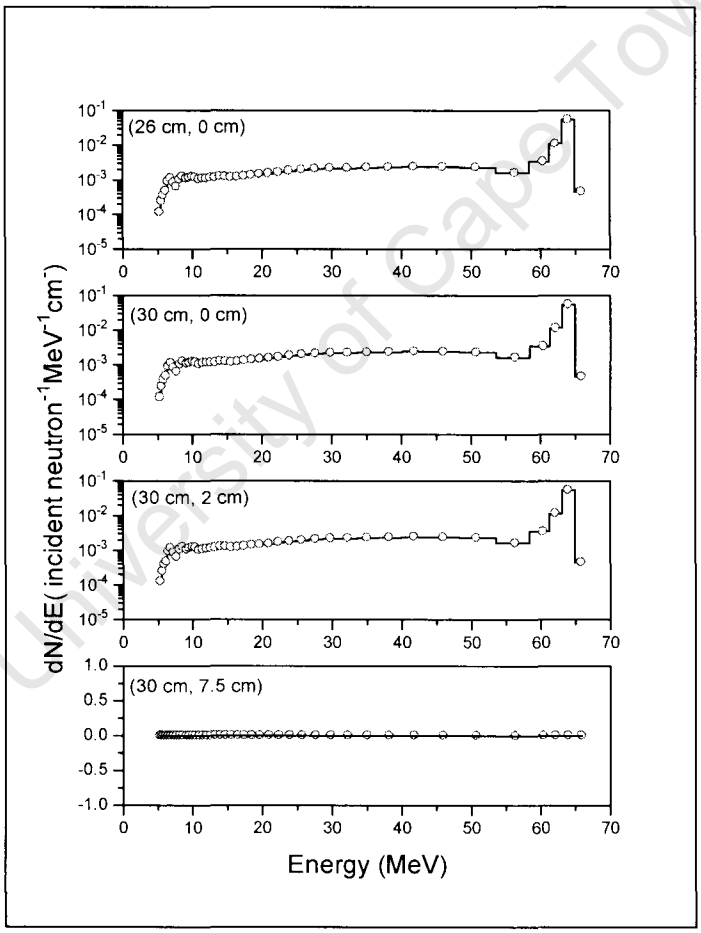

Fig. 4.4 *The top three panels show MCNPX simulations of the spectra (open circles) at positions which are illuminated in the direct path of the beam compared with the input source spectrum (histogram). The bottom panel shows a simulation using the same source spectrum at a position that is outside the direct path of the beam indicating no neutrons as expected. The simulations were done in "vacuum".*

4.3 Simulations of neutron energy spectra

4.3.1 Perturbation effect of the detector assembly on the energy spectra

MCNPX was used to investigate effect of the detector assembly on the neutron energy spectrum by simulating the following three situations at the centre of the water phantom: (1) no detector present, (2) only the NE320 cell present and (3) the complete detector assembly present. Fig. 4.5(a)-(b) shows the results obtained from the 3 simulations, from which it is clear that the detector assembly has a negligible effect on the neutron energy spectrum. Each spectrum was normalized to per single incident neutron per MeV. A detailed comparison indicated that the detector assembly introduced a perturbation of less than 1%.

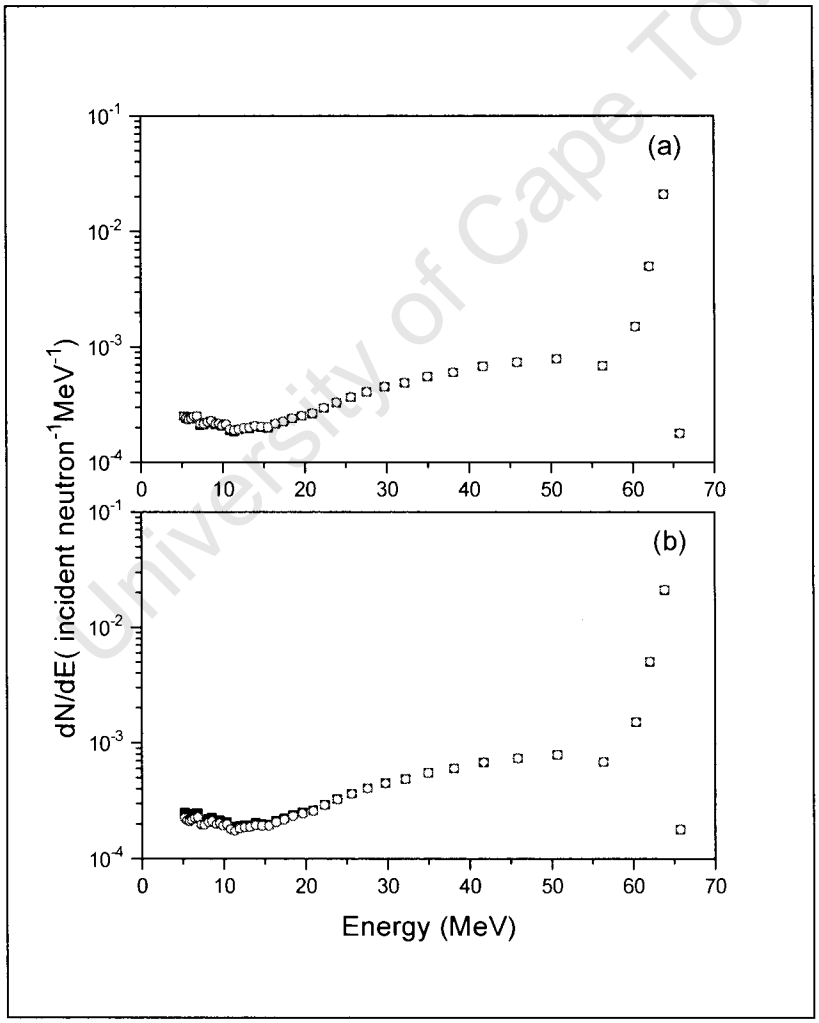

Fig. 4.5 *Results from MCNPX showing neutron spectra at the centre of the water phantom with (a) no detector present (solid squares); NE230 cell present (open circles), and (b) no detector present (solid squares; detector assembly present (open circles).*

4.3.2 Simulations in the water phantom

Simulations of the experimental measurements were carried out at the positions in the water phantom corresponding to those at which measurements were taken. The material isotopic composition and density for the room, phantom and detector assembly components used are indicated in the MCNPX input file shown in Appendix C. Table 4.1 shows the materials used in the simulations.

Table 4.1 *Geometric cells and their material composition used in the MCNPX simulations.*

Geometric cells	Material
Room (Cube)	Air
Phantom (Cube)	Water
Detector (Cylinder)	Deuterated benzene
PM-tube (Cylinder)	Vacuum
PVC-holder (Cylinder)	Polyvinyl chloride
Scoring sphere (Sphere)	Deuterated benzene

Fig 4.6 shows a plot generated by MCNPX indicating the passage of the neutrons through the water phantom. The plot also indicates the detector at the various positions in the water phantom where measurements were made. The figure shows that at positions (6 cm, 0 cm), (8 cm, 0 cm), (20 cm, 0 cm), (30 cm, 0 cm), (40 cm, 0 cm) and (8 cm, 2 cm) the detector is in the direct path of the beam and is predominantly illuminated by neutrons that come directly from the source while at positions (8 cm, 4 cm), (8 cm, 7.5 cm) and (20 cm, 4 cm) the detector is outside the direct path of the beam and is illuminated by neutrons that have previously undergone scattering.

For the Monte Carlo calculations the systemic uncertainties in the neutron energy spectrum $N_i(E_i)$ arise from the LA 150 MeV data libraries and nuclear models used in MCNPX as well as those due to modelling the neutron sources and experimental setup. The uncertainties associated with the LA 150 MeV data libraries and nuclear models are difficult to assess but are thought to be within 5%. Those due modelling the neutron sources and experimental setup were estimated by repeating Monte Carlo calculations with small changes in the modelling and differences in the results

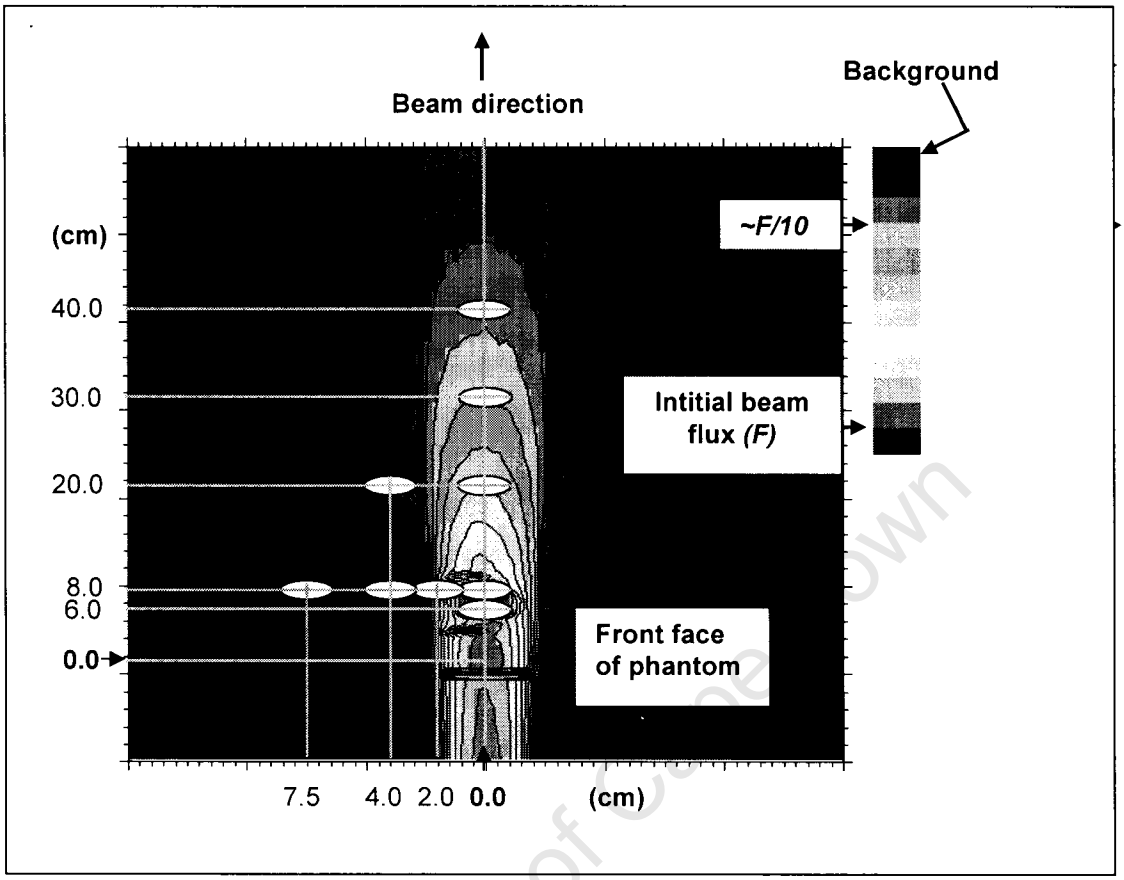

Fig. 4.6 *Plot showing the neutron beam (flux) as it progresses through the water phantom. Ellipses (distorted circles due to scale) show detector positions where measurements were carried out.*

observed was less than 3%. The overall systematic uncertainty was calculated by the quadratic summations of the components discussed above and is in the order of 7%. As with the measurements these uncertainties will be of the same order for all the spectra calculated and as a consequence, the differences in the calculated neutron energy spectra observed are therefore significant. Statistical uncertainties are due to the input source energy spectra of the Li-target measured in-air by time-of-flight. This was calculated as discussed in section 3.4 and lies within 5% to 10%, while those due to the Monte Carlo statistic was within 2%.

Figs. 4.7(a) and 4.7(b) are the results of the simulations (neutron energy spectra with statistical uncertainties) carried out for positions corresponding to those at which measurements were carried out. Each spectrum was normalized to per single incident neutron per MeV. Fig 4.7(a) shows the results at depths along the beam axis in the

phantom indicating that the flux diminishes with increasing depth. This trend is in keeping with expectations based on the fact that the beam becomes more diffuse as it progress through the water due to neutrons scattering out of the beam. However, the proportion of high energy to low energy neutrons in the spectra increases i.e. the spectra "harden" with increasing depth as expected (see section 3.4).

Fig 4.7(b) shows the spectra for positions off the beam axis. Since the detector was predominantly illuminated by neutrons that come directly from the source at the position (8 cm, 2 cm) the features of the spectrum are also most identical to those shown for the position (8 cm, 0 cm). However, the remaining 2 spectra at positions (8 cm, 4 cm) and (8 cm, 7.5 cm) are different in shape since the detector is only illuminated by scattered neutrons at these positions. Both spectra show reduced intensity due to lower beam flux. At (8 cm, 4 cm) the neutron peak at 64 MeV is significantly reduced while at (8 cm, 7.5 cm) the peak is almost absent. The spectrum at position (20 cm, 4 cm) shows a higher proportion of high energy neutrons than at position (8 cm, 4 cm) above 30 MeV due to the kinematics.

Another indication of the consistency of the results was comparing the proportion of high energy neutrons to low energy neutrons in the spectra. This was done by estimating the fraction of neutrons in the peak region N_{peak} (56.42 to 65.89 MeV) and the fraction of neutrons in the tail region N_{tail} (5.36 to 56.42 MeV) and then calculating the ratio N_{peak} to N_{tail} as shown in (Table 4.2). The statistical uncertainties for the ratios in table 4.2 were calculated as outlined in section 3.4. The results show consistent behaviour as expected. Thus, the ratio increases with increasing depth along the beam axis i.e. the spectra harden as discussed previously in section 3.4 and the ratio at (8 cm, 2cm) is similar to the ratio at (8 cm, 0 cm). The ratios at (8 cm, 4 cm) and (8 cm, 7.5 cm) show low proportions of high energy neutrons while at (20 cm, 4 cm) the percentage is higher.

A detailed comparison between the results from the simulations and the experimental measurements are discussed in Chapter 5.

Table 4.2 *Ratio of fractional count in peak N_{peak} to fractional count in tail N_{tail} calculated from the simulated spectra as a function of position in the phantom.*

Positions (d, r) cm	Ratio $(\frac{N_{peak}}{N_{tail}})$
(6, 0)	1.31 ± 0.25
(8, 0)	1.39 ± 0.26
(20, 0)	1.91 ± 0.35
(30, 0)	2.33 ± 0.43
(40, 0)	2.68 ± 0.50
(8, 2)	1.29 ± 0.24
(8, 4)	0.29 ± 0.05
(8, 7.5)	0.013 ± 0.002
(20, 4)	0.60 ± 0.10

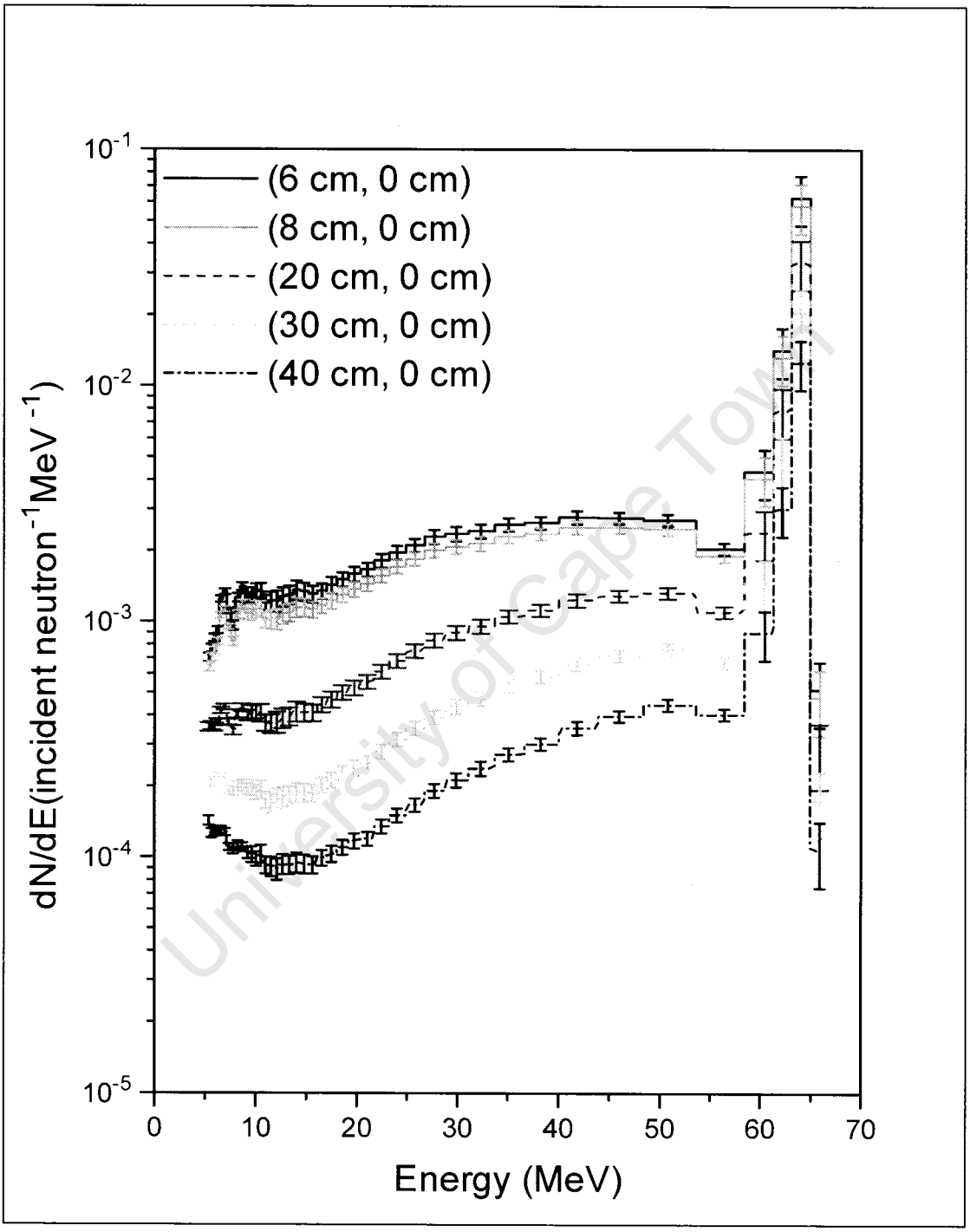

Fig. 4.7*(a) Simulated neutron energy spectra (per incident neutron) at different positions along the beam axis in the phantom.*

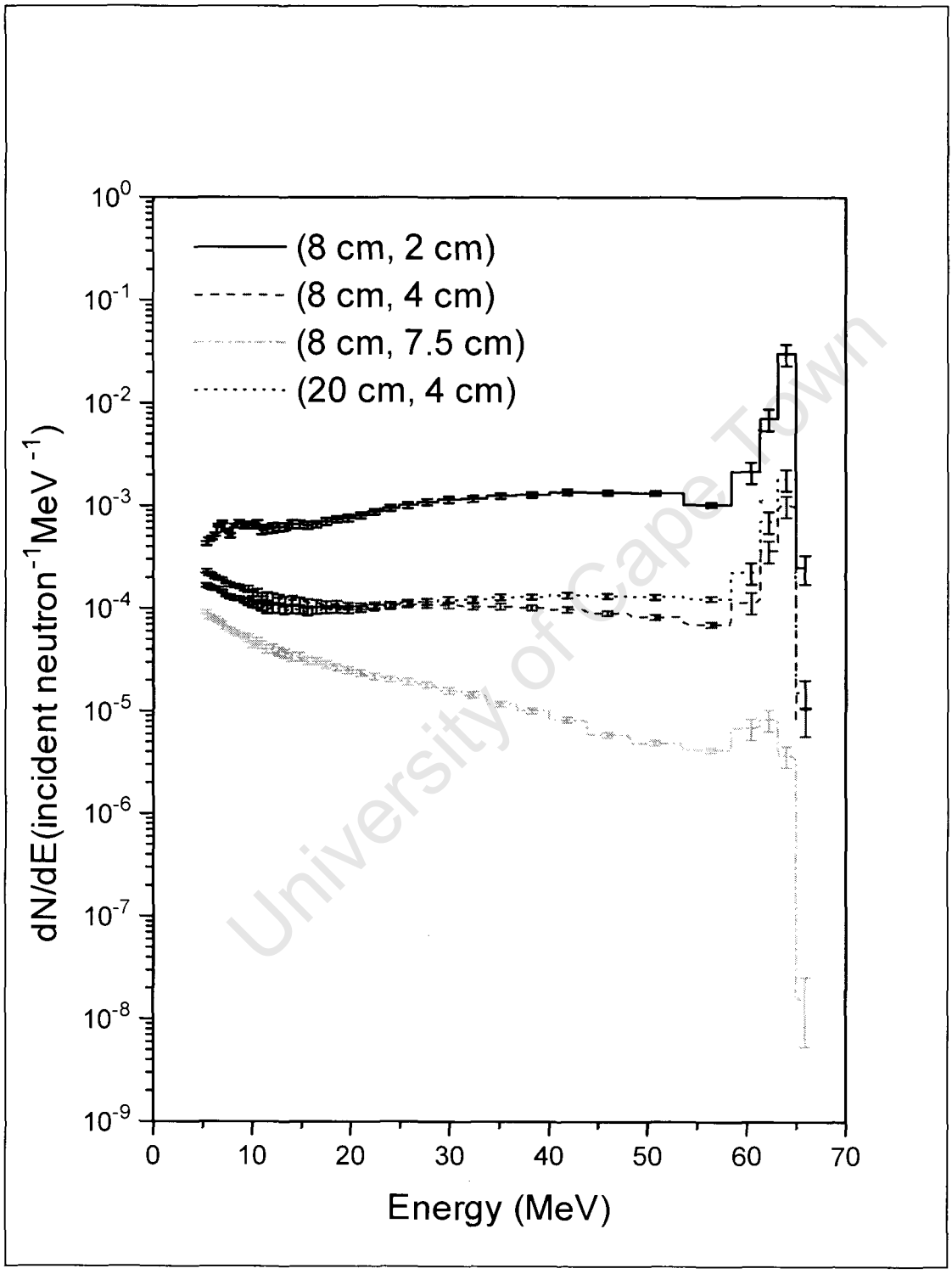

Fig. 4.7*(b) Simulated neutron energy spectra (per incident neutron) at different positions off the beam axis in the phantom.*

CHAPTER 5

DISCUSSION AND CONCLUSIONS

5.1 Comparisons between the results from experiment and Monte Carlo calculations for the in phantom neutron energy spectra.

The neutron energy spectra measured in the water phantom (section 3.4) are here compared with the predictions from Monte Carlo calculations (section 4.3.2). In each case shown below, the calculated and measured neutron energy spectrum is normalized to the same number of neutrons measured by the neutron monitor per MeV. The histograms indicate the measurements obtained from unfolding using MAXED while the solid circles are the results from the MCNPX Monte Carlo code (figs. 5.1(a)-(e), 5.3(a)-(d) and 5.5(a)-(b)). The error bars shown in the spectra are the statistical uncertainties associated with the measurements (see section 3.4) and the calculations (see section 4.3). To facilitate more detailed comparison, the ratios of the calculated energy spectra to the measured spectra are also presented (Table 5.1 and figs. 5.2(a)-(c) and 5.4(a)-(b)). The statistical uncertainties for the ratios in table 5.1 were calculated as outlined in section 3.4 and are shown in figs 5.2(b)-(c) and 5.4(b).

5.1.1 Neutron energy spectra along the beam axis

Figs. 5.1(a)-(e) show energy spectra at five positions in the water phantom along the beam axis, namely, 6 cm, 8 cm, 20 cm, 30 cm and 40 cm from the front face of the phantom. At the shallowest position, i.e. 6 cm into the water along the beam axis, it can be seen that above about 8 MeV there is good overall agreement between calculation and experiment. Based on the ratios shown in Table 5.1 and figs. 5.2(a)-(c) the agreement is within 5% from above 9 MeV up to the maximum energy. Below about 6.5 MeV the measured spectrum shows a sharp drop in intensity which is consistent with the electronic threshold of the experiment of about 5 MeV (section 2.4). Similar trends are observed at the 8 cm and 20 cm positions (figs. 5.1(b) and 5.1(c)) although the overall agreement is somewhat lower at 10%. The resonance structure around 7.4 MeV, attributed to resonances of ^{12}C associated with the 6.5 cm

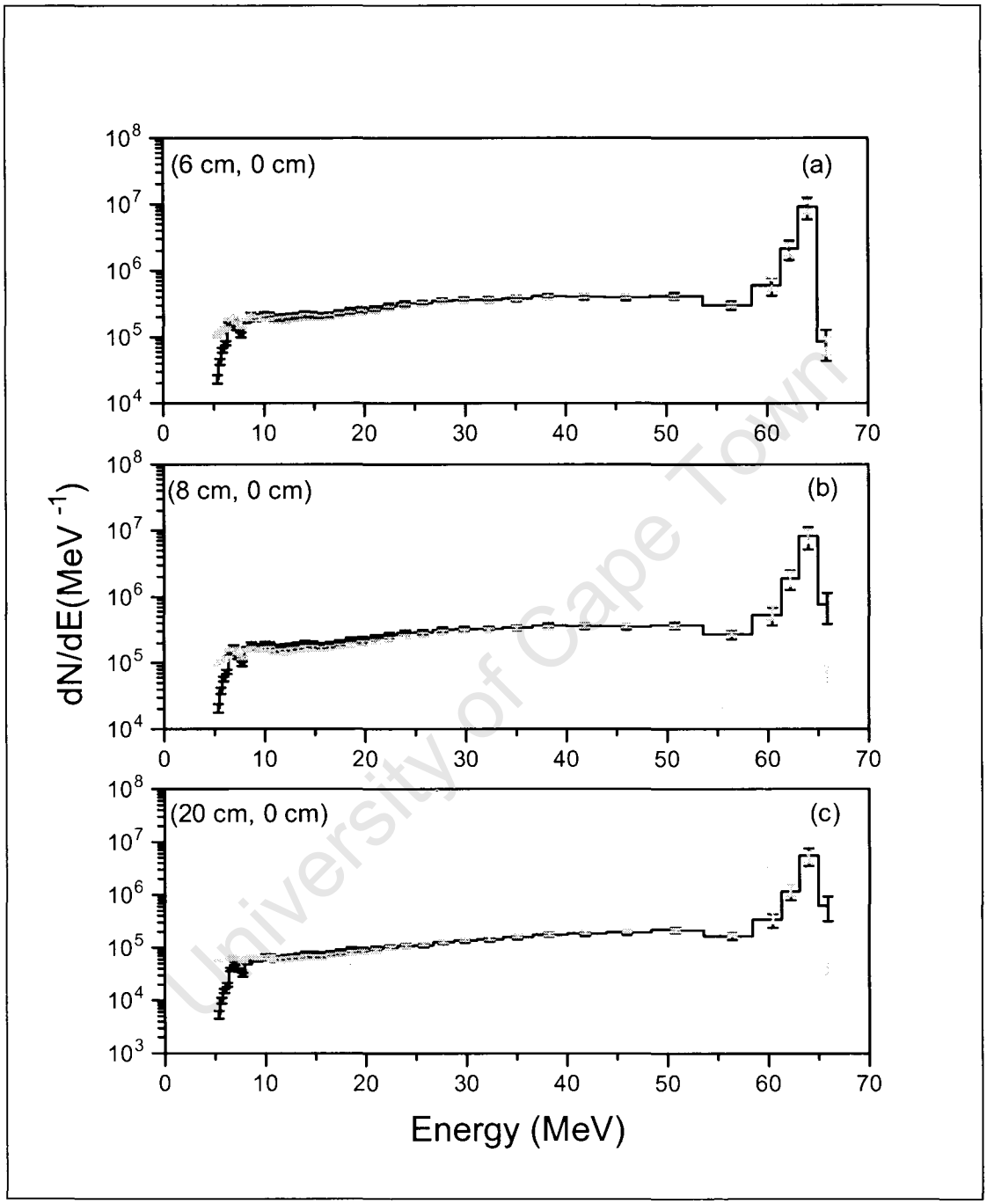

Fig 5.1(a)-(c) *Measured neutron energy spectra (histograms) compared with Monte Carlo results (solid circles) at depths of 6 cm, 8 cm and 20 cm along the beam axis in the phantom.*

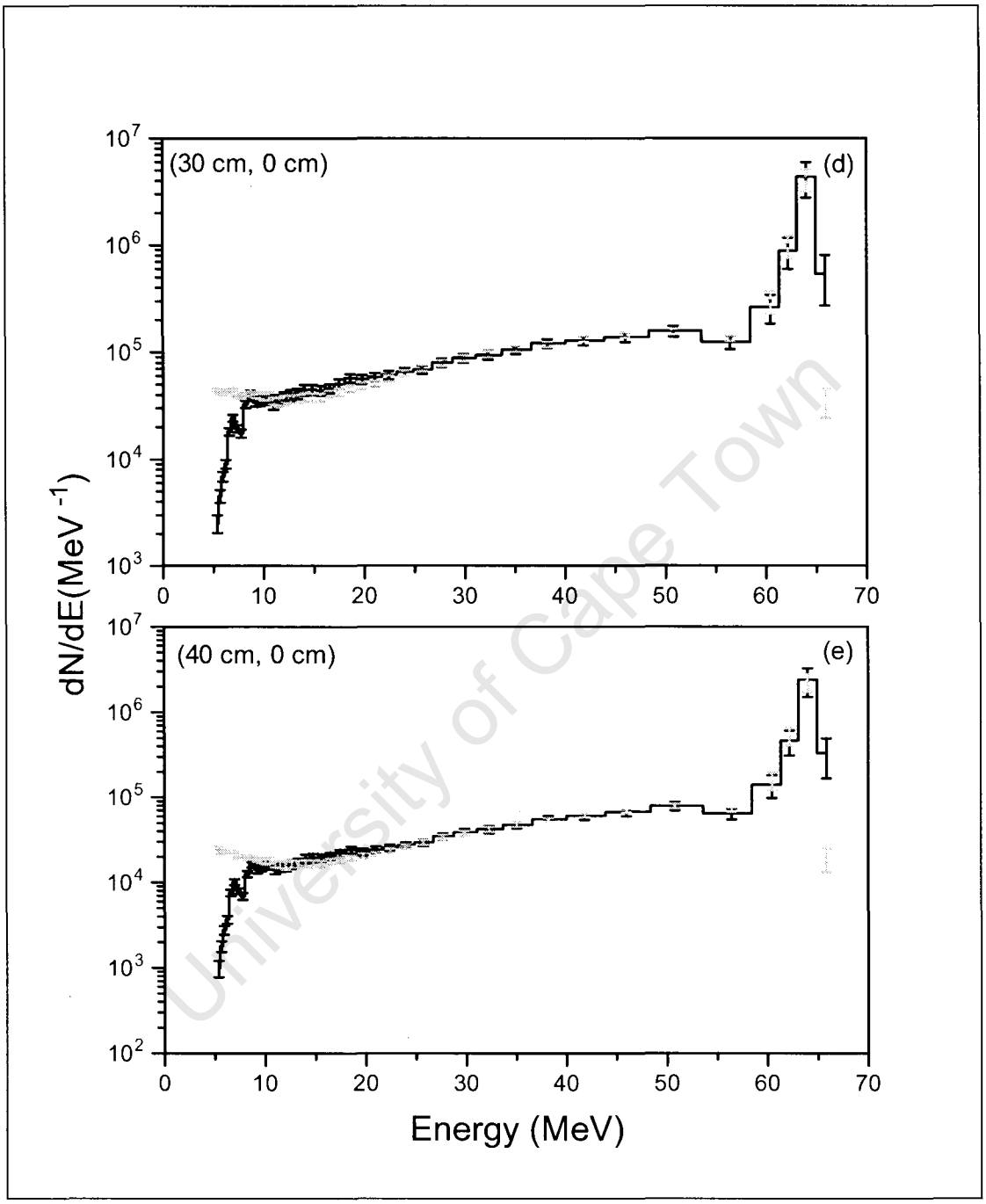

Fig 5.1(d)-(e) *Measured neutron energy spectra (histograms) compared with Monte Carlo results (solid circles) at depths of 30 cm and 40 cm along the beam axis in the phantom.*

Table 5.1 *Ratios of calculated (Monte Carlo) energy spectra to measured spectra at positions in the water phantom where d is the depth in cm along beam axis and r is the lateral distance in cm from the beam axis.*

Energy (MeV)	Ratios calculated at the indicated positions (d, r) cm into the water phantom								
	(6, 0)	(8,0)	(20,0)	(30,0)	(40,0)	(8,2)	(8,4)	(8,7.5)	(20,4)
5.36	4.51	4.47	10.49	17.66	25.63	5.59	3.44	16.56	10.91
5.63	2.70	2.71	5.86	9.32	12.49	3.35	2.16	7.93	6.29
5.92	1.99	1.91	3.78	5.98	8.21	2.30	2.05	5.28	4.62
6.23	1.68	1.64	3.04	4.73	6.24	1.95	2.47	4.26	4.30
6.56	1.20	1.11	1.72	2.44	3.06	1.26	1.82	2.18	2.60
6.93	1.04	0.95	1.38	1.85	2.24	1.09	1.38	1.82	1.93
7.32	1.20	1.12	1.59	1.99	2.46	1.27	1.23	2.26	2.13
7.75	1.33	1.24	1.81	2.21	2.81	1.43	1.03	2.61	2.27
8.22	1.05	0.97	1.22	1.24	1.58	1.08	0.65	1.60	1.29
8.65	0.96	0.89	1.03	1.02	1.21	0.97	0.88	1.50	1.23
9.20	1.00	0.93	1.08	1.15	1.31	1.01	0.99	1.86	1.44
9.60	0.96	0.89	1.03	1.14	1.21	0.98	0.88	1.62	1.32
10.03	0.93	0.86	0.95	1.03	1.07	0.90	0.67	1.26	1.12
10.49	0.95	0.87	0.97	1.08	1.15	0.96	0.77	1.26	1.22
10.97	0.97	0.90	1.00	1.09	1.17	0.95	0.78	1.23	1.36
11.50	0.93	0.85	0.93	0.95	1.08	0.92	0.69	1.24	1.13
12.06	0.92	0.85	0.93	0.95	1.02	0.93	0.79	1.50	1.10
12.67	0.94	0.86	0.92	0.92	1.01	0.93	1.35	1.50	1.15
13.32	0.93	0.85	0.90	0.89	0.95	0.91	0.99	1.25	1.39
14.02	0.91	0.84	0.88	0.86	0.88	0.91	0.78	1.12	1.50
14.78	0.92	0.86	0.86	0.84	0.85	0.92	0.60	1.18	1.50
15.61	0.94	0.88	0.88	0.86	0.84	0.95	1.12	1.40	1.33
16.51	0.94	0.89	0.91	0.89	0.86	0.95	1.41	1.30	1.19
17.49	0.94	0.88	0.89	0.84	0.83	0.94	0.97	1.53	1.02
18.56	0.89	0.84	0.86	0.80	0.81	0.89	0.68	1.16	0.96
19.73	0.93	0.88	0.93	0.87	0.90	0.91	0.76	1.00	1.04
21.02	0.91	0.87	0.94	0.86	0.87	0.90	0.83	1.02	1.01
22.43	0.92	0.87	0.97	0.93	0.93	0.90	0.76	0.94	0.99
24.00	0.91	0.87	1.00	0.98	0.97	0.90	0.87	0.74	0.92
25.75	0.97	0.93	1.06	1.04	1.01	0.95	0.86	0.70	0.98
27.69	0.97	0.93	1.04	0.99	0.98	0.94	0.84	0.76	0.93
29.87	0.97	0.94	1.04	1.00	0.98	0.97	0.94	0.81	0.99
32.31	0.99	0.96	1.05	1.02	1.01	0.98	0.81	0.80	1.02
35.08	1.01	0.99	1.06	1.03	1.03	1.00	0.86	0.72	1.02
38.23	0.96	0.94	1.00	0.98	0.97	0.95	0.92	0.62	1.00
41.83	1.02	1.01	1.07	1.04	1.04	1.02	0.82	0.74	1.09
45.97	1.03	1.03	1.06	1.05	1.05	1.03	0.83	0.66	1.07
50.78	0.97	0.98	0.99	0.99	1.00	0.98	0.67	0.51	1.00
56.42	1.01	1.03	1.07	1.09	1.12	1.04	1.51	1.14	1.51
60.44	1.09	1.11	1.12	1.13	1.14	1.10	2.33	1.33	1.47
62.18	0.99	1.02	1.07	1.12	1.16	1.01	1.74	0.43	1.25
63.99	1.01	1.03	0.96	0.95	0.94	1.00	1.19	0.07	0.74
65.89	0.89	0.91	0.07	0.07	0.06	0.89	0.02	0.01	0.04

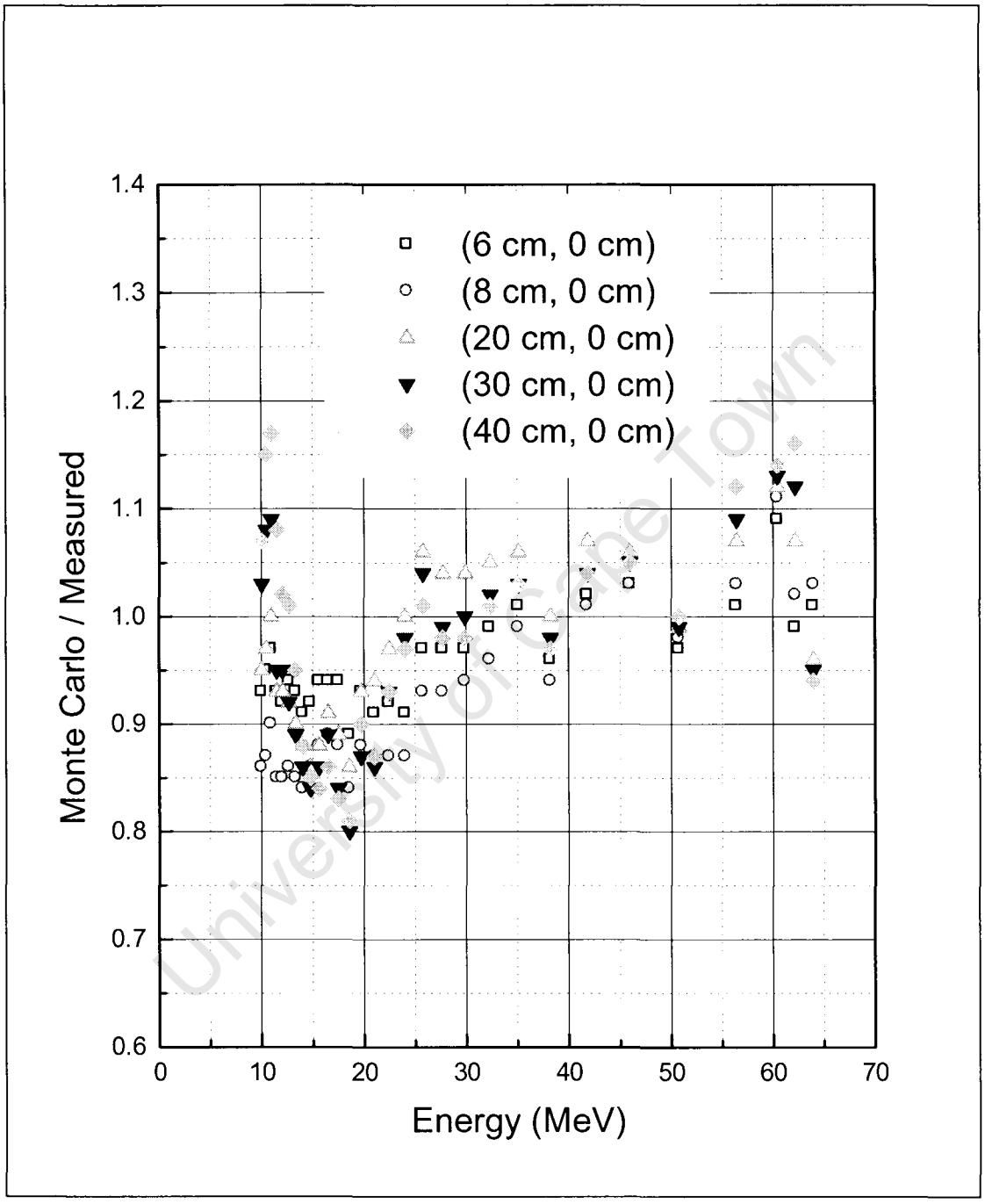

Fig. 5.2(a) *Ratios of the calculated (Monte Carlo) energy spectra to the measured spectra for different positions along the beam axis in the phantom. (The results are shown from 10 MeV upward for clarity of display (see table 5.1).*

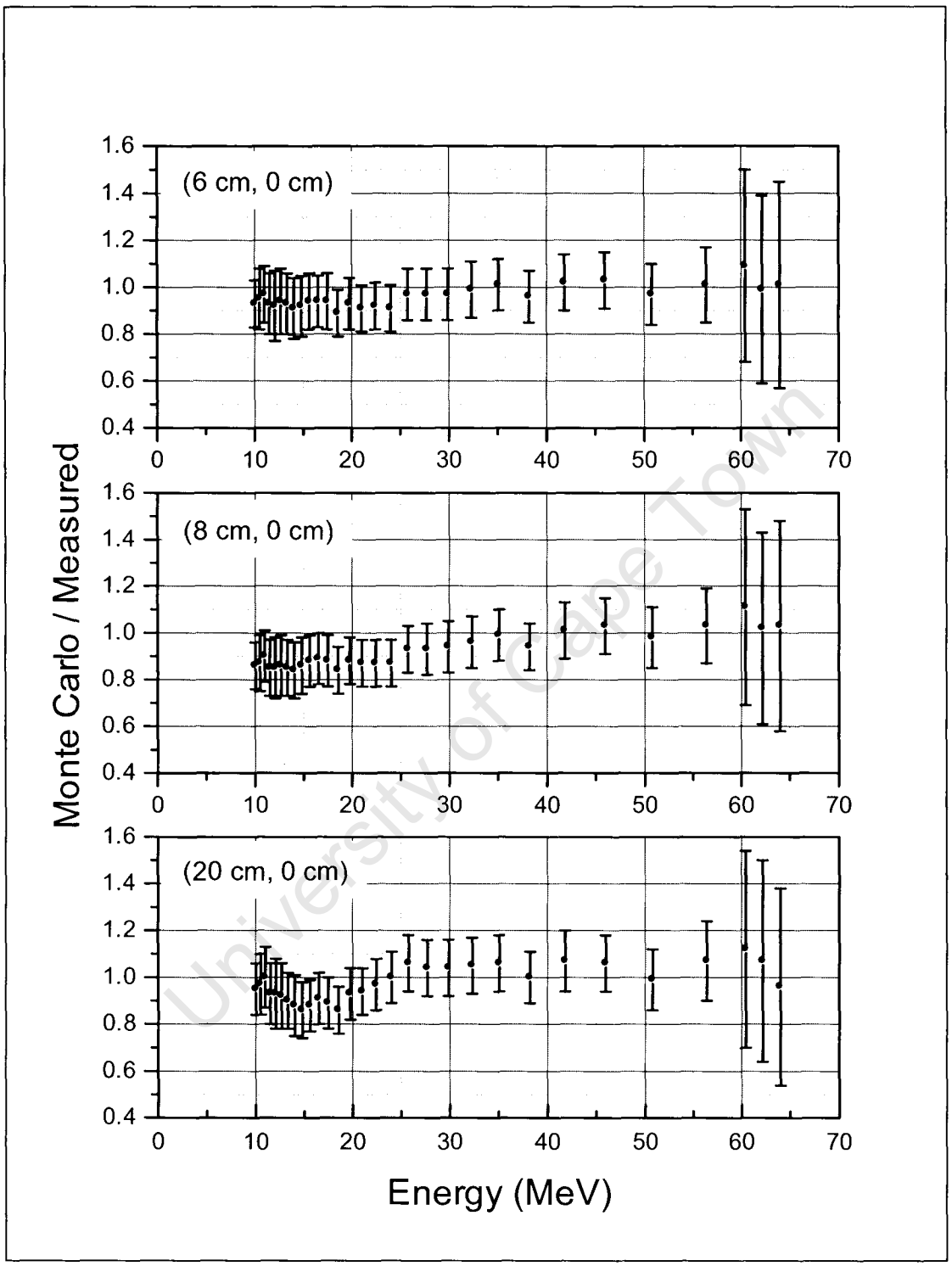

Fig. 5.2(b) *Ratios and associated statistical uncertainties of the calculated (Monte Carlo) energy spectra to the measured spectra at depths 6 cm, 8 cm and 20 cm along the beam axis in the phantom . (The results are shown from 10 MeV upward for clarity of display (see table 5.1).*

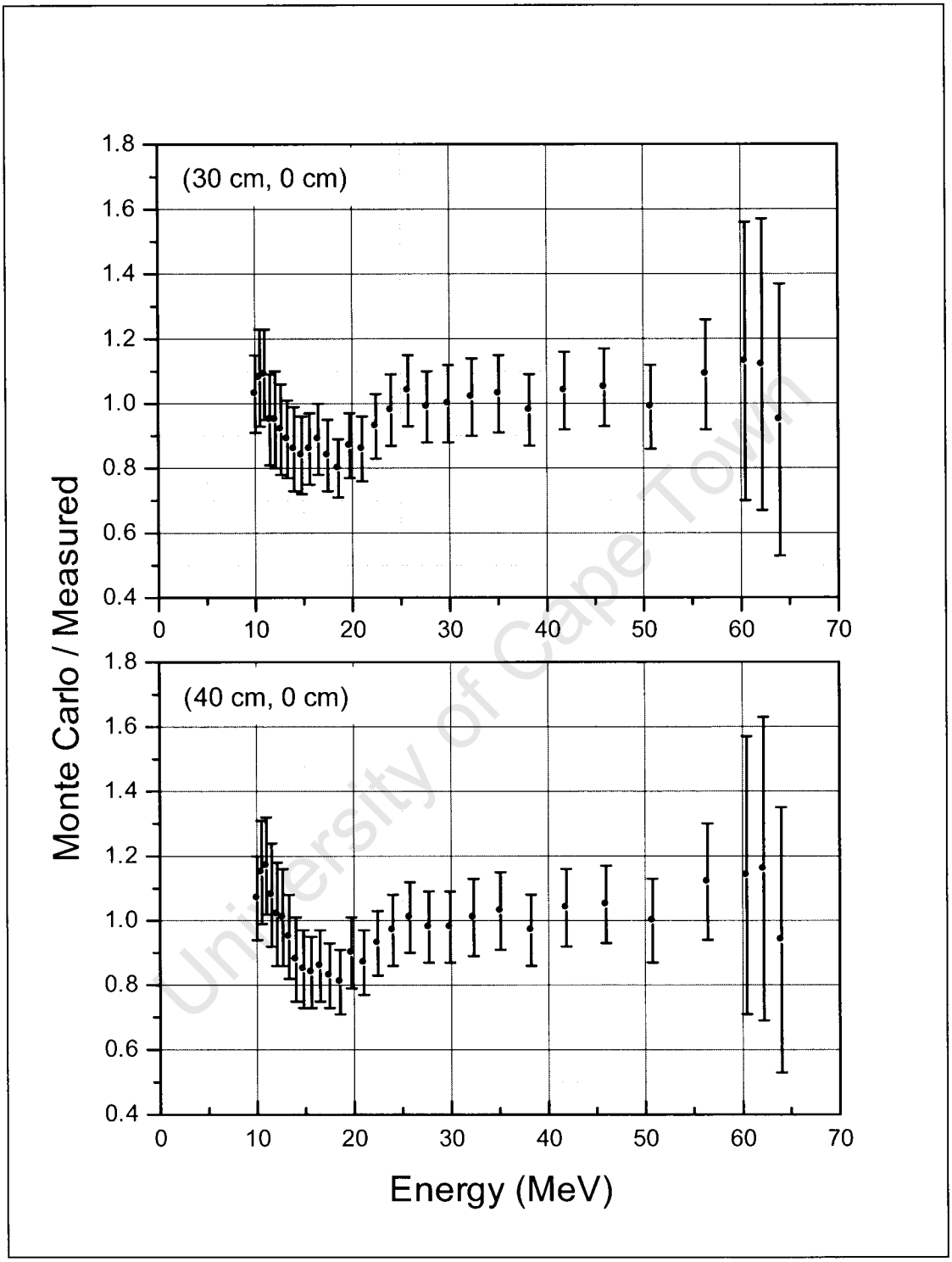

Fig. 5.2(c) *Ratios and associated statistical uncertainties of the calculated (Monte Carlo) energy spectra to the measured spectra at depths 30 cm and 40 cm along the beam axis in the phantom . (The results are shown from 10 MeV upward for clarity of display (see table 5.1).*

thick graphite block put in front of the collimator side facing the target (see section 2.1) can clearly be seen in both the measured and calculated spectra at all three depths. At the deepest positions within the phantom (30 cm and 40 cm) the differences between the spectra remain within about 10% at energies above about 12 MeV. However, the level of agreement becomes progressively worse below this energy as can be seen from figs. 5.2(a)-(c)

In particular, at 30 cm and 40 cm, there is a large disagreement with regard to the resonance at 7.4 MeV. The Monte Carlo calculations indicate that the resonance has faded out while the measurements show a "dip" in structure. The apparent strength of the resonance in the measured spectra is attributed to an artefact associated with the unfolding procedure in that MAXED applies no smoothing routines and preserves any structure in the prior spectrum that is finer than the energy resolution of the detector [Go02]. On the other hand, the Monte Carlo calculations are in keeping with the expectation that the resonance structure will fade out with increasing depth in the phantom due to scattering.

5.1.2 Neutron energy spectra off the beam axis

Fig 5.3(a)-(d) shows results of both measured and calculated spectra at positions that are off the beam axis. The first three panels (a)-(c) show measured spectra (histograms) and calculated spectra (open circles) at the same depth of 8 cm while the lateral distances are 2 cm, 4 cm and 7.5 cm as indicated. Table 5.2 and fig. 5.4(a)-(b) show that at the position closest to the beam axis (2 cm) the agreement between the measured and calculated spectra agree to within 10%. The neutron peak at 64 MeV and the resonance structure around 7.4 MeV are also well reproduced in both the calculated spectrum and measured spectra. Overall, the results at 2 cm away from the axis are similar to the on-axis results obtained at the same depth (8 cm).

However, agreement between the measurements and the calculations becomes progressively worse further from the axis, i.e. the agreement at 7.5 cm is substantially worse than at 4 cm as can be seen in fig. 5.4(a)-(b). For example, at the position (8 cm, 4 cm) the disagreement between the calculated and measured energy spectra above 20 MeV is more than 10% rising to over 50% above 55 MeV. It is interesting to note, however, that at position (20 cm, 4 cm) which is substantially further into the

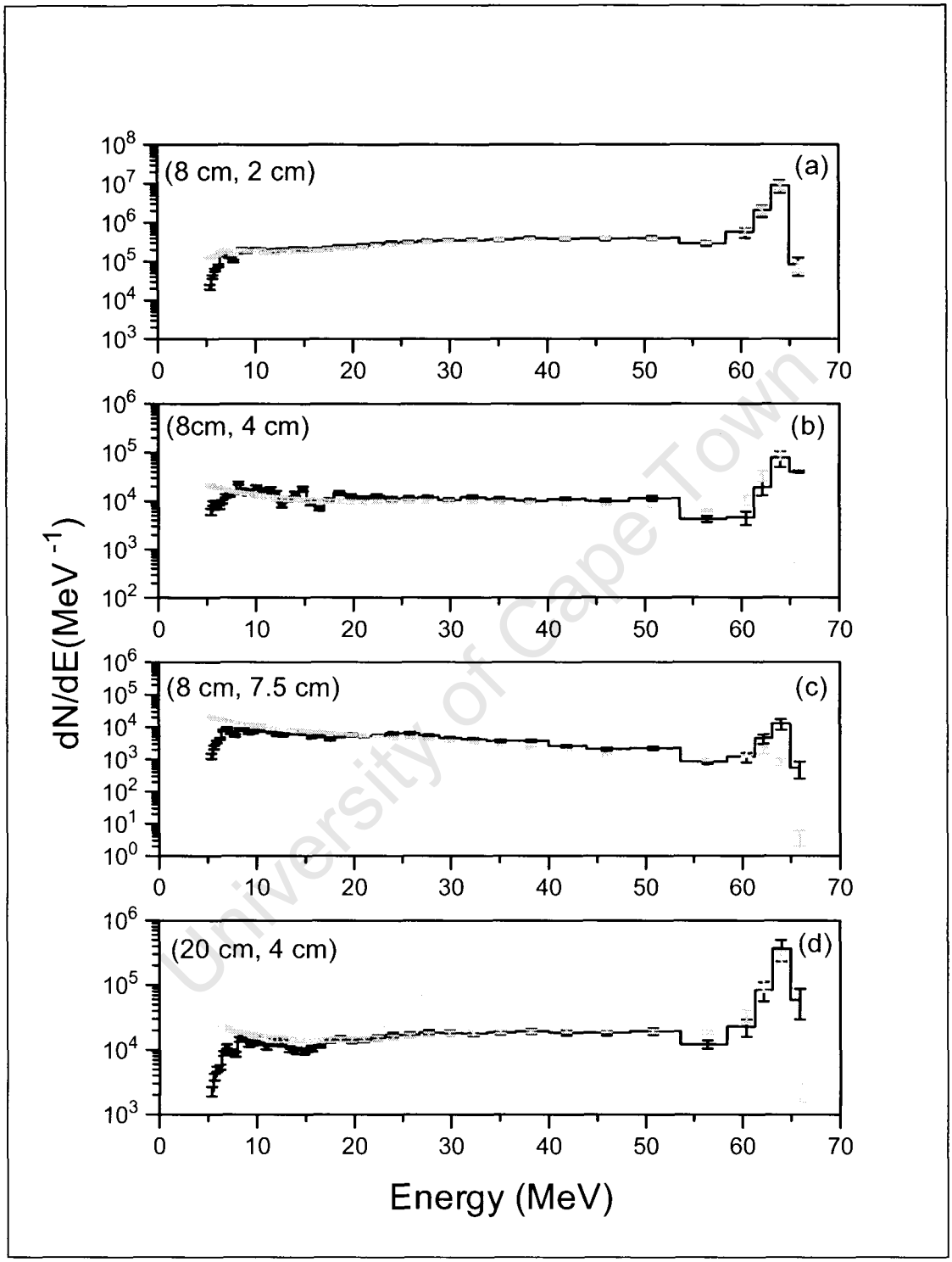

Fig. 5.3(a)-(d) *Measured neutron energy spectra (histograms) compared with Monte Carlo results solid circles) at off beam axis positions (2 cm, 4 cm and 7.5 cm) in the phantom.*

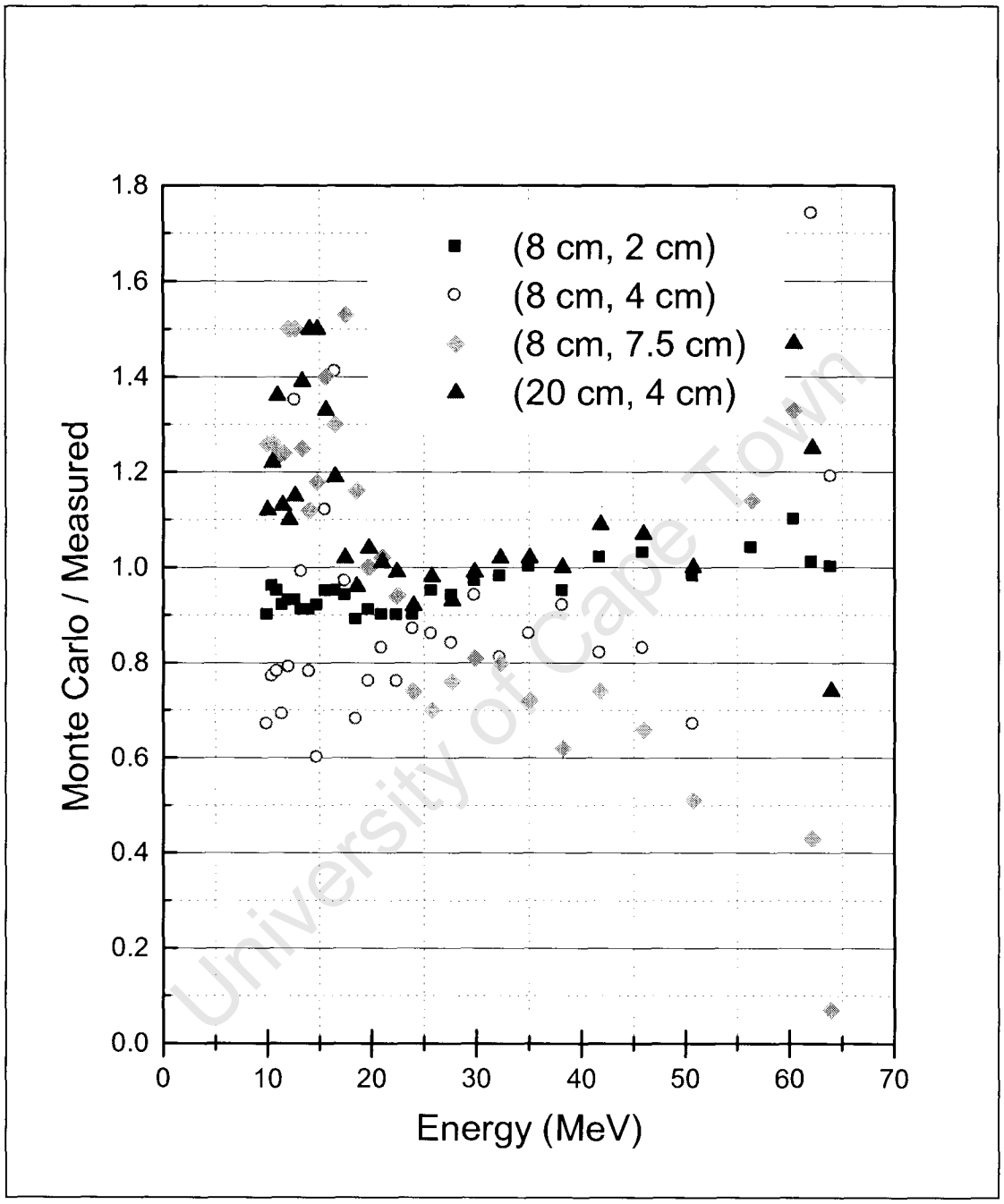

Fig. 5.4(a) *Ratios of the calculated (Monte Carlo) energy spectra to the measured spectra for different positions off the beam axis in the phantom. (The results are shown from 10 MeV upward for clarity of display (see table 5.1.).*

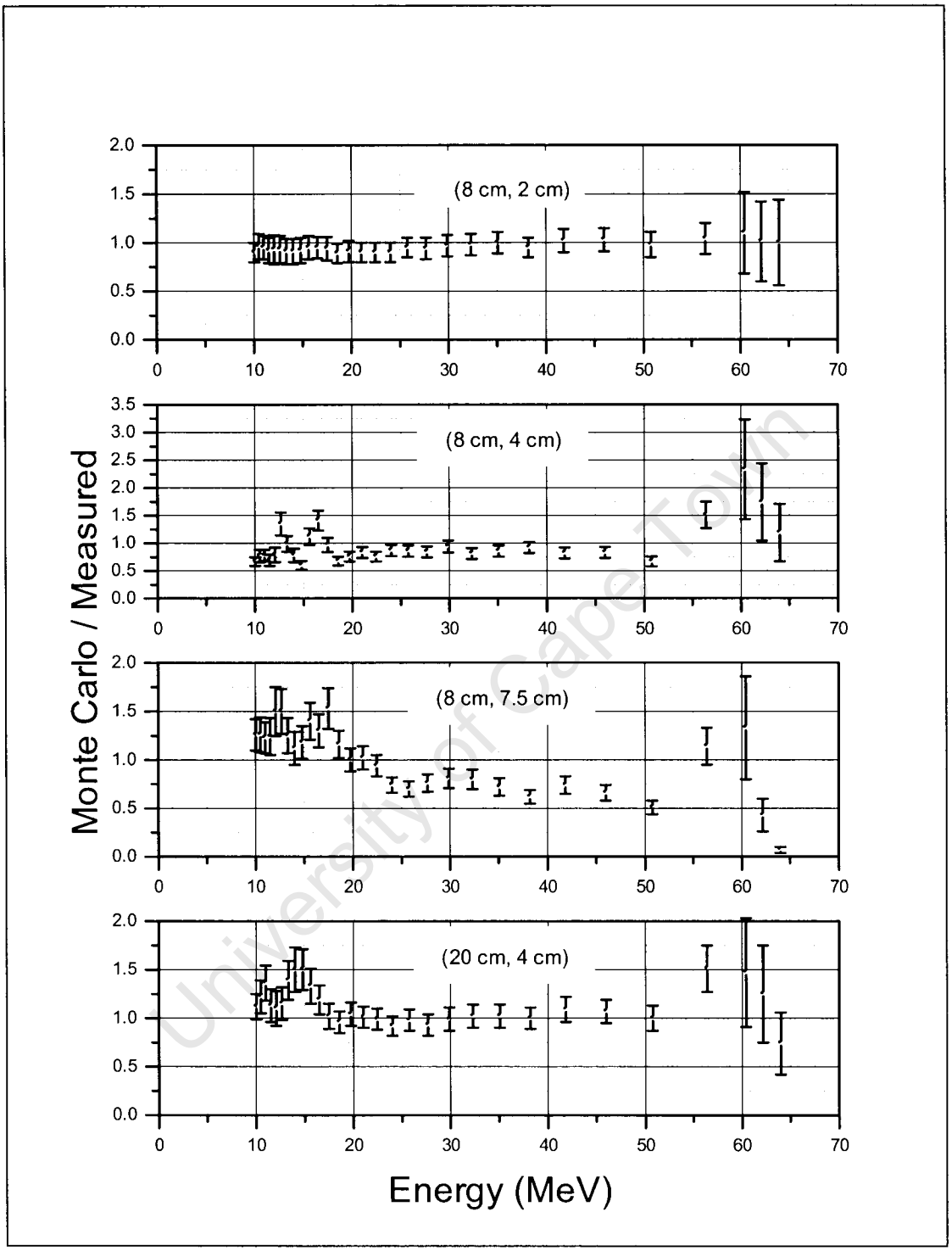

Fig. 5.4(b) *Ratios and associated statistical uncertainties of the calculated (Monte Carlo) energy spectra to the measured spectra at off beam axis positions (2 cm, 4 cm and 7.5 cm) in the phantom. (The results are shown from 10 MeV upward for clarity of display (see table 5.1).*

phantom, the measured and calculate spectra agree to within 10% over the same energy range (20-55 MeV). It is possible that the differences between the Monte Carlo results and the measurements arise due to the unfolding procedure insofar as using the Li spectrum as the prior concerned. At the positions where agreement is worst the detector is situated out of the path of the neutrons that arise directly from the target. In these cases the neutrons that enter the detector do so after having been scattered. Thus, the spectra are not likely to have a strong peak around 64 MeV. Using the Li spectrum is therefore likely to give results that overestimate the strength of the 64 MeV peak in the same way as discussed in section 3.3. This is in keeping with the fact that the agreement between the calculations and the measurements are better at position (20 cm, 4 cm) than at (8 cm, 4 cm) since the former position lies in a more forward direction that the latter. With regard to the poor agreement between the calculations and the measurements around the region of the 7.4 MeV resonances, the dip in the measured spectra is attributed to an artefact of the unfolding procedure as discussed previously in 5.1.1.

5.2 Conclusions and further work

A neutron spectrometer based on a deuterated organic liquid scintillator (NE230) has been developed for measuring neutron spectra in water. The spectrometer is capable of measuring energies above 5 MeV, set by the electronic threshold. One of the important features of the spectrometer is that it is able to discriminate between particles arising from neutron interactions in the detector from recoiling protons that arise from n-p scattering in the water. The spectrometer was tested by measuring pulse height spectra in a water phantom irradiated by neutrons of energy up to ~ 64 MeV. The neutron energy spectra were obtained from the measurements of the pulse height spectra by Bayesian unfolding. One of the novel features of this process was that the response matrix required by the unfolding code MAXED was determined experimentally rather than by Monte Carlo calculation. (As pointed out in Chapter 1 a limitation on the accuracy of such Monte Carlo calculations is that the cross-sections are not well known at the energies above about 20 MeV).

We distinguish between two different situations in the water phantom depending on the particular position of the detector in the phantom: (1) the detector was in the direct

path of the beam and was predominantly illuminated by neutrons that come directly from the source and (2) the detector was outside the direct path of the beam and was illuminated by neutrons that have previously undergone scattering. In the present work situation (1) was explored in detail by placing the detector along the beam axis while exploratory work was carried out in the case of situation (2).

The broad trends of the neutron energy spectra that were obtained after unfolding were, firstly, that the energy spectrum hardens with increasing depth in the phantom along the beam axis, and, secondly that the spectrum softens with increasing lateral distance from the beam axis. These results are consistent with other measurements that have been reported [Jo92, Bo82 and Cr91]. A comparison with Monte Carlo calculations using MCNPX showed good agreement (of the order of 10%) between the measurements and the calculations for the spectra along the beam axis. However, the spectra that were measured at positions off the beam axis, in particular, those in which the detector was situated out of the path of the neutrons that arise directly from the target did not agree well with the Monte Carlo calculations.

From the limited data taken for case (2) a number of issues are apparent, although a more systematic investigation remains to be undertaken. One possibility is that the Li prior spectrum used in the unfolding is not appropriate when the geometry is such that only scattered neutrons enter the detector since it is likely to be an overestimate of the strength of the 64 MeV neutron peak. A preliminary investigation was carried out using a flat prior to unfold the data taken at the positions (8 cm, 4 cm), (8 cm, 7.5 cm) and (20 cm, 4 cm). The results are shown in fig. 5.5 in which the dotted line indicates results from the unfolding using the flat prior. It is clear that at the position (8 cm, 4 cm) the flat prior appears to fare worse than the Li prior in that between 50 MeV and 60 MeV the results deviate systematically from both the Monte Carlo calculations and the results from the Li prior especially around the peak at 64 MeV . For the positions (8 cm, 7.5 cm) and (20 cm, 4 cm) there is also no evidence that a flat prior produces results that are in greater agreement with the Monte Carlo calculations. This points strongly to the possibility that the disagreements at these positions might lie in the choice of the prior spectrum used in the unfolding which requires a more detailed investigation. A more systematic set of measurements with good statistical accuracy are also required in order to understand the issues associated with unfolding

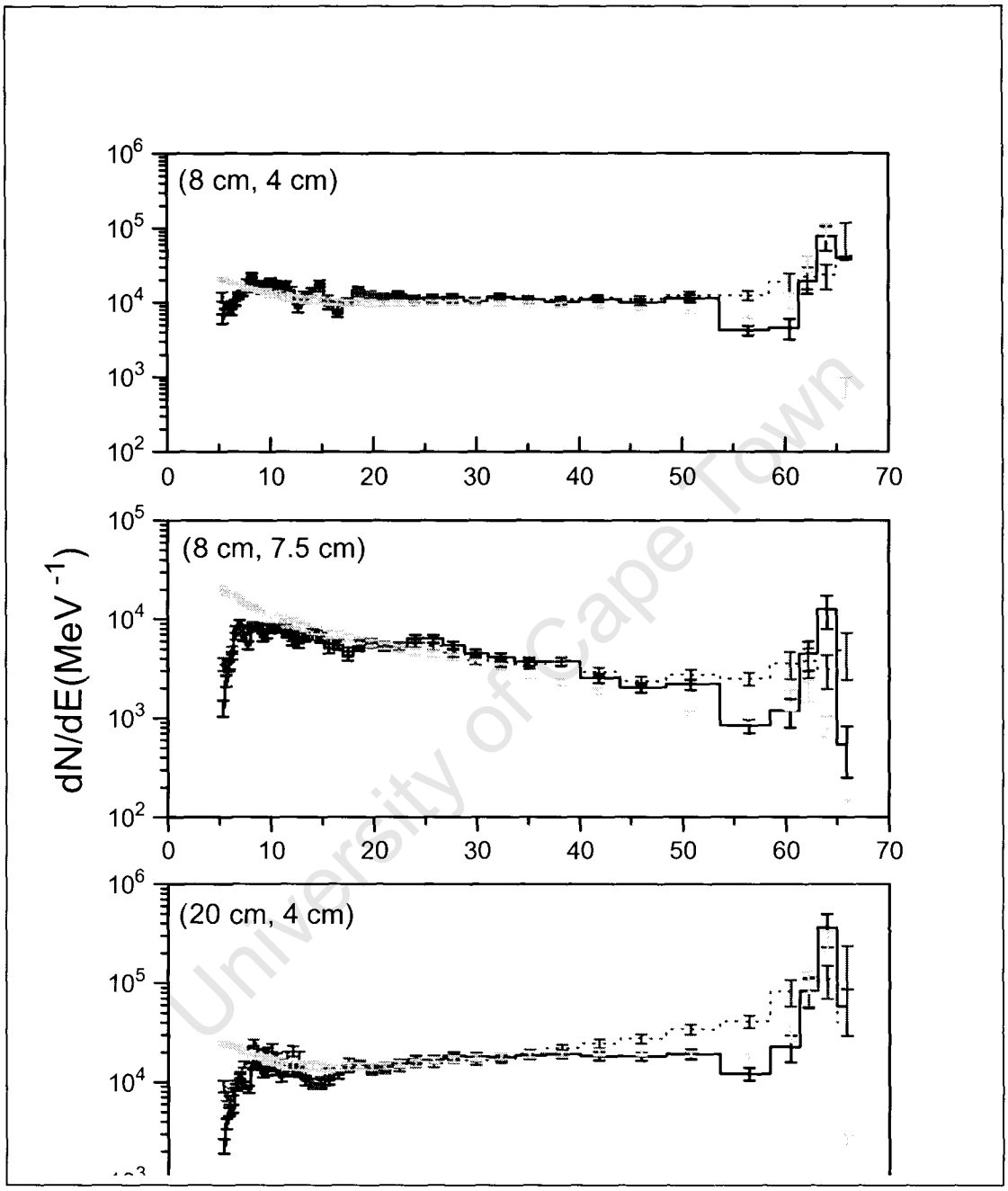

Fig. 5.5 *Comparison between measured neutron energy spectra obtained using Li prior (histograms), flat prior (dotted line) for unfolding and Monte Carlo results (solid circles) at off beam axis positions (8 cm,4 cm), (8cm, 7.5 cm) and (20 cm, 4 cm) in the phantom.*

of data at off-beam axis positions. In particular, this will allow one to explore the effect of either using different mixtures of the Li and flat spectra as well as using Monte Carlo calculations to generate spectra as prior input. The sensitivity of the response matrix could also be improved, in particular at neutron energies above 55 MeV where the sensitivity of the response matrix is lower due to forward recoil deuteron escapes.

The effectiveness of radiation therapy using fast neutron beams depends on the deposition of energy within body tissue and the biological effects these particles produce. Both the energy deposition and the biological effects are due to the recoil nuclei and charged particles the neutrons produced when they interact with body tissue as discussed in chapter 1. In order to calculate the absorbed dose, i.e. the energy deposited in body tissue by recoil nuclei and the charged particle, detailed knowledge of the energy spectrum of the neutrons as a function of position in the body tissue is require. The energy spectrum of the neutrons can either be calculated by Monte Carlo Methods or measured experimentally. As outlined previously in section 1.2 it is difficult to do either the calculations or measurements.

The only directly comparable study to the present work is that of Crout et al in which they used an NE213 cell (diam. 60 mm x 60 mm) to measure the energy spectrum of 10 to 60 MeV neutrons as a function of position in a water phantom. As discussed previously in section 1.3 a lead cap was used in their work to screen out protons from the water. The perturbing effect of the cap on the neutron energy spectra was investigated using Monte Carlo calculations and was calculated to be of the order of 15% [Cr91]. In the present work using deuterated liquid NE230 (diam. 25 mm x 25 mm) the recoil particle is a deuteron. Thus, the protons from the water do not add significant background to the measured pulse height spectra. This leads to the fact that a much smaller detector could be used thereby providing better spatial resolution.

The proportion of recoil particles that escape from the two detectors in question i.e. either protons from the NE213 (diam. 60 mm x 60 mm) or deuterons from the NE230 (diam. 25 mm x 25 mm), are compared as shown in columns 2 and 3, respectively, in Table 5.2. (See Appendix A for details). Thus, for example while at 10 MeV about 3% of particles escape at 50 MeV the fraction is almost to 15 times larger. Column 4

shows the fractions of recoil protons that would escape from a NE213 detector of the same dimensions as the NE230 detector used in the present work. Thus, comparing columns 2 and 4, it can be seen that already at 50 MeV 100% of recoiling protons will escape. It is clear from this perspective that there is a significant advantage to using the NE230 over NE213. It is also interesting to note that the effect of multiple scattering is reduced from 6% using NE213 (diam. 60 mm x 60 mm) to about 3% in the case of the NE230 (diam. 25 mm x 25 mm). Although this discussion indicates that the NE230 will in all like hood give better results than the NE213 for the measurements, a detail study along the lines described in the thesis needs to be carried out with NE213 in order to provide a more quantitative comparison.

Table 5.2 *Comparison of percentage recoil particles that escape from NE213(protons) and NE230 (deuterons) for different energies.*

Energy of recoil particles (MeV)	NE230 (% deuteron escapes)	NE 213 (% proton escapes)	
	Diam 25 mm x 25 mm	Diam 60 mm x 60 mm	Diam 25 mm x 25 mm
10	3	3	7
20	11	10	24
30	24	21	49
40	39	35	79
50	58	52	100
57*	71	65	100
64**	-----	78	100

* Maximum recoil deuteron energy for 64 MeV neutrons

** Maximum recoil proton energy for 64 MeV neutrons

Appendix A

Neutron detection efficiency

Determining the neutron energy spectra with the NE230 detector the neutron detection efficiency of the detector as a function of neutron energy is required. For this it is sufficient to use the relative detection efficiency of the detector as a function of neutron energy. In this work the neutron detection efficiency of the NE230 detector as a function of neutron energy was determined from the ratio of counts recorded by the NE230 and NE213 detectors respectively. The efficiency of the NE230 detector is given by the product of this ratio and the known detection efficiency of the NE213 detector, which was determined by reference to the n-p elastic scattering cross-section.

The efficiency $\varepsilon(E_n)$ of a neutron detector for detecting a neutron of a particular energy E_n is the probability of recording a pulse from a particle produced by the interaction of the neutron in the detector. Let's first consider the simple case, a beam of N_i mono-energetic neutrons of energy E_n incident on a slab detector of thickness t and N the number of pulses recorded above electronic threshold of the detector as shown in fig. A-1.

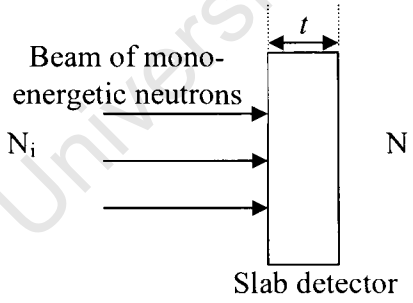

Fig. A-1 *A beam of mono-energetic neutrons of energy E_n incident on a slab detector.*

The neutron detection efficiency $\varepsilon(E_n)$ for the slab detector for detecting mono-energetic neutron of energy E_n is related to N_i and N by

$$\varepsilon(E_n) = \frac{N}{N_i}. \qquad (A.1)$$

The efficiency $\varepsilon(E_n)$ of the detector depends on the energy E_n of the incident mono-energetic neutrons, neutron reaction cross-section at E_n, thickness of the detector in the

direction of the incident mono-energetic neutrons, the electronic threshold of the detector and any other electronic selection, if applied.

Now consider the NE230 and NE213 detectors exposed to the same beam of mono-energetic neutrons of energy E_n in succession measurements, using equation A.1 we can write for the NE213 detector

$$N_H = \varepsilon_H(E_n, L_H)N_o \tag{A.2}$$

where, N_o is the number of mono-energetic neutrons of energy E_n incident on the NE213, N_H is the number of proton and heavier charged particle events induced by the mono-energetic neutrons in the pulse height spectrum measured by the detector above the pulse height threshold, L_H (see fig. A-2) and $\varepsilon_H(E_n, L_H)$ the efficiency of the NE213 detector for detecting neutrons of energy E_n above the pulse height threshold L_H. The efficiency $\varepsilon_H(E_n, L_H)$ can be calculated from the n-p elastic scattering cross-sections and the detector properties as follows: We set L_H to a value L_{np} which selects only the n-p elastic scattering cross-sections events, indicated by N_{np} as shown in fig. A2. Thus equation A.2 becomes

$$N_{np} = \varepsilon_H(E_n, L_{np})N_o \tag{A.3}$$

For the energy considered the efficiency $\varepsilon_H(E_n, L_{np})$ can be calculated by

$$\varepsilon_H(E_n, L_{np}) = \phi_{npf}(E_n, L_{np})\sigma_{np}(E_n)n_H \tag{A.4}$$

where:

$\phi_{npf}(E_n, L_{np})$: the fraction of mono-energetic neutrons of energy E_n detected above pulse height threshold L_{np} that undergo n-p elastic scattering only in the NE213 scintillator;

$\sigma_{np}(E_n)$: total cross-section for all n-p elastic scattering in the NE213 scintillator at energy E_n;

n_H: number of hydrogen nuclei per unit cross sectional area presented to the mono-energetic neutrons by the NE213 scintillator.

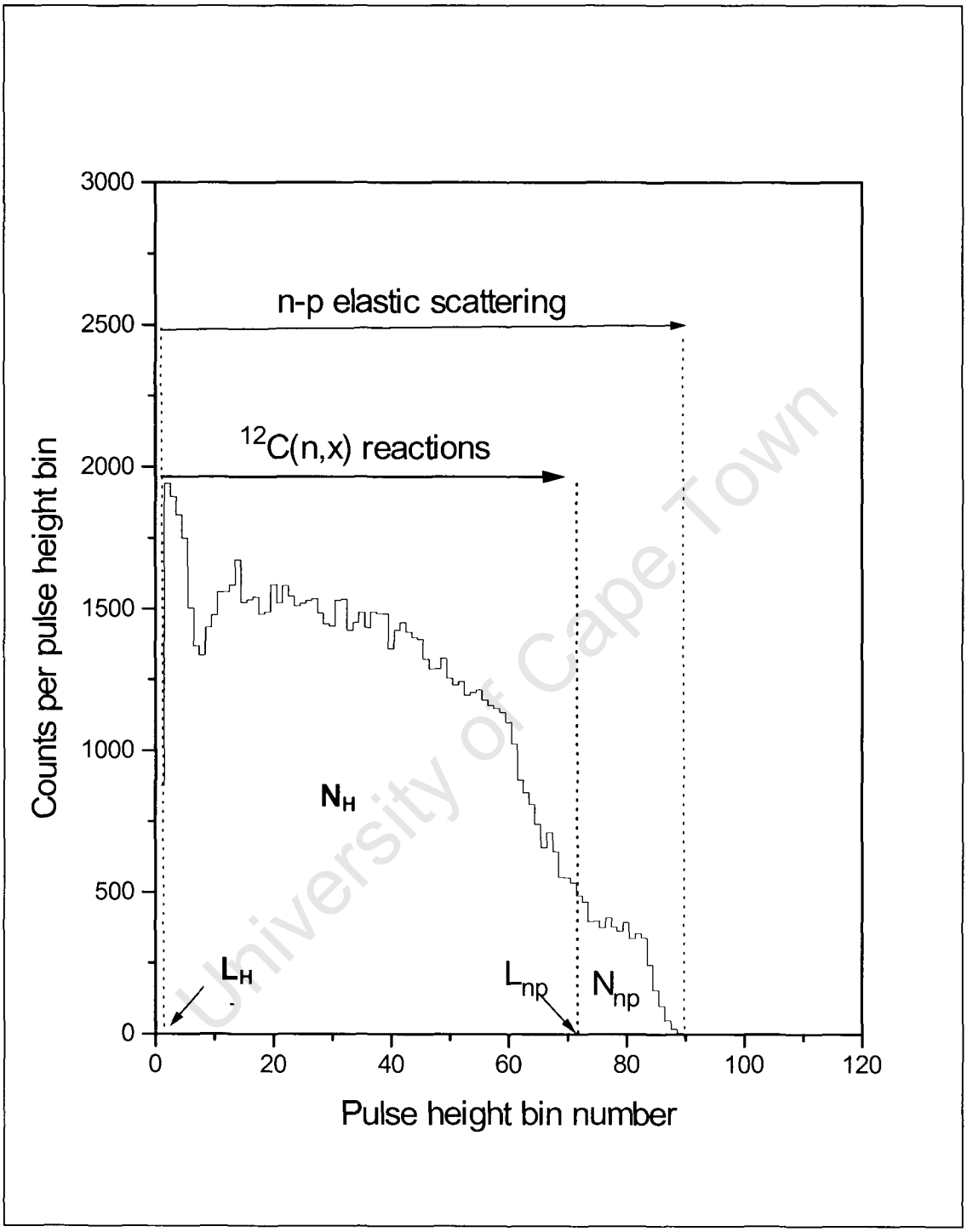

Fig. A-2 *Pulse height spectrum measured using the NE213 detector for incident neutrons of energy 64 MeV, with the PSD-cut (see section 2.5) set to select protons and heavier charged particles events.*

The factors $\phi_{npf}(E_n, L_{np}), \sigma_{np}(E_n)$ and n_H was determined from the total differential neutron cross-section data for hydrogen and from the properties of the detector. Combining equations A.3 and A.4 we can write

$$N_{np} = \phi_{npf}(E_n, L_{np})\sigma_{np}(E_n)n_H N_o \tag{A.5}$$

The right hand-side of equation A.5 is multiplied by a recoiling proton correction factor $\phi_{npe}(E_n, L_{np})$ which corrects for the fraction of recoiling protons which has pulse height above the pulse height threshold L_{np}, which escape from the detector before depositing all their energy in the detector. The factor $\phi_{npe}(E_n, L_{np})$ was determined from the stopping power data for protons. Equation A.5 then becomes

$$N_{np} = \phi_{npf}(E_n, L_{np})\phi_{npe}(E_n, L_{np})\sigma_{np}(E_n)n_H N_o \tag{A.6}$$

Using equation A.1 we can also write for the NE230 detector

$$N_D = \varepsilon_D(E_n, L_D)N_i \tag{A.7}$$

where, N_i is the number of mono-energetic neutrons of energy E_n incident on the NE230, N_D is the number of deuteron and heavier charged particle events induced by the mono-energetic neutrons in the pulse height spectrum measured by the detector above the pulse height threshold, L_D (see fig. A-3) and $\varepsilon_D(E_n, L_D)$ the efficiency of the NE230 detector for detecting neutrons of energy E_n above the pulse height threshold L_D. Combining equations A.6 and A.7 the efficiency $\varepsilon_D(E_n, L_D)$ of the NE230 detector was determined from the ratio $\frac{N_D}{N_{np}}$ and is given by

$$\varepsilon_D(E_n, L_D) = \frac{N_o N_D}{N_i N_{np}}\phi_{npf}(E_n, L_{np})\phi_{npe}(E_n.L_{np})\sigma_{np}(E_n)n_H \tag{A.8}$$

Normalizing N_o and N_i to the same number of monitor neutrons, equation A.8 becomes

$$\varepsilon_D(E_n, L_D) = \frac{M_o N_D}{M_i N_{np}}\phi_{npf}(E_n, L_{np})\phi_{npe}(E_n.L_{np})\sigma_{np}(E_n)n_H \tag{A.9}$$

where, M_i is the number of monitor neutrons recorded by the monitor during the measurement of N_i and M_o the monitor neutrons recorded during measurement N_o. Equation A.9 gives the efficiency $\varepsilon_D(E, L_D)$ of the NE230 detector for detecting mono-energetic neutron of energy E_n via n-p elastic scattering. Using equations A.9 the efficiency $\varepsilon_D(E, L_D)$ of the NE230 detector was determined as a function of neutron

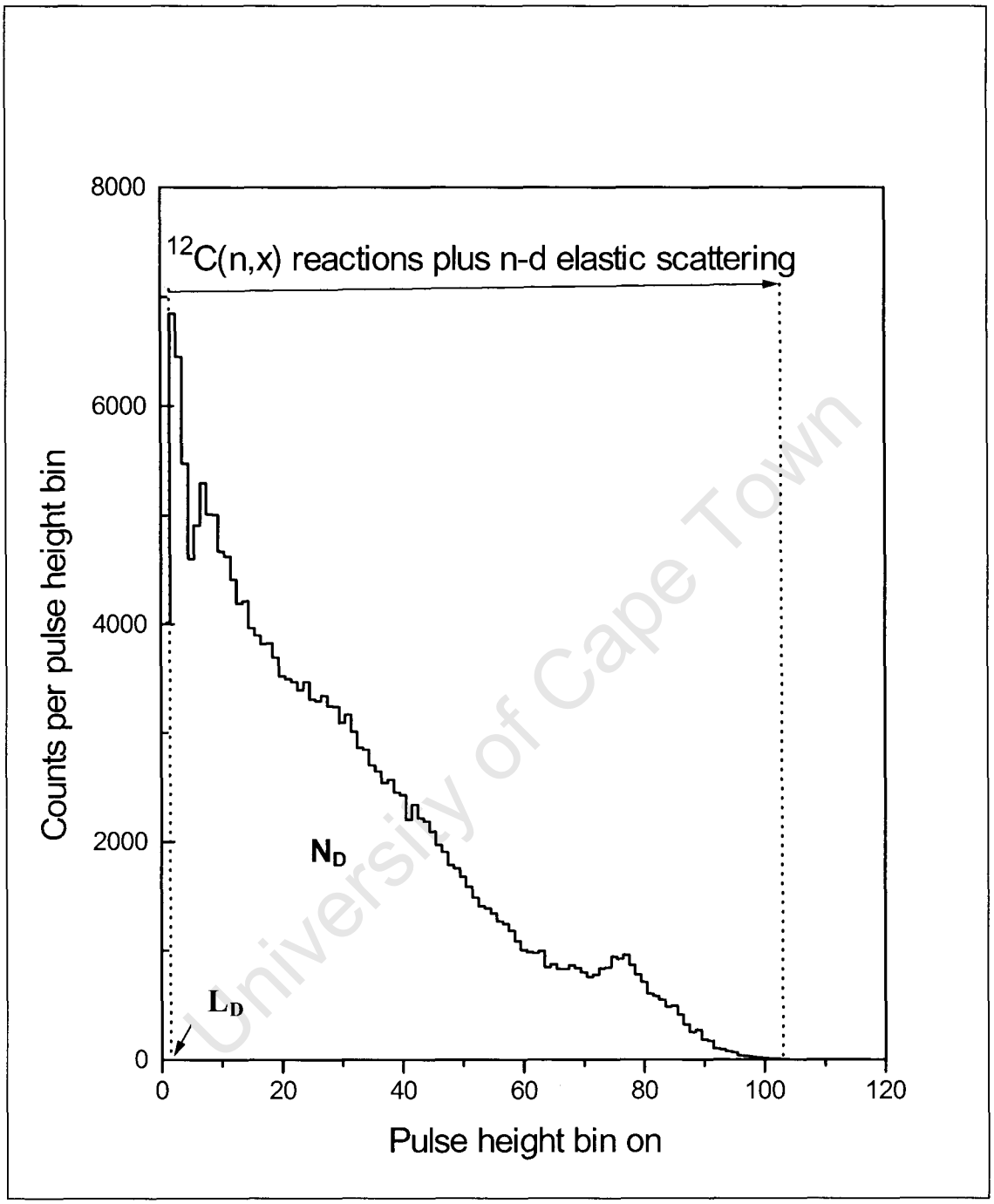

Fig. A-3 *Pulse height spectrum measured using the NE230 detector for incident neutrons of energy 64 MeV, with the PSD-cut (see section 2.5) set to select deuterons and heavier charged particles events.*

energy E for the energy range 5 to 64 MeV, using the time of flight data obtained during the in-air measurements (see section 2.6).

Discussed below is the calculation of the neutron detection efficiency, $\varepsilon_D(E,L_D)$ with uncertainty, $\Delta\varepsilon_D(E_n,L_D)$ of NE230 for neutrons of energy 64 MeV, shown in the calculation is how each quantity in equation A.9 was obtained separately. Pulse height spectra for neutrons of 64 MeV measured by the NE230 and NE213 detectors were obtained from the combined two-parameter (LT) data obtained in-air, using the Li, Be and C targets as described in section 2.6. The spectra are shown in figs. A-2 and A-3.

(a) M_i and M_o neutrons measured by the neutron monitor

The monitor reading M_i recorded for the data measured with the NE230 detector was 89166 and the reading M_o recorded for the data measured with the NE213 detector was 35664.

(b) N_D the integral count of the pulse height spectrum measured above the pulse height threshold L_D with NE230

The pulse height threshold L_D that was applied during the off-line analysis corresponded to a deuteron energy threshold of 5.6 MeV and incident neutron energy of 5 MeV. The integral count of the pulse height spectrum, N_D above L_D (see fig. A-3) was determined to be 207943 counts.

(c) N_{np} the integral counts of the pulse height spectrum measured above the pulse height threshold L_{np} with NE213

Pulse height L was determined as a function of proton energy E_p using the two-parameter (LT) data measured by the NE213 detector as described in section 2.6, see fig.4-A. The figure also shows a linear least square fit (solid line) to the data which is given by

$$L(E_p) = 1.5.E_p - 6.2 \text{ (in ADC channel)} \qquad \text{(A.10)}$$

Equation (A.10) together with the pulse height threshold $L_{np}(E_{np})$(use to select all the proton recoiling events from n-p elastic scattering, N_{np} (see fig. A-2)) was used to determine the corresponding proton threshold energy of E_{np} for all incident neutron energies. In the case of 64 MeV neutrons, $L_{np}(E_{np})$= 71 ADC channel which corresponds to proton threshold energy of E_{np}= 51.4 MeV. The integral count of the events of the pulse height spectrum, N_{np} above $L_{np}(E_{np})$ (see fig. A-2) was determined to be 8262 counts. Systematic uncertainties which affect the determined values $L_{np}(E_{np})$ are the uncertainties in the neutron energy (see section 2.6.2), wrong identification of proton deuteron events in the measurements (see section 2.5) and the shift in $L_{np}(E_{np})$ due to proton escapes at high neutron energies (see section 3.4). This was calculated to be within 10%.

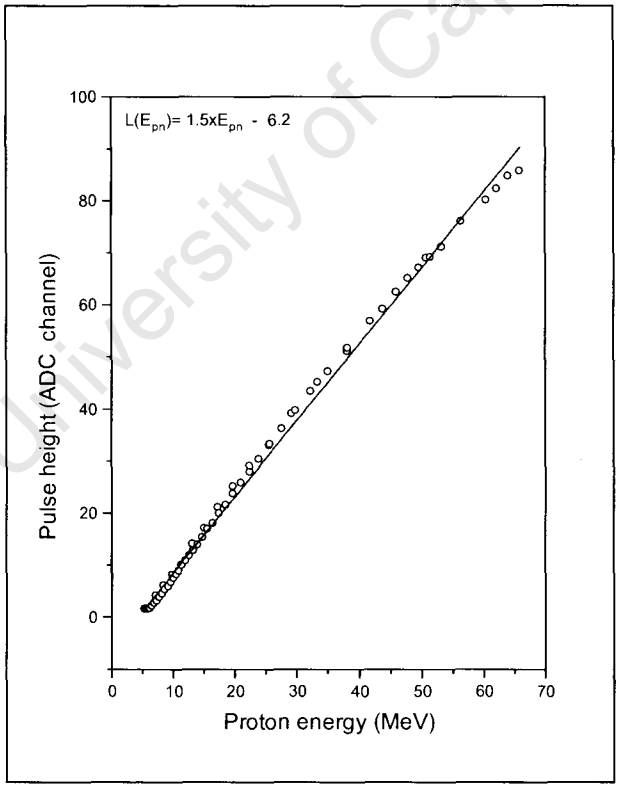

Fig. A-4: *Pulse height L versus proton energy E_p for the NE213 detector. The solid line is a linear least square fit to the data.*

(d) ϕ_{npf} the fraction of recoiling protons from n-p elastic scattering detected above pulse height threshold L_{np}

The recoiling protons from n-p elastic scattering with energy greater then E_{np} = 51.4 MeV lie within a cone with internal angle ξ in the laboratory frame. This angle is related to the incident neutron energy E_n and the recoiling proton energy E_p by:

$$\cos\xi = \frac{E_p}{m_p c^2(\gamma_2 - 1)} - 1 \tag{A.11}$$

where

$$\gamma_2 = \frac{\frac{m_p}{m_n} + \frac{E_n}{m_n c^2}}{\left[\left(\frac{m_p}{m_n}\right)^2 + \frac{2m_p E_n}{(m_n c)^2} + 1\right]^2} \tag{A.12}$$

Where m_p and m_n are the respective rest masses of the proton and neutron and c the speed of light.

The relationship between the angle of the scattered proton ξ in the laboratory frame and the angle of the scattered neutron θ in the center of mass frame is given by:

$$\xi = 180 - \theta \tag{A.13}$$

Combining equations A.10 and A.12 to obtain

$$\cos\theta = 1 - \frac{E_p}{m_p c^2(\gamma_2 - 1)} \tag{A.14}$$

Using equation (A.12) and (A.14) the relationship between the incident neutron energy E_n, the energy E_p over which recoil protons were selected for the integral count leading to recoiling proton threshold energy E_{np} and the associated scattered neutron angle θ_{np} in the center of mass frame can be expressed by:

$$\cos\theta = 1 - \frac{E_{np}}{m_p c^2(\gamma_2 - 1)} \tag{A.15}$$

The range of proton energy, E_p over which candidate recoil protons could be selected are E_p = 0 to E_n, which corresponds to a scattered neutron angle range θ = 0 to π . The

energy range of the recoil protons N_{np} are $E_p = E_{np}$ to E_n, which corresponds to a scattered neutron angle range $\theta = \theta_{np}$ to π. To obtain ϕ_{npf} (the fraction of recoiling protons from n-p elastic scattering detected above the recoiling proton threshold energy E_{np}) we integrate the differential cross section $\sigma_H(E,\theta)$ for n-p elastic scattering between the limits: $\theta = \theta_{np}$ to π and $\theta = 0$ to π, and then take the ratio of these integrals. In equation form ϕ_{npf} is expressed as:

$$\phi_{npf} = \frac{\int_{\theta_{np}}^{\pi} \sigma_H(E_n,\theta)d\theta}{\int_{0}^{\pi} \sigma_H(E_n,\theta)d\theta} \qquad (A.16)$$

Fig. A-5 shows differential cross sections for n-p elastic scattering data used in this work obtained from ENDF data sets [Ro91]. Shown in the figure are the recommended evaluations as a function of scattered neutron angle in the center of mass (cosine theta) and incident neutron energy in the range 10 to 100 MeV. For all energy below 10 MeV the angular distribution for n-p elastic scattering is isotropic in the center of mass, for this the differential cross sections for n-p elastic scattering is constant [Kn89]. When calculating the fraction of recoiling protons from n-p elastic scattering, ϕ_{npf} for 64 MeV neutrons detected above the recoiling proton threshold energy, E_{np}= 51.4 MeV, $\cos\theta_{np}$ was determined to be -0.608 and θ_{np}=127.3^0. Using θ_{np}= 127.3^0 and differential cross sections for n-p elastic scattering data at 64.0 MeV shown in fig. A-5 equation A.16 was evaluated and ϕ_{npf} was determined to be 0.255.

(e) ϕ_{npe} the escape correction factor for recoiling protons above pulse height threshold L_{np} that escape from the NE213 scintillator

The ranges of protons, deuterons, and alpha charged particles in NE213 organic liquid scintillators as a function of neutron energy are shown fig. A6. The ratio of the total number protons, which recoil directly forward from n-p elastic scattering events in the NE213 scintillator to the number of such protons, which do not escape from the scintillator, is given by (see Appendix D)

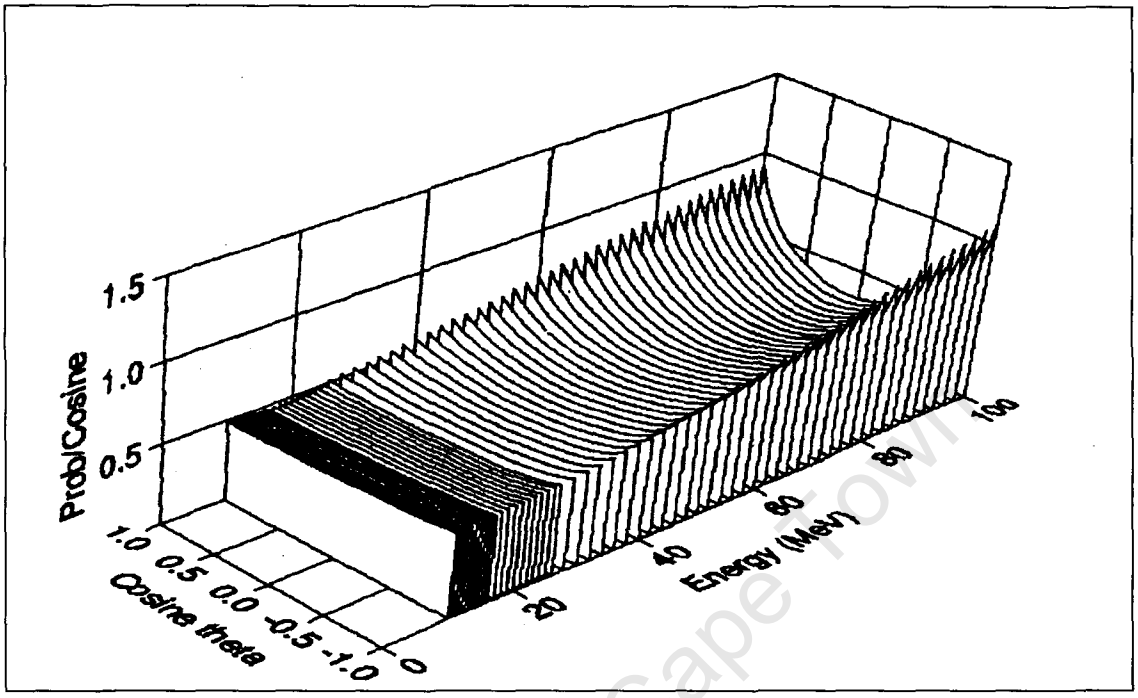

Fig. A-5 *Differential cross sections for n-p elastic scattering obtained from the ENDF data [Ro91]*

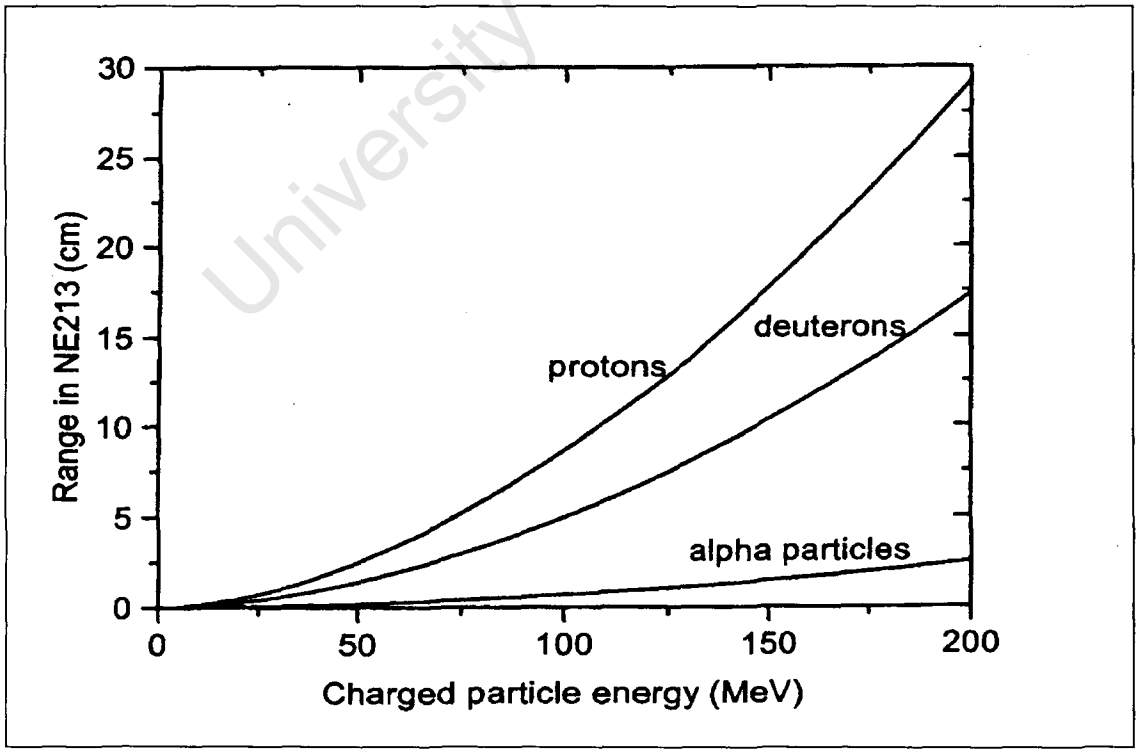

Fig. A-6 *Ranges in NE213 organic liquid scintillator for different charged particles as a function of neutron energy [Ji84].*

$$\frac{all\ protons\ events}{proton\ non\ escapes} = \frac{\pi r^2}{r^2 \cos^{-1}\left(\frac{s^2}{2r^2} - 1\right) - 0.5s\sqrt{4r^2 - s^2}} \quad (A.17)$$

where r is the radius of NE213 scintillator and s the range of a proton in the NE213 scintillator at a particular energy. From fig. A-6 the range of 64 MeV protons in NE213 is 3.95 cm, using this in equation A.17 and the radius of 2.5 cm of the NE213, the escape correction factor for recoiling protons, ϕ_{npe} above pulse height threshold L_{np} was determined to be 0.116. This correction only accounts for protons which recoil directly forward from n-p events in the scintillator which do not escape for the scintillator and is estimated to be a 90% correction [Bu90].

(f) σ_H the total cross-section for all n-p elastic scattering in the NE213 scintillator

Fig. A-7 shows total cross section for n-p elastic scattering used in this work obtained from the ENDF data sets [Ro91]. Using this σ_H the total cross-section for n-p elastic scattering at 64 MeV was determined to be 0.124 barn.

(g) n_H the number of hydrogen nuclei per unit cross sectional area presented to the neutron beam by the NE213 scintillator

The number of hydrogen nuclei per cm^2, presented to the neutron beam by the NE213 scintillator of length 5.0 cm is given by

$$n_H = \frac{N_A \eta_H \rho l}{M} \quad (A.18)$$

where:

N_A: Avogadro's number (= 6.022 x 10^{23} mol^{-1})

ρ: The density of the NE213 organic liquid scintillators (= 0.874g.cm^{-3})

l: The length of the of the NE213 organic liquid scintillator (= 5.0 cm)

η_H: The number of hydrogen atoms per molecule of NE213 scintillator (~ 10.2)

M: Molar mass of the NE213 scintillator (=106 g.mol^{-1})

Using the above information in the equation n_H was determined to be 0.252 $barn^{-1}$.

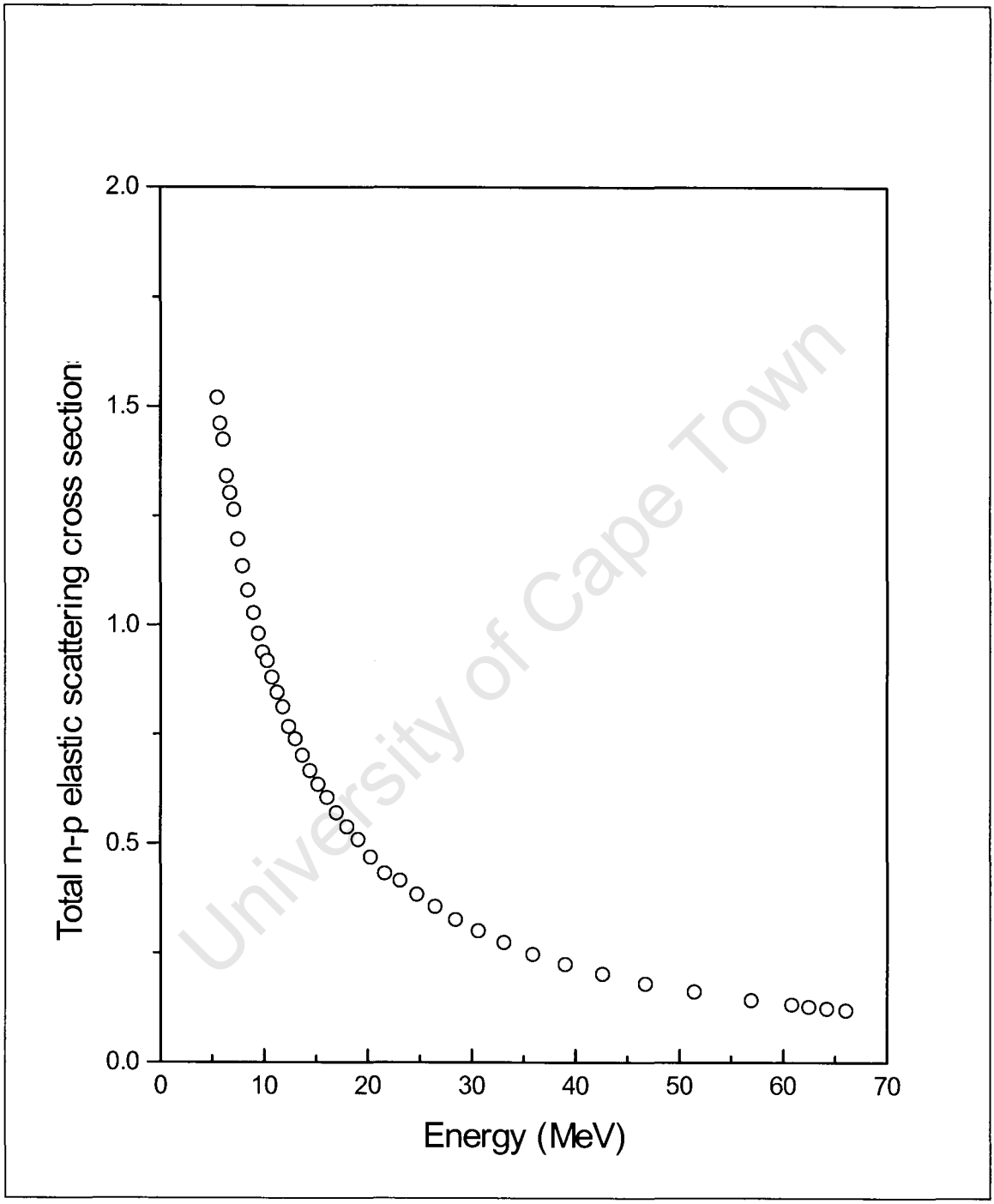

Fig. A-7 *Total n-p elastic scattering cross-section as a function of neutron energy [Ro91].*

Substituting all the above determined values in equation A.9 the detection efficiency of the NE230 for detecting neutrons of energy 64 MeV was determined to be 9.3 x 10^{-3}. Similar calculations were completed for the other neutron energies of interest. The neutron detection efficiency determined for the energies of interest together with the parameters used in equation A.9 to determine them is displayed in table A-2.

(h) $\Delta\varepsilon_D(E_n, L_D)$ **the uncertainty in** $\varepsilon_D(E_n, L_D)$

The uncertainty $\Delta\varepsilon_D(E_n, L_D)$ in the detection efficiency of NE230 $\varepsilon_D(E_n, L_D)$ arises from the input quantities used in equation (A.9). The uncertainty in each input quantity in equation (A.9) has been calculated according their category [Ta94, GUM]. The ratio $\frac{M_o}{M_i}$ is constant. The uncertainties in N_D and N_{np} are type A, random and are calculated using statistical methods (Gaussian distribution is used to model knowledge about them). Thus uncertainty in N_D and N_{np} is given by their square root. The uncertainties in $\phi_{npf}(E_n, L_{np}), \phi_{npe}(E_n, L_{np}), \sigma_{np}(E_n)$ and n_H are type B, is calculated on scientific judgment based on all available knowledge about their measurement. In these cases a rectangular probability density function (pdf) is used to model the available knowledge about them. Thus the uncertainty $u(x_i)$ in each is given by

$$u(x_i) = \frac{\frac{1}{2}(x_{right} - x_{left})}{\sqrt{3}} \tag{A.19}$$

where x_{right} and x_{left} are the limits of the pdf. The combined uncertainty in $\varepsilon_D(E_n, L_D)$ is then given by

$$\left[\frac{\Delta\varepsilon_D(E_n, L_D)}{\varepsilon_D(E_n, L_D)}\right]^2 = \sum_i \left[\frac{u(x_i)}{x_i}\right]^2 \tag{A.20}$$

where x_i and $u(x_i)$ are the best estimates and uncertainties respectively for each input quantity in equation (A.9). Using equations (A.19) the uncertainty $\Delta\varepsilon_D(E_n, L_D)$ in the detection efficiency of NE230 $\varepsilon_D(E_n, L_D)$ was determined, using the best estimates and uncertainties respectively for each input quantity in equation (A.9) at each energy. Table A-1 display the best estimate and uncertainty of each input quantity used in

equation (A.19) to determine uncertainty $\Delta\varepsilon_D(E_n, L_D)$ in the detection efficiency of NE230 $\varepsilon_D(E_n, L_D)$ for the incident neutron 64 MeV. The neutron detection efficiency with uncertainty as a function of neutron energy is shown in fig. 2.16 and is discussed in section 2.6.4. There is further systematic uncertainty discussed in section 3.4 which is not include in the statistical uncertainty determined here.

Table A-1: Best estimate and uncertainty of each input quantity used in equation (A.18) to determine uncertainty $\Delta\varepsilon_D(E_n, L_D)$ *in the detection efficiency of NE230,* $\varepsilon_D(E_n, L_D)$ *for the incident neutron 64 MeV.*

Input quantity	x_i	$u(x_i)$	Type uncertainty	x_{left}	x_{right}
N_D	207943	456	Type A	-	-
N_{np}	8262	91	Type A	-	-
$\phi_{npf}(E_n, L_{np})$	0.255	0.009	Type B	0.24	0.27
$\phi_{npe}(E_n.L_{np})$	0.116	0.032	Type B	0.06	0.17
$\sigma_{np}(E_n)$ (barn)	0.124	0.003	Type B	0.119	0.129
n_H (barn)	0.252	0.010	Type B	0.235	0.269

Table A-2: *The neutron energies and the neutron detection efficiency determined for each energy together with the parameters used to determine it.*

E_n (MeV)	σ_H (barn)	L_{np} channel	E_{np} (MeV)	θ_{np} (°)	ϕ_{npf}	ϕ_{npe}	N_{np} (counts)	N_{230} (counts)	ε_{230} 10^{-3}	$\Delta\varepsilon_{230}$ 10^{-3}
5.36	1.551	1	5.00	150.0	0.081	0.995	2064	6679	40.8	4.9
5.63	1.490	1	5.00	140.9	0.122	0.994	5893	16578	51.2	4.5
5.92	1.434	1	5.00	133.6	0.173	0.993	12431	29263	58.5	4.2
6.23	1.381	1	5.00	127.2	0.213	0.993	19401	34058	51.7	3.4
6.56	1.332	1	5.00	121.6	0.254	0.992	44215	61004	46.7	2.9
6.93	1.271	1	5.00	116.3	0.294	0.991	64438	73360	42.5	2.5
7.32	1.230	1	5.00	111.5	0.334	0.990	51389	49763	39.7	2.3
7.75	1.165	1	5.00	106.9	0.370	0.975	44925	36282	34.2	1.9
8.22	1.107	1	5.00	102.5	0.405	0.974	80131	53335	29.3	1.6
8.65	1.067	1	5.00	99.0	0.435	0.973	112207	66672	27.0	1.5
9.20	1.004	1	5.00	95.0	0.475	0.971	73326	41920	26.7	1.5
9.60	0.970	1	5.00	92.4	0.502	0.970	82879	46704	26.8	1.5
10.03	0.938	1	5.00	89.8	0.514	0.963	94527	52672	26.1	1.4
10.49	0.899	1	5.00	87.3	0.540	0.961	95448	53700	26.5	1.4
10.97	0.862	1	5.00	84.9	0.560	0.960	91889	50720	25.8	1.4
11.50	0.828	1	5.00	82.5	0.579	0.953	102650	56878	25.5	1.4
12.06	0.796	1	5.00	80.2	0.599	0.951	105745	58087	25.1	1.3
12.67	0.760	1	5.00	77.8	0.614	0.945	116404	63911	24.4	1.3
13.32	0.723	1	5.00	75.6	0.634	0.943	124400	66950	23.4	1.3
14.02	0.689	1	5.00	73.3	0.658	0.937	140854	75858	23.1	1.2
14.78	0.655	1	5.00	71.1	0.672	0.930	141878	76080	22.1	1.2
15.61	0.620	1	5.00	68.9	0.692	0.924	143053	78419	21.9	1.2
16.51	0.587	1	5.00	66.8	0.707	0.913	157069	89208	21.7	1.2
17.49	0.553	1	4.90	63.9	0.731	0.905	172573	101251	21.6	1.2
18.56	0.523	1	5.97	69.1	0.692	0.894	180657	112290	20.3	1.1
19.73	0.489	4	7.14	74.0	0.653	0.882	172057	136003	22.4	1.2
21.02	0.458	6	8.43	78.6	0.614	0.867	177157	169641	23.5	1.3
22.43	0.426	8	9.84	83.0	0.574	0.850	179317	217779	25.4	1.4
24.00	0.397	10	11.41	87.2	0.540	0.832	179734	276116	27.6	1.6
25.75	0.368	14	13.16	91.3	0.504	0.808	165502	329800	30.1	1.8
27.69	0.337	17	15.10	95.2	0.470	0.782	157532	361338	28.6	1.7
29.87	0.307	21	17.28	99.0	0.437	0.750	146123	392220	27.2	1.7
32.31	0.281	25	19.72	102.8	0.409	0.712	131524	409511	25.7	1.6
35.08	0.255	29	22.49	106.4	0.382	0.667	114721	424545	24.2	1.6
38.23	0.230	33	25.64	110.0	0.355	0.613	96212	411039	21.6	1.5
41.83	0.206	39	29.24	113.5	0.329	0.547	63276	344649	20.4	1.5
45.97	0.184	45	33.38	116.9	0.309	0.468	54400	392422	19.3	1.6
50.78	0.163	51	38.19	120.3	0.286	0.373	53304	455357	15.0	1.5
56.42	0.144	59	43.83	123.6	0.274	0.260	40437	458672	11.7	1.6
60.44	0.132	65	47.85	125.7	0.261	0.182	7431	101125	8.6	1.6
62.18	0.128	67	49.59	126.5	0.258	0.149	5696	106151	9.2	2.0
63.99	0.124	71	51.40	127.3	0.255	0.116	8262	207943	9.3	2.6
65.89	0.119	73	53.30	128.2	0.247	0.084	4860	10452	5.0	2.0

Appendix B

Unfolding methods and MAXED input details

Briefly, there are many direct inversion methods [Pr96, Re06], that can be used to solve equation 3.2 (section 3.1); examples of these, which have been applied, are the derivative methods [Mi83, Cr89] and matrix inversion methods [Ma94, Re06]. Unfolding codes based on the derivative method include: DUFOLD [Co71], NEUSTP [To71] and FLYSPEC [Sl76]. Smoothing of the measurements are required in these codes and may lead to the elimination of fine structure in the measured data that can result in poor solutions and sometimes lead to non-physical solutions of equation 3.2 [Re06].

There are a number of matrix inversion unfolding codes based on different unfolding algorithms available that can be used to solve equation (3.2). Many of these codes use unfolding algorithms based on the least squares method; for example SANDII [Mc67], FERDOR [Bu65], FORIST [Jo75], LOUHI [Ro80] and GRAVEL [Ma94]. These codes use iterative routines that involve the use of some initial energy spectrum to start the unfolding. Alternatives to least squares unfolding include Monte Carlo methods, for example the code MIEKE [Ma94]; maximum entropy methods, for example the code MAXED [Re02] and other approaches based on the use of genetic algorithms [Fr99] and neural networks [Br02a].

As noted in Chapter 3, MAXED was used for the unfolding based on the arguments presented by Reginatto. For completeness, the following section is taken from the MAXED manual.

The input parameters to MAXED are the following;

L_k : neutron spectrometric measurements,

σ_k : estimate of the measurement error

f_i^{DEF} : prior spectrum

Ω : a parameter that fixes the chi-squared of the solution spectrum

Equations (B1) and (B2) define the constraints on the set of solution spectra to the unfolding problem given by equation 3.2.

$$L_k + \varepsilon_k = \sum_i R_{ki} f_i \tag{B1}$$

$$\sum_k \frac{\varepsilon_k^2}{\sigma_k^2} = \Omega . \tag{B2}$$

Equation (B1) is an integral equation that relates the measurement to the detector response matrix and the neutron energy spectrum, allowing for measurement error. Equation (B2) is a constraint for handling the ε_k, and assumes that the chi-squared statistic of the solution spectrum is equal to a value determined by the user. From this set of solution spectra, we want to calculate the one that maximizes the entropy S expression (B3) given by

$$S = -\sum_i \left\{ f_i \ln\left(\frac{f_i}{f_i^{DEF}} \right) + f_i^{DEF} - f_i \right\}. \tag{B3}$$

The unfolding leads to a set of output parameters $\{\lambda_i\}$ that satisfies the following set of equations:

$$f_i = f_i^{DEF} \exp\left\{ -\sum_k \lambda_k R_{ki} \right\} \tag{B4}$$

$$\varepsilon_k = \frac{\lambda_k \sigma_k^2}{2} \left(\frac{4\Omega}{\sum_j (\lambda_j \sigma_j)^2} \right)^{\frac{1}{2}} . \tag{B5}$$

Equation (B4) is an expression for the solution spectrum and equation (B5) the uncertainties associated with the solution spectrum. Since the maximum entropy solution spectrum can be written in closed form, uncertainties associated with the solution spectrum can be calculated by considering variations in L_k and f_i^{DEF}. However, the uncertainties do not include uncertainties in the response matrix. Therefore, the determination of the uncertainties associated with the solution spectrum still remains a challenge [Th02]

Appendix C

MCNPX INPUT FILE

Input file with parameters to simulate the neutron energy spectrum at a position (8cm, 0 cm) in the water phantom.

```
Neutron detector design, depth (8,0)(detector assembly)

C Cell Cards
1 0 1:-2:3:-4:5:-6                                  $ Outside of room
2 1 -0.945 -13                                      $ Scoring sphere
3 1 -0.945 13 14 -15 -16                            $ Scintillator
4 0 16 -17 -18                                      $ PMT bottom
5 0 18 -17 -19                                      $ PMT top
6 4 -1.3 17 18 -19 -20                              $ PVCT
7 2 -1.0 7 -8 -9 10 -11 12 #3 #2 #4 #6 #5           $ Phantom
8 3 -0.00121 -1 2 -3 4 -5 6 (-7:8:9:-10:11:-12) $ Air
C End Of Cell Cards

C Surface Cards
1 PZ 500                                            $ Room
2 PZ 0
3 PY 250
4 PY -250
5 PX 250
6 PX -250
7 PZ 350                                  $ Front of phantom (isocentre)
8 PZ 410                                            $ Back of phantom
9 PY 30                                             $ Side of phantom
10 PY -30                                           $ Side of phantom
11 PX 30                                            $ Side of phantom
12 PX -30                                           $ Side of phantom
13 1 SO 1.215                                       $ Scoring Sphere
14 1 PX -1.25                                       $ Bottom of scintillator
15 1 CX 1.25                                        $ Scintillator
16 1 PX 1.25                                        $ Top of scintillator
17 1 CX 3.0                                         $ PMT
18 1 PX 6.25                                        $ Bottom of PMT&PVCT
```

```
19 1 PX 29.0                                          $ Top of PMT&PVCT
20 1 CX 3.5                                           $ PVCT
C End Of Surface Cards

C   Data cards
mode n
imp:n 0 1 1 1 1 1 1 1
SDEF pos=0 0 0 axs 0 0 1 sur=2 rad=d1 vec=0 0 1 dir=d2 erg=d3 par=1
si1 1.25
sp1 -21
si2 0.9999 1.0
sp2 0 1.0
si3 5.23 5.49 5.77 6.07 6.39 6.74 7.12 7.53 7.98 8.47 9.01 9.40&
9.81 10.25 10.73 11.23 11.77 12.36 12.99 13.66 14.39 15.19 16.05&
16.99 18.01 19.13 20.36 21.71 23.20 24.85 26.69 28.75 31.05 33.65&
36.60 39.96 43.82 48.29 53.49 59.60 61.30 63.08 64.93 66.87
sp3 0 5662 11777 19709 27021 57066 76894 59320 50497 90717 119852&
74195 82463 95096 97774 92519 104275 112151 125984 139915 160563&
171357 178721 202627 234815 273153 315223 365234 439882 529855 629834&
761434 883309 1005058 1197645 1385463 1668971 1889588 2120933 1775385&
1068140 3653571 18109345 154579
*TR1 0 0 358 30 120 90 60 30 90 90 90 0
F1:n 13                                       $ Fluence scoring position
C1 0 1                                        $ Outside of scoring sphere
E0 5.23 5.49 5.77 6.07 6.39 6.74 7.12 7.53 7.98 8.47 9.01 9.40&
9.81 10.25 10.73 11.23 11.77 12.36 12.99 13.66 14.39 15.19 16.05&
16.99 18.01 19.13 20.36 21.71 23.20 24.85 26.69 28.75 31.05 33.65&
36.60 39.96 43.82 48.29 53.49 59.60 61.30 63.08 64.93 66.87
cut:n j 4.0
m1 1002.24c -0.1429 6000.24c -0.8571          $ Deuterated scintillator
m2 1001.24c -0.1111 8016.24c -0.8889          $ Water
m3 8016.24c -1.0                              $ Air
m4 1001.24c -0.0800 8016.24c -0.32 6000.24c -0.6000 $ LG(Lucite)
nps 20000000
PRDMP j j j 2
```

Appendix D

Derivation of the proton escape correction factor

Consider neutrons of energy E incident of on the curved surface of a cylindrical NE213 scintillator detector of radius r placed perpendicular to the incident neutron beam. Say, protons which recoil directly forward from n-p events in a scintillator and deposit their energy in the scintillator have a range s in the scintillator, as show in the sketch below.

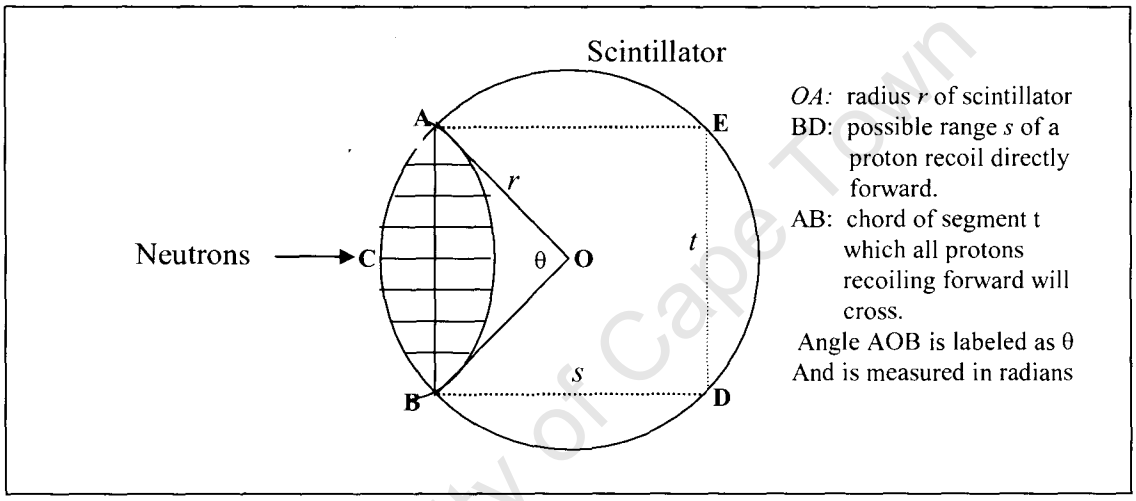

The ratio *R* of all proton recoiling events from n-p to protons recoiling events recoiling directly forward that does not escape from the scintillator is given by the expression

$$R = \frac{all\ proton\ recoil\ events\ produced\ in\ scintillator}{all\ directly\ forward\ recoiling\ proton\ events\ not\ escaping\ from\ scintillator} = \frac{\pi r^2}{shaded\ area} \qquad \text{(D1.)}$$

The shaded area is given by

$$Shaded\ area = 2(Area\ of\ segment\ OACB - Area\ of\ \Delta AOB) \qquad \text{(D.2)}$$

The area of segment OACB given in terms of *r* and *s*

$$Area\ of\ segment\ OACB = \frac{1}{2}\theta r^2$$

$$using\ the\ cosine\ rule\ t\ can\ be\ express\ as\ t^2 = 2r^2 - 2r^2\cos\theta$$

$$but\ \ t\ \ also\ \ t^2 = 4r^2 - s^2\ \ for\ forward\ recoil\ protons\ not\ escaping\ from\ the\ scintillator$$

$$Combinnig\ this\ give\ \theta = \cos^{-1}\left[\frac{s^2}{2r^2} - 1\right]$$

$$\therefore\ Area\ of\ segment\ OACB = \frac{1}{2}r^2\cos^{-1}\left[\frac{s^2}{2r^2} - 1\right] \qquad (D.3)$$

The area ΔAOB in terms of t and *s*

$$Area\ \ of\ \ \Delta AOB = \frac{1}{4}Area\ of\ \ Square\ ABDE = \frac{1}{4}ts$$

$$= \frac{1}{4}s\sqrt{4r^2 - s^2} \qquad (D.4)$$

Combining (D.2), (D.3) and (D.4) the shaded area is given by

$$Shaded\ area = 2(Area\ \ of\ \ segment\ OACB - Area\ of\ \ \Delta AOB)$$

$$= r^2\cos^{-1}\left(\frac{s^2}{2r^2} - 1\right) - \frac{1}{2}s\sqrt{4r^2 - s^2} \qquad (D.5)$$

Combining (D.1) and (D.5) given the ratio R as

$$R = \frac{all\ proton\ recoil\ events\ \ produced\ \ in\ \ scintillator}{all\ directly\ \ forward\ \ recoiling\ \ proton\ events\ not\ \ escaping\ from\ scintillator}$$

$$= \frac{\pi r^2}{r^2\cos^{-1}\left(\frac{s^2}{2r_2} - 1\right) - \frac{1}{2}s\sqrt{4r^2 - s^2}}$$

This correction only accounts for protons which recoil directly forward from n-p events in the scintillator which do not escape for the scintillator and is estimated to be a 90% correction [Bu90]. The uncertainties in R are type B, is calculated on scientific judgment based on all available knowledge used in its determination [Ta94, GUM].

REFERENCES

[AA80] Protocol for neutron beam dosimetry, AAPM Report **no.7,** (1980)

[Ad78] J.M. Adams and G.White, A versatile pulse shapes discriminator for charge particle separation and its application to fast neutron time of flight spectroscopy Nucl. Instr. Meth. **156**, 459-476 (1978).

[Ag03] S. Agostinelli, *et al,* GEANT4-a simulation toolkit Nucl. Instr. Meth. **A506,** 250-303 (2003).

[Aw80] M. Awschalom, I. Rosenberg, Conceptual design of beryllium targets for the generation of neutron beams for radiation therapy by the (p,n) reaction. Med.Phys. **7**, 492-494 (1980)

[Be69] H.W. Bertini, Intranuclear-cascade calculation of the secondary nucleon spectra from nucleon-nucleus interactions in the energy range 340 to 2900 MeV and comparison with experiment. Phys. Rev **188**, 1711-1730 (1969).

[Be87] John W. Bennett and Malcolm C. Scott, Fast neutron spectrum measurements in anthropomorphic phantoms using an NE213 scintillation spectrometer. Phys. Med. Biol. **32**, 1645-1648 (1987).

[Be02] S. Benck, F.D. ` Errico, J. M. Denis, J.P. Meulders, R. Nath, E.J. Pitcher, In phantom spectra and dose distributions from a high- energy neutron therapy beam, Nucl. Instr. Meth. **A476,** 127-131 (2002).

[Bi64] J.B. Birks, in Theory and practice of scintillation counting, (Pergamon Press, 1964)

[Bi87] P.J. Binns and J.H. Hough, Spectral energy measurements in a fast neutron therapy field, Nucl. Instr. Meth. **A255,** 330-333 (1987).

[Bi98] P.J. Binns, P.M. DeLuca Jr, R.L. Maughan and C. Kota, Direct determination of kerma for a d (48.5) + Be therapy beam. Phys. Med. Biol. **43**, 3449-3457 (1998).

[Bl55] L. Blumberg and S.I. Schlesinger. Kinematics of the relativistic tow body problem. Report LAMS-1718-C3, Los Alamos National Laboratory (August 1955)

[Bo82] D.E. Bonnett, and C.J. Parnell, Effect of variation of the energy spectrum of a cyclotron-produced fast neutron beam in a phantom relevant to its application in radiotherapy, Br.J.Radiol **55**, 48-55 (1982)

[Bo99] Tim D. Bohm, Paul M. Deluca, Jr., Lawrence J. Cox, Richard L. Maughan, D.T.L. Jones, Arlene Lennox. Monte Carlo calculations to characterize the source for neutron therapy facilities. Med. Phys. **26,** 783-792 (1999).

[Br79] F.D. Brooks, Development of organic scintillators. Nuc. Instr. Meth. **162**, 477-505 (1979).

[Br81] J.J. Broerse, B.J. Mijnheer, and J.R. Williams; European protocol for neautron dosimetry for external beam therapy. Br .J. Radiol. **58**, 882-898 (1981)

[Br88] F.D. Brooks, W.A. Cilliers, B.R.S. Simpson, F.D. Smit, M.S. Allie, D.T.L. Jones, W.R. MucMurry and J.V. Pilcher. Deuterated anthracene spectrometer for 5-30 MeV neutrons. Nucl.Instr.Meth. **A270**, 149-156 (1988).

[Br97] J.F. Briemeister, editor, MCNP^{TM} – A general Monte Carlo N-Particle Transport Code, report LA-12625-M, Los Alamos National Laboratory (March 1997)

[Br02a] C.C. Brag and M.S. Dias, application of neural networks for unfolding neutron spectra measured by means of Bonner spheres, Nucl. Instr. Meth. **A476**, 252-25 (2002)

[Br02b] F.D. Brooks, H. Klein, Neutron spectrometry- historical review and present status, Nucl. Instr. Meth. **A476,** 1-11 (2002).

[Br04] F.D. Brooks, M.S. Allie, A. Buffler, V. Dangendorf, M.S. Herbert, S.A. Makupula, R. Nolte and F.D. Smith, Measurements of a neutron fluence spectra up to 150 MeV using a stacked scintillator neutron spectrometer. Radiat. Prot. Dosim. **110**, 151-155 (2004).

[Br07] F. D. Brooks, A. Buffler, M. S. Allie, M. S. Herbert, M. R. Nchodu, D. T. L. Jones, F. D. Smit, R. Nolte and V. Dangendorf, A compact high-energy neutron spectrometer, Radiat. Prot. Dosim. **126,** (1-4): 218-222 (2007)

[Bu65] W.R. Burrus, Utilization of a prior information by means of mathematical programming in the statistical interpretation of measured distribution. Oak Ridge National Laboratory ORNL-3743, (1965)

[Bu90] A. Buffler, The response of organic scintillators to neutrons of energy 14-63 MeV, M.Sc thesis, University of Cape Town, unpublished (1990).

[Ca04] J.F. Carrier, L. Archambault, L. Beaulieu and R. Roy, Validation of GEANT4, an object- orientated Monte Carlo toolkit, for simulations in medical physics. Med. Phys. **31**, 484-492 (2004).

[Ch99] M.B. Chadwick, H.H. Barschall, R.s. Caswell, P.M. Deluca, G.M. Hale, D.T.L. Jones, R.E. MacFarlane, J.P. Meulders, H. Schuhmacher, U.J. Schrewe, A. Wambersie and P.G. Young, A consistent set of neutron kerma coefficients from thermal to 150 MeV for biologically important materials, Med.Phys. **26**, 974-990 (1999).

[Co71] M.J. Coolbaugh, R.E Faw and W. Meyer, Report COO-2049-7, (1971)

[Cr89] N.M.J. Crout, J.G. Fletcher and M.C. Scott, Calibration of an NE213 scintillator up to 60 MeV for in situ spectrometry in a neutron cancer therapy facility. Nucl. Instr. Meth. **A277**, 664-668 (1989).

[Cr91] N.M.J. Crout, J.G. Fletcher, S. Green, M.C. Scott and G.C. Taylor, *In situ* neutron spectrometry to 60 MeV in a water phantom exposed to a cancer therapy beam. Phys. Med. Biol.**36,** 507-519 (1991).

[Da00] S. Dangtip, A. Atac, B. Bergenwall, J. Blomgroen, K. Elmgren, C. Johansson, J. Klug, N. Olsson, G. Alm Carlsson, J. Söderberg, O. Jonsson, L. Nilsson, P-.U. Renberg, P. Nadel- Turonski, C. Le Brun, F. R. Lecolly, C. Varingnon, Ph. Eudes, F. Haddad, M. Kerveno, T. Kirchner, C. Lebrum, A facility for measurements of nuclear cross sections for fast neutron cancer therapy. Nucl. Instr. Meth. **A452**, 484-504 (2000).

[De98] J.J. DeMarco, T.D. Solberg, and J.B. Smathers, A CT- based Monte Carlo simulation tool for dosimetry planning and analysis. Med. Phys. **25**, 1- (1998).

[Di88] J.K. Dickens, Oak Ridge National Laboratory, Report ORNL-6462 (1998).

[Dö83] B. Dörschel and G. Streubel, Some Characteristics of neutron field and kerma distributions inside a phantom irradiated at a cyclotron. Rad. Prot. Dosim. **5**, 65-70 (1983).

[Dö95] B. Dörschel, V. Schuricht, J. Steuer, The Physics of radiation protection. (Nuclear Technology Publishing, 1995).

[Do03] J.G. Douglas, W.J. Koh, M. Austin-Seyemour, G.E. Laramore, Treatment of salivary gland neoplasms with fast neutron radiotherapy. Arch Otolaryngol Head Neck Surg. **129,** 944-948 (2003).

[Fr99] David W. Freeman, D. Ray Edwards, Albert E. Bolon, Genetic algorithms: A new technique for solving the neutron spectrum unfolding problem. Nucl. Instr. Meth. **A425**, 549-576 (1999).

[Go02] P. Goldhagen, M. Reginatto, T. Kniss, J.W. Wilson, R.C. Singleterry, I.W. Jones, W. Van Steveninck, Measurements of the energy spectrum of cosmic-ray induced neutrons aboard an ER-2 high-altitude airplane. Nucl. Instr. Meth. **A476**, 42-51 (2002).

[GNU] Data reduction software available in the Physics Department, University of Cape Town.

[GUM] International Organization for Standardization, Guide to the expression of uncertainty in measurement. Geneva, Switzerland (1995)

[Hu97] H. Hughes, R. Prael and R. Little, *MCNPX- The LAHET/MCNP code merge*. X-Division research note XTM-RN(U) 97-012, LA-UR- 97- 4891, Los Alamos National Laboratory (1997).

[Hu01] P.E Huber, J. Debus, and D. Latz, et al. Radiotherpy for advanced adenoid cystic carcinoma: Neutrons, photons or mixed beam? Radiot. Oncol. **9**, 161-167 (2001).

[IC45] ICRU report 45. Clinical neutron dosimetry part I: Absorbed dose in a patient treated by external beams of fast neutrons. International commission of radiation units and measurements, Bethesda, MD, (1989).

[ITH] iThemba Laboratory for Accelerator Based Sciences, P.O. BOX 72, Faure, Cape Town, South Africa, 7131.

[Ji84] P. Jipsen and J.Maritz, Program ELOSS 2.0, based on data from H.H. Andersen and J.F. Ziegler, in the stopping and ranges of ions in matter, Volume 3, 4 and 5, (Pergamon Press, New York, 1977).

[Jo75] R.H. Johnson, A user's manual for COOLC and FORIST. Radiation Shielding Information Centre PNE-75-107, 1975

[Jo92] D.T.L. Jones, J.E. Symons, and T.J. Fulcher, F.D. Brooks, M.R. Nchodu, M.S. Allie, A. Buffler and M.J. Olivier, Neutron fluence and kerma spectra of a p(66)/ Be (40) clinical source. Med. Phys. **19**,1285-1291 (1992).

[Jo01a] D.T.L. Jones and A.N. Schreuder, Magnetically scanned proto therapy beams: rationales and principles. Rad. Phys. Chem. **61**, 615-618 (2001).

[Jo01b] D.T.L. Jones, Fast neutron and proton therapy sources. Radiochim. Acta **89,** 265-277 (2001).

[Jo07] D.T.L. Jones, A. Wambersie, Radiation therapy with fast neutrons: a review. Nucl. Instr. Meth. **A580,** 522-525 (2007)

[Kn89] G.F. Knoll, in Radiation Detection and Measurement, 2 edition, (Wiley, New York, 1989).

[La93] G.E. Laramore, J.M. Krall, T.W. Griffin, W. Duncan, M.P. Richter, K.R. Saroja, M.H. Maor, L.W. Davis. Neutron vs. photon irradiation for unrespectable salivary gland tumors: final report of an RTOG-MRC randomized clinical trial. Int. J. Radiat. Oncol. Biol. Phys. **27**,235-240, (1993).

[Le01] Arlene J. Lennox, Accelerators for cancer therapy. Radiat. Phys. Chem. **61**, 223-226 (2001).

[Ma92] R.L. Maughan, Neutron radiation therapy. Br. J. Radiol. Suppl. **24**, 204-208 (1992).

[Ma94] M. Matzke, Unfolding of pulse height spectra: The HEPRO program system, Report PTB-N-19, Physikalisch-Technische Bundesanstalt, Braunschweig, (1994).

[Ma02] M. Matzke, Propagation of uncertainties in unfolding procedures, Nucl. Instr. Meth.**A476,** 230-241 (2002).

[Mc67] W.N. McElroy, S. Berg, T. Crockett and R.G. Hawkins, A computer-automated iterative method for neutron flux spectra determination by foil activation, SAND_II, Report AFWL-TR-67-41, U.S. Air Force Weapons Laboratory, (1967)

[Mc75] A.K. McCracken and M.J. Grimshore, Proc. 1 st Symp. on Reactor Dosimetry (1975).

[Mo82] P.J. Mountford, A miniaturized tissue- equivalent organic liquid scintillator for fast-neutron spectrometer. Phys. Med. Biol. **27**, 97-105 (1982).

[Mi83] W. H. Miller and W. Meyer, Standardization of neutron spectrum unfolding codes: testing using idealized, calculated response functions. Nucl. Instr. Meth. **205,** 185-195 (1983).

[Mi87] B.J. Mijnheer, P. Wotton, J.R. Williams, J. Eenmaa and C.J. Parnell; Unifromity in dosimetry protocols for therapeutic applications of fast neutron beams. Med.Phys. **14**, 1020-1026 (1987)

[Pa72] C.J. Parnell, A fast neutron spectrometer and its use in determining the energy spectra of some cyclotron-produced fast neutron beams, Br.J.Radiol. **45**, 452-460 (1972)

[Pa73] G. Pauletta, The neutron-deuteron breakup cross section between 8 and 22 MeV. PhD thesis, University of Cape Town, unpublished (1973).

[Pa75] G. Pauletta and F.D. Brooks, Cross-sections for n + d breakup reaction, Nucl. Phys. **A255**, 267-274 (1975).

[Pe79] L.J. Perkins and Malcolm C. Scott, The application of pulse shape discrimination in NE213 to neutron spectrometry. Nucl. Instr. Meth. **166**, 451-464 (1979).

[Pr89] R.E. Prael and H. Lichtenstein, User guide to LCS: LAHET CODE SYSTEM, report LA-UR-89-3014, Los Alamos National Laboratory, (1989)

[Pr96] W.H. Press, B.P. Flannery, S.A. Teukolsky and W.T. Vetterling, in Numerical recipes: the art of scientific computing, Cambridge University Press, Cambridge (1996).

[RCA] RCA specification sheet 6-72, available from RCA electronics Components, Harrison, NJ 07029

[Re99] M. Reginatto and P. Goldhagen, MAXED, a computer code for maximum entropy deconvolution of multispehere neutron spectrometer data. Health Physics. **77**, 579-583 (1999).

[Re02] M. Reginatto, P. Goldhagen and S. Neumann, Spectrum unfolding, sensitivity analysis and propagation of uncertainties with the maximum entropy deconvolution code MAXED. Nucl. Instr. Meth. **A476,**242-246 (2002).

[Re06] M. Reginatto, Mathematical formulation of neutron spectrum unfolding: a set of (informal) notes: Course offered at the University of Cape, April 2006

[Ro80] J.T. Routti and J.V. Sandberg, General purpose unfolding program LOUHI78 with linear and nonlinear regulations. Comput. Phys. Comm, **21**, 119-144 (1980).

[Ro91] P.F. Rose, ENDF-201: ENDF/B-VI Summary Documantation, Report BNL-NCS-17541, Brookhaven National Laboratory (1991)

[Ro97] M.A. Ross, P.M. DeLuca Jr., D.T.L. Jones, A. Lennoux and R.L. Maughan, Calculated fluence spectra at neutron therapy facilities. Rad. Prot. Dosim. **70**, 481-484 (1997).

[Ro06] D.W.O. Rogers, Fifty years of Monte Carlo simulations for medical physics. Phys. Med. Biol. **51,** R287-R301 (2006).

[Ru93] K.J. Russell, R.J. Caplan, G.E. Laramore, C.M. Burnison, M.H. Maor, M.E. Taylor, S. Zink, L.W. Davis, T.W. Griffin, Photon versus fast neutron external beam radiotherapy in the treatment of locally advanced prostate cancer: Results of randomized prospective trail. Int. J. Radiat. Oncol. Biol. Phys. **28**, 47-54 (1993).

[Sc81] M.C. Scott, J.W. Bennett and J.S. Petler, Neutron spectrum studies in phantoms from 30 keV to 14 MeV, Proc. 4th Symp. Neutron Dosimetry vol **2** EUR 7448, 167-168 (1981)

[Sh90] Jacob Shapiro, RADIATION PROTECTION: A guide for Scientist and Physicians, Third Edition. Harvard University Press, Cambridge, Massachusetts, and London, England, (1990).

[Sl76] D.R. Slaugther, A review of radiation energy spectra unfolding, compiled by D.K. Truben, ORNL/RSIC-40. (1976).

[Sm87] F.D. Smit and F.D. Brooks, Angular distribution of neutrons from at E = 2.75 MeV. Nucl. Phys. **A465**, 429-444 (1987).

[So00] Jonas Söderberg and Alm Carlsson Gudrun, Fast neutron absorbed dose distributions in the energy range 0.5 – 80 MeV- a A Monte Carlo study, Phys. Med. Biol. **45**, 2987-3007 (2000)

[St71] N.R. Stanton, Ihio State University Report COO-1545-92, 1971. !!!

[Ta94] B.N. Taylor and C.E. Kuyatt, Guidelines for evaluating and expressing of the uncertainty NIST measurement results, National Institute of standards and technology (NIST) technical note 1297 (1994).

[Te68] R.R. Textor and V.V. Verbinski, ORNL-4160, Oak Ridge National Laboratory. (1968).

[Te82] R.K. Tenhaken, M. Awschalom, I. Rosenberg, Update of neutron dose yields as a function of energy for protons and deuterons, incident on beryllium targets. Report TM-1146, Fermi National Accelerator Laboratory, Batavia, IL (1982)

[Th02] D.J. Thomas, A.V. Alevra, Bonner sphere spectrometers- a critical review. Nucl. Instr. Meth. **A476**, 12-20 (2002).

[To71] M.E. Toms, Computer analysis to obtain neutron spectra from an organic scintillator. Nucl. Instr. Meth. **92**, 61-70 (1971).

[Tu95] James E. Turner, ATOMS, RADIATION, AND RADIATION PROTECTION. Second Edition, John Wiley & Sons. Inc. New York, (1995).

[Wa99] L.S. Waters, editor, MCNPX^{TM} user manual, report TPO-E83-GUG-X-00001, Los Alamos National Laboratory (November 1999)

[Wa02] L.S. Waters, editor, "MCNPX User's Manual, Version 2.3.0," Los Alamos National Laboratory report LA-UR-02-2607 (April 2002)

[Wa04] A. Wambersie. J. Hendry, J. Gueulette, R. Gahbauer, R. Potter, V. Gregorie. Radiobiological rationale and patient selection for high- LET radiation in cancer therapy. Radiot. Oncol. **73,** Suppl 2: S1-S14 (2004).

[Wh92] R.M. White, J.J. Broerse, P.M. DeLuca Jr., G. Dietze, R.C. Haight, K. Kawashima, H.G. Menzel, N. Olsson and A. Wambersie. Status of nuclear data for use in neutron therapy. Rad. Prot. Dosim. **44**, 11-20 (1992).

[Ul81] J.L. Ullman, N. Peak, S.W. Johnsen, S. Raventos, P. Heintz, Improved measurement of neutron spectrum from 35 MeV protons on thick beryllium. Med. Phys. **8**, 396-397 (1981).

[Ya81] Y. Yariv and Z. Fraenkel, Intranuclear cascade calculation of high-energy heavy-ion interactions: Effects of interactions between cascade particles. Phys. Rev. **C42**, 488-494 (1981).

[Zi06] A. Zimbal, H. Klein, M. Reginatto et al, High-resolution spectrometry with liquid scintillation detectors for fusion applications. Proceedings of Science. (FNDA2006)035, available at http://pos.sissa.it.